THESIS FOR THE DEGREE OF DOCTOR OF PHILOSOPHY

Transport properties of Bi_2Se_3 Topological insulator nanoribbon-Superconductor hybrid junctions

ANANTHU P. SURENDRAN

Department of Microtechnology and Nanoscience (MC2)

Quantum Device Physics Laboratory

CHALMERS UNIVERSITY OF TECHNOLOGY

Göteborg, Sweden 2023

Transport properties of Bi_2Se_3 Topological insulator nanoribbon-Superconductor hybrid junctions

ANANTHU P. SURENDRAN
Göteborg, Sweden 2023
ISBN 978-91-7905-944-6

Doktorsavhandlingar vid Chalmers tekniska högskola
Ny serie Nr 5410
ISSN 0346-718X

Quantum Device Physics Laboratory
Department of Microtechnology and Nanoscience (MC2)
Chalmers University of Technology
SE-412 96 Göteborg, Sweden
Telephone: +46 (0)31-772 1000

Cover
A false colored SEM image of two adjacent Al-Bi_2Se_3-Al junctions.

Printed by Chalmers Reproservice
Göteborg, Sweden 2023

Transport properties of Bi_2Se_3 Topological insulator nanoribbon-Superconductor hybrid junctions

ANANTHU P. SURENDRAN
Quantum Device Physics Laboratory
Department of Microtechnology and Nanoscience (MC2)
Chalmers University of Technology

Abstract

In recent years, topological superconductivity and Majorana zero-energy modes have attracted vast interest due to their potential for topologically protected quantum information processing. Hybrid devices involving a conventional s-wave superconductor (S) in proximity to a 3D Topological Insulator (TI) are expected to provide a platform for emulating and studying these phenomena. In superconductor-topological insulator-superconductor (S-TI-S) Josephson junctions, Majorana physics manifests as peculiar current-carrying bound states, i.e., Majorana bound states (MBS) localized on the topological surface of the 3D TI. In this thesis, we investigate the electrical transport properties of superconductor-topological insulator-superconductor (S-TI-S) Josephson junctions fabricated using Bi_2Se_3 nanoribbons and Al electrodes.

We explore in-depth the size quantization effects and ballistic transport in S-TI-S junctions by studying the width dependence of critical current density in our junctions and Fabry-Pérot (FP) resonance arising from ballistic topological surface states (TSSs). We show that FP resonance survives in devices with width scales over a micrometre. Further characterization involves the measurement of the current phase relation (CPR) of our Al-Bi_2Se_3-Al junctions using the asymmetric SQUID measurements technique. The experimentally extracted CPR of our junctions is heavily skewed and supports transport by ballistic TSSs.

The third part of the thesis developed around the microwave probing of Andreev bound state dynamics in Al-Bi_2Se_3-Al junctions. We use a circuit-QED-inspired layout where an RF-SQUID based on our S-TI-S junction is inductively coupled to a coplanar waveguide resonator. By studying the AC susceptibility of our junctions, we reveal bounds states with small energy gaps (or high transparency).

In the final section of the thesis, we address the problem of the unavoidable bulk contributions to transport in our TINR-based devices and discuss some of our attempts to tackle the problem by employing electrostatic gates. We also explore the possibility of using ultrathin TI-nanoribbons, which are easy to control by a gate as compared to thick nanoribbons. The gate response of the conductivity indeed shows hints of size-induced subband quantization.

Overall, the work presented in the thesis demonstrates the presence of highly transparent ballistic transport modes arising from TSSs in Al-Bi_2Se_3-Al junctions using a variety of DC and AC measurements. Our devices give hints that size control of the nanoribbons and geometry of the junctions can be instrumental in isolating the contributions of TSSs to the transport properties in the normal and superconducting state.

Keywords: Topological insulator, Bismuth selenide, superconductivity, Josephson junctions, SQUID, surface states, ac susceptibility, andreev bound states ...

In an attempt to justify the words never said, the moments never spent, the courage never mustered and duties never fulfilled;

To the warm memories of my mom Ajitha and Susanne;

To teachers Bindhu and Nima whose dreams I carry with me;

And to my loving fiancée Marielle.

Acknowledgements

During this PhD study, I went through some of the darkest days of my life. With the sudden passing of my mom, Ajitha, I lost all my courage. Then, shortly after, with the untimely passing of my girlfriend at the time, Suzie, I lost all hope, and with her mom, Ulla-Britt, following her, I lost trust in myself. I have never been this angry or sad or depressed before; I have never hated myself this much or felt like a failure to this extent. The sleepless, nightmare-ridden nights that followed; I would wish that for anyone. I can only imagine how unpleasant it might have been to be around me; it was a very low point in my life. I would start by apologising to everyone who had to go through any inconvenience because of me over the past five years; I am sorry. Thank you for sticking around!

At some point during the last years, I thought I would never complete this PhD or write a thesis. Yet here I am! Thanks to my supervisors, Thilo Bauch and Floriana Lombardi, it would not have been possible without their constant support and patience. When I joined your group, I did not know much about the subject, and Thilo, you sat beside me and taught me most of the things I know now. Even today, when I am at the end of this PhD, you are still teaching me new things, and I am grateful for that and everything you did for me, even the most simple thing of asking, 'Are you okay?'. Floriana, your passion for physics inspires me; you taught me and others 'to think about the physics' and supported me without fail when I needed it. Thank you so much for everything.

I was fortunate enough to work with a fantastic group of people who were always ready to help. Alex, your passion for machine and experimental techniques amazes me and makes me want to learn more about them. Xavier and Kiryl, I am glad I was part of your TI-squad; thanks for the help, discussions, ideas, lunches, hangouts, etc. Domenico, I am grateful you trained me in the cleanroom and thank you so much for checking in on me even years after leaving Chalmers. Edo, when I need help with anything, you were the first to show up; thank you so much for that. I am proud of how quickly you got better at badminton. Most of this thesis is based on your hard work, Gunta, and I am glad we got to work together. Eirc and Riccardo, thank you so much for the things you taught me, all the help, and everything. Núria glad that I got to be a part of your master thesis project, and as you requested, 'Núria, we (all the juniours at QDP) thank you for taking

one for the team!' Alessia, thank you so much for all the chit-chat and for not ratting me out on the pranks. Thank you so much, everyone, for all your help and contributions to my thesis. If I were to do it again, I would choose you guys again as a team.

I want to thank all the current and ex-members of the QDP group, including seniors Dag, Tord, August, Samuel, Andrey, Sergey, Saroj, and Elisabeth and all the juniors, Ivo Petronella C. Cools, Nermin, Lars, Naveen, Anamul, Sumedh, Roselle, Munis, Richa, Aditya, Maha, Bing, Bogdan, Sobhan, Siliva, Chirs, Johanna, Federico, Theresa, Ankit, Aws, Prabhav, Oleg, and whoever I can't remember now for making it an excellent experience work here. I want to also express my gratitude to Lars for helping machine various things over the years. I also want to thank the members of our administrative staff, Annika, Linda, Debbie and Susannah for all the helps over the years.

This project would have been possible with out the Cleanroom here at Chalmers and who people keeps it running. With the knowledge and helps from Bengt, Henrik, Mats, Niclas, Marcus and other it would have been difficult. Thank you all for everthing.

I also want to thank my fellow ESRs from the QuESTech project, namely Naveen, David, Franz, Francesco, Rebecca, Rishabh, Arun, Daniel, Danilo, Bayan, Willy, Johnny, Elias and Laura, for making all the project meetings and other events fun and exciting. I also want to thank Hervé Courtois and Hendrika Borsje-Hekking for heading and managing the project well. I want to thank Jukka Pekola and everyone in the Pico lab for making my visit productive and enjoyable. Thank you so much to Klaus Ensslin and Amaia Zurutuza for all the discussions during the project.

I would also like to thank my fellow members of the Göteborgs Gatufotoförening. It was fun photographing the streets, and it served as meditation to calm myself during some of the rough days. Specifically, I would like to thank Anna Linthander and Linda Svensson for introducing me to the group and others.

I want to express my gratitude to Aisha, Shammy, Naem, Rishi, Sanjay, Vidya, Simin, Azega, and Anjana for being my Indian family here in Sweden and thanks for all the food, trips and hangouts during the past five years.

I greatiful to have had wonderful teacher who helped dream bigger and get better at doing things. Teachers, Bindhu, Nima, Biju, Elsy, Sreenivasan, Sujatha, thank you. Also, I learned lot about experimental condensed matter physics during my master time working in Madhu Thalakulam's lab and some if it I even helped in this project and I am grateful to you and all the other lab members.

I want to thank all my friends, all my family members and all the members of Marielle's family. Specifically, I want to thank my dad for introducing me to science, trying to hold everything together and being there for me at every point in my life. Also, I thank my niece, Aadhya, who is patiently awaiting all the missed birthday gifts.

Mom, Suzie and Ulla, thank you so much for everything. I will miss you all for the rest of my life.

Finally, I would like to thank my fiancée Marielle; thank you so much for being there for me.

List of publications

This thesis is based on work contained in the following papers:

[I] G. Kunakova, **A. P. Surendran**, D. Montemurro, M. Salvato, D. Golubev, J. Andzane, D. Erts, T. Bauch, and F. Lombardi, "Topological insulator nanoribbon Josephson junctions: Evidence for size effects in transport properties", Journal of Applied Physics **128**, 194304 (2020).

[II] **A. P. Surendran**, D. Montemurro, G. Kunakova, X. Palermo, K. Niherysh, E. Trabaldo, D. S. Golubev, J. Andzane, D. Erts, F. Lombardi, and T. Bauch, "Current-phase relation of a short multi-mode Bi_2Se_3 topological insulator nanoribbon Josephson junction with ballistic transport modes", Superconductor Science and Technology **36**, 064003 (2023).

[III] **A. P. Surendran**, G. Kunakova, X. Palermo, K. Niherysh, D. Montemurro, J. Andzane, D. Erts, D. S. Golubev, S. Lara-Avila, F. Lombardi, and T. Bauch, "Ballistic transport on micrometer scale revealed by Fabry-Pérot-like resonances in Bi_2Se_3 nanoribbon devices", Submitted to Phys. Rev. Applied (2023).

[IV] K. Niherysh, X. Palermo, **A. P. Surendran**, A. Kalaboukhkov, R. Sondors, J. Andzane, D. Erts, T. Bauch, and F. Lombardi, "Quantum Confinement and Coherent Transport in Ultrathin Bi_2Se_3 nanoribbons", Submitted to Phys. Rev. Applied (2023).

[V] **A. P. Surendran**, N. A. Herraiz, G. Kunakova, X. Palermo, K. Niherysh, D. Montemurro, J. Andzane, D. Erts, D. S. Golubev, S. Lara-Avila, F. Lombardi, and T. Bauch, "AC Susceptibility of a Bi_2Se_3 nanoribbon Josephson junction", to be submitted (2023).

We always refer to these publications as paper I, II, ..., according to the labeling in the list above.

Papers that are outside the scope of this thesis:

[A] F. Calavalle, P. Dreher, **A. P. Surendran**, W. Wan, M. Timpel, R. Verucchi, C. Rogero, T. Bauch, F. Lombardi, F. Casanova, M. V. Nardi, M. M. Ugeda, L. E. Hueso, and M. Gobbi, "Tailoring Superconductivity in Large-Area Single-Layer NbSe2 via Self-Assembled Molecular Adlayers", Nano Letters **21**, 136–143 (2021).

List of abbreviations

2D	Two dimensional
2DEG	Two dimensional electron gas
3D	Three dimensional
ABS	Andreev bound state
AC	Alternating current
AFM	Atomic Force Microscopy
BCS	Bardeen, Cooper and Schrieffer
BTK	Blonder, Tinkham and Klapwijk
CMP	Condensed matter physics
CPR	Current phase relation
CPW	Coplanar waveguide
DC	Direct current
EBL	Electron beam lithography
FFT	Fast Fourier transform
FP	Fabry-Pérot
h-BN	Hexagonal boron nitride
HEMT	High electron mobility transistor
IBE	Ion beam etching
IQHE	Integer quantum Hall effect
IPA	Isopropanol
IVC	Current-voltage characteristic
MAR	Multiple Andreev reflection
MBS	Majorana bound state
PDMS	Polydimethylsiloxane
PMMA	Polymethyl methacrylate
PVD	Physical vapour deposition
SDE	Superconducting diode effect
SdH	Shubnikov-de Haas
SEM	Scanning electron microscopy
SNS	Superconductor-normal metal-superconductor
SQUID	Superconducting quantum interference device
S-TI-S	Superconductor-topological insulator-superconductor
TI	Topological insulator
TINR	Topological insulator nanoribbon
TR	Time reversal
TSS	Topological surface states
VNA	Vector network analyzer
TI	Topological Insulator

Contents

1 Introduction

In physics, discoveries involve a combination of experiments and theories that explain the observations. The path leading to new physics can be complicated, often going back and forth between a theory and an experiment. If we consider the simplest case leading to a discovery, we either go from theoretical prediction to experimental verification or from experiments to a theory that comprehends the observations. However, not every theory gets to be experimentally tested, and sometimes, it takes years or decades of work for a theory to be experimentally verified or a phenomenon to be theoretically understood. We all know this.

One of the important examples of a theory that resulted in celebrated discoveries came from Paul A. M. Dirac in 1928 [1]. Apart from its crucial role in understanding the quantum nature of spin, his equation that describes relativistic electrons also had another significant implication: it accepts solutions with negative energy. Though initially seemed unrealistic, the negative energy solutions were later interpreted as antiparticles and led to the discovery of positron, the anti-electron by Carl D. Anderson in 1933 [2] and other antimatter particles. In 1937, Ettore Majorana devised an elegant modification to the Dirac equation that predicted a particle that could be its own antiparticle [3]. He speculated that one of the potential candidates that might follow his equation could be neutrinos, which were still hypothetical particles then. With the discovery of neutrinos, it was shown that there is a clear distinction between a neutrino and an anti-neutrino; they can not be Majorna fermions. So, just like the physicist Majorana, who went missing, his particle remained elusive for many years. In 1998, with the observation of flavour oscillation in neutrinos, the idea that neutrinos might be Majorna fermion was back on the table. The particle physics community is experimentally exploring it, and till now, the case of neutrino remains unsettled [4]

Condensed matter physics (CMP) is a field of physics known for its ability to host collective excitation or quasiparticles. Some examples of these include phonons, magnons, excitons, polarons, skyrmions etc. With recent advancements in CMP, mainly in the form of topological band theory, Majorana fermions gathered attention as they could be emulated as a quasiparticle in unconventional material systems, namely Majorana bound states(MBSs). The search for MBSs in solid-state devices is primarily driven by one of their potential technological applications: topologically protected quantum information processing [5–7]. Here, with MBSs, one hopes to have better-performing qubits that are immune to local noise.

The key ingredients required for emulating the elusive Majorana fermion are superconductivity and an unconventional metal, for example, topological surface states(TSSs) of topological insulators(TI) [8–11] or semiconducting nanowires with high spin-orbit coupling [12, 13]. One of the potential systems for emulating MBSs are 3D-topological insulator-superconductor hybrid Josephson junctions (S-TI-S). 3D-TIs are characterized by an insulating bulk and a metallic topological surface states characterized by a Dirac-dispersion with spin-momentum locking. In recent years, they have been studied extensively [14–35]. Though the MBSs in this kind of junctions are not localized (can not be used for topological qubits), they provide a way to explore the unconventional physics of these exotic states. In a multimode S-TI-S junction, Majorana physics might manifest as a peculiar property of a part of the Andreev-bound states carrying the Josephson current. The MBSs give rise to an unconventional 4π periodic current phase relation (CPR) coexisting with a 2π periodic CPR resulting from the conventional Andreev bound states. By probing an S-TI-S junction one could get access to the unconventional physics of MBSs [14–30, 32–35].

A major obstacle in revealing MBSs using Josephson junctions based on readily available 3D-TI, like Bi_2Se_3, Bi_2Te_3, and Sb_2Te_3, is the coexistence of bulk states in addition to the topological surface states, making the electrical transport analysis cumbersome [8, 36]. Compensation doping has been used to reduce the bulk contribution, however, at the expense of electron mobility [15, 25–27, 29, 30, 32–34]. Instead, in this thesis we make use of Al-Bi_2Se_3-Al junctions implemented using Bi_2Se_3 nanoribbon to increase the surface to volume ratio of TI and thereby reducing bulk contributions to transport. Previous studies have shown high-quality interfaces between 3D-TI Bi_2Se_3 nanoribbons and Al electrodes. This thesis further explores the transport of our Al-Bi_2Se_3-Al junctions.

- In the first part of the thesis (Chapter 4), we will look at size quantization effects in S-TI-S junctions. For this, we will discuss two different kinds of measurements done on single junction devices. In the first set of measurements, we look at the dependence of the current density of our S-TI-S junctions on the width of the junctions. Here, we will show that to explain the peculiar response we observed in these devices, one must consider supercurrent transport by TSSs. In the second set of experiments, we look at Fabry-Pérot(FP) conductance oscillation in S-TI-S junctions originating from ballistic TSSs. Here, we will show that the obtained gate periodicity of the resonance matches well in both normal and superconducting states.

- The second part of the thesis (Chapter 5) deals with the extraction of the CPR of our Al-Bi_2Se_3-Al junctions. Here, we use the asymmetric SQUID measurements technique to extract the CPR. We will show that the obtained CPR is skewed, and the observed skewness values require transport by ballistic TSSs with high transparencies. Moreover, we show that one needs to

consider both ballistic and diffusive contributions to the transport to fit the extracted CPR of our S-TI-S junctions.

- The third part of the thesis (Chapter 6) is dedicated to microwave probing of ABSs in Al-Bi_2Se_3-Al junctions. For this, we will use an S-TI-S junction-based RF-SQUID, which is inductively coupled to a coplanar waveguide resonator. Here, by studying the AC susceptibility of our junctions, we reveal bounds states with small energy gaps or high transparency. We show that the relaxation rate of the bounds states in our junctions exceeds 1GHz, which is an indication of the existence of a quasiparticle continuum in the gap.

- In the final section (Chapter 7), we address the problem of the unavoidable bulk contributions to transport in our TINR-based devices and discuss some of our attempts at tackling the problem. Here, we show two different gating approaches. An h-BN encapsulated device with a top and bottom h-BN layer was more successful in reducing the carriers. Then, we discuss the gate-dependent transport in ultrathin TI-nanoribbons, showing hints of size-induced subband quantization.

Overall, the work presented in the thesis demonstrates the presence of highly transparent ballistic transport modes arising from TSSs in Al-Bi_2Se_3-Al junctions using multiple (DC and AC) measurements. The analysis of the results requires the inclusion of both TSSs and bulk state contributions to conductive bulk channels, and this calls for the development of better TI materials with fully insulating bulk with high mobilities.

2 Background

This chapter provides some of the fundamental concepts of superconductivity, Josephson junctions, SNS junctions, Topological insulators and hybrid devices involving topological insulators and superconductors. In the later section of the chapter, we will also provide a summary of the previous works done at Chalmers that are relevant to understanding this thesis.

2.1 Superconductivity

Over a century ago, after his historic achievement of liquifying helium gas, Dutch physicist Heike Kamerlingh Onnes experimentally demonstrated an odd phenomenon, which he initially referred to as "supraconductivity" [37, 38]. He noticed that the electrical resistance of solid mercury wire suddenly vanished when cooled below a temperature of 4.2K, marking the birth of the field of superconductivity [37–39]. This characteristic temperature below which a material turns superconducting, allowing for non-dissipative current flow, is called the critical temperature T_c. In 1933, Walther Meissner and Robert Oschenfeld showed that below T_c superconductors expel magnetic fields from the bulk of the material and behave as perfect diamagnets [40, 41]. Thus, the phenomenon of superconductivity manifests as perfect conductivity or zero DC resistance and perfect diamagnetism or the Meissner effect. With the ability to pass high currents without dissipation, superconductors enabled the creation of powerful magnets, which find their applications in many areas, from research to healthcare. Because of this, superconductors are commonly thought of as just conductors with zero resistance. However, it is essential to note that the true hallmark of this macroscopic quantum phenomenon is the Meissner effect, which separates superconductors from a "trivial" perfect conductor [40–42].

In 1957, J. Bardeen, L. Cooper and J. R. Schrieffer developed the microscopic theory of low-temperature superconductivity called the BCS theory [43]. BCS theory is based on an effective weak electron-electron attractive interaction mediated by phonons (lattice vibrations) resulting in the formation of electron pairs called the Cooper pairs. The dissipationless electrical transport in a superconductor is carried out by these Cooper pairs. BCS theory showed that, below T_c, Cooper pairs are more energetically favourable and electrons in the vicinity of Fermi level with opposite spin and momentum get paired to bosons, which condense into the same ground state. As a result, an energy gap Δ opens up

in the density of states of the superconductor, separating the ground state from quasiparticle states. The density of states of quasiparticle excitations in a BCS superconductor can be written as [42]

$$N_s(E) = N(E_F)\frac{|E|}{\sqrt{E^2 - \Delta^2}}\Theta(|E| - \Delta) \tag{2.1}$$

where E is energy with respect to Fermi energy E_F, $N(E_F)$ is the density of states at E_F in the normal state and Θ is the Heaviside step function. The sketch of the density of states is given in figure 2.1. At T = 0, the BCS superconducting gap takes the form $\Delta \simeq 2\hbar\omega_D e^{-1/N(E_F)V} \simeq 1.764 k_B T_c$, where ω_D is the Debye frequency, and V is the effective electron-phonon coupling constant [43]. For the Al contacts used in our experiments with a typical $T_c = 1.15$K, we get $\Delta_0 \simeq 175$ μeV. Further details on the basics of BCS superconductivity can be found in various standard textbooks [42].

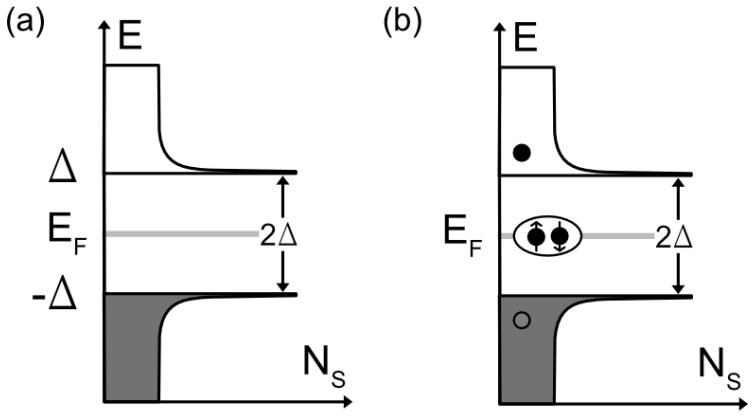

Figure 2.1: (a) Sketch of quasiparticle density of states of superconductor as a function of energy with various energy locations marked. (b) The sketch density of states of superconductor depicting a Cooper pair and quasiparticle excitations both as an electron (black dot) and a hole (open dot) as well.

2.2 Jospehson Junctions

Following various experiments looking at tunnelling effects in structures involving superconductors, in 1962, Brian D. Josephson developed theoretical predictions for tunnelling current in a system (SIS tunnel junction) where two superconducting electrodes are separated by a thin insulating tunnel barrier [44–47]. He showed that apart from quasiparticle tunnelling, it is possible to observe the transfer of Cooper pairs through the barrier. The so-called Josephson junctions were experimentally realized shortly after [48]. Now, after more than 60 years since the

initial prediction from Josephson, Josephson junctions come in various forms other than SIS junctions, junctions with normal metallic barriers like SNS and SINIS, and point contact and constriction-based junctions, etc. They are utilized in many applications, including Josephson voltage standard, superconducting qubits, SQUID magnetometers, parametric amplifiers, bolometers, etc [49].

2.2.1 Josephson Effect

To understand the behaviour of Cooper pair tunnelling, consider two superconducting electrodes with wave functions $\Psi_1 = \sqrt{n_1}e^{i\varphi_1}$ and $\Psi_2 = \sqrt{n_2}e^{i\varphi_2}$, with n_1 and n_2 being the Cooper pair density and φ_1 and φ_2 being the phase of the order parameter at the respective electrodes [47, 49]. Now, if the barrier is small enough, then the wavefunctions of the two electrodes can overlap, allowing for Cooper pairs to tunnel. The Josephson effect can be summarized into two equations given below,

$$I = I_c \sin\varphi \tag{2.2a}$$

$$V = \frac{\hbar}{2e}\frac{\partial\varphi}{\partial t} \tag{2.2b}$$

Here, φ corresponds to the phase difference between the electrodes, and I_c corresponds to the critical current of the junction. Equation 2.2a is called the DC Josephson effect, and it shows that the junction can support supercurrent without developing any voltage until the critical current is reached. Since this expression relates the current and phase in a junction, it is also called the current-phase relation (CPR) of the junction, and it plays a crucial role in understanding the properties of a Josephson junction. Now, the second Josephson equation given in 2.2b describes the time evolution of the phase difference φ across the junction with respect to the voltage drop across the junction. By integrating, it is easy to see that the time evolution of phase across the junction can be expressed as

$$\varphi(t) = \frac{2eV}{\hbar}t + \varphi_0 \equiv \omega_J t + \varphi_0 \qquad \text{with} \quad f_J = \frac{\omega_J}{2\pi} = \frac{2eV}{h} \tag{2.3}$$

being the Josephson frequency. So, when finite voltage develops across the junction, the phase across the junction evolves in time, generating an alternating supercurrent. This is called the AC Josephson effect, and the junction radiates photons at a frequency defined by the voltage bias and fundamental constants. For instance, when $V = 1\mu V$, the Josephson radiation is emitted at a frequency of $f_J \simeq 483.6$ MHz [46, 47].

2.2.2 Shapiro Steps

When a voltage with AC components is applied to a Josephson junction, it results in the observation of Shapiro steps in the current-voltage characteristic (IVC) of

the junction [49, 50]. To understand this, let us consider a voltage bias across the junction of the form

$$V(t) = V_{dc} + V_{rf} \cos \omega_{rf} t \tag{2.4}$$

where V_{dc} is the DC voltage and V_{rf} and ω_{rf} corresponds to the amplitude and angular frequency of the applied RF signal. Now, plugging this into the AC Josephson equation 2.2b, we get the phase across the junction as

$$\varphi(t) = \frac{2e}{\hbar}\left(V_{dc}t + \frac{V_r f}{\omega_{rf}} \sin \omega_{rf} t\right) + \varphi_0. \tag{2.5}$$

The current across the junction can be written as,

$$\begin{aligned} I(t) &= I_c \sin\left[\frac{2e}{\hbar}\left(V_{dc}t + \frac{V_r f}{\omega_{rf}} \sin \omega_{rf} t\right) + \varphi_0\right] \\ &= I_c \sum_{n=-\infty}^{\infty} (-1)^n \mathcal{J}_n\left(\frac{2eV_{rf}}{\hbar\omega_{rf}}\right) \sin\left[\left(\frac{2e}{\hbar}V_{dc} - n\omega_{rf}\right)t + \varphi_0\right]. \end{aligned} \tag{2.6}$$

Here, $\mathcal{J}_n$ is the nth order of the Bessel function of the first kind. As seen in the equation 2.6, whenever $\frac{2eV_{dc}}{\hbar} = n\omega_{rf}$, the supercurrent is time independent and DC current steps emerge at voltages $V_n = \frac{nh}{2e} f_{rf}$. These are called Shapiro steps, and this is one of the most fundamental properties of a Josephson junction often used for characterizing them [49]. Since voltage spacing depends on drive frequency f_{rf} and fundamental constant, this phenomenon is used in metrology for defining voltage standards.

2.2.3 Josephson inductance and Josephson energy

From an electrical circuit point of view, a pure Josephson element is a nonlinear inductor [49]. To see this, let us take the time derivative of Josephson current,

$$\frac{\partial I}{\partial t} = I_c \cos\varphi \frac{\partial \varphi}{\partial t} = I_c \cos\varphi \frac{2e}{\hbar} V \qquad \text{or} \quad V = \frac{\hbar}{2eI_c \cos\varphi} \frac{\partial I}{\partial t}. \tag{2.7}$$

Now, by comparing this to the equation for the voltage across an inductor, $V = L\frac{dI}{dt}$, we get the Josephson inductance to be

$$L_J = \frac{\hbar}{2eI_c} \frac{1}{\cos\varphi} = \frac{\Phi_0}{2\pi I_c} \frac{1}{\cos\varphi}, \tag{2.8}$$

where $\Phi_0 = h/2e$ is the magnetic flux quantum. Because of the presence of the $1/\cos\varphi$ term, the L_J is nonlinear and the value L_J diverges whenever φ is an odd multiple of $\pi/2$. The energy stored in a Josephson junction is given by

$$E_J(\varphi) = \int_0^t IV dt = \frac{\hbar I_c}{2e} \int_0^{\varphi} \sin\varphi d\varphi = E_{J0}(1 - \cos\varphi), \tag{2.9}$$

with $E_{J0} = \frac{\hbar I_c}{2e}$ being the maximum Josephson energy.

2.2.4 Josephson effect in magnetic field

Consider a Josephson junction with an applied perpendicular magnetic field (B) as shown in figure 2.2(a). Here, we consider that case, in which the thickness of the superconducting electrode $t \gg w, \lambda_{1,2}$, with w being the width of the junction and $\lambda_{1,2}$ corresponds to the London penetration depth. The spatial modulation phase φ across the junction field along the y-axis follows the equation [49],

$$\frac{\partial \varphi}{\partial y} = \frac{2\pi B d_{eff}}{\Phi_0} \qquad \text{with} \qquad d_{eff} = \lambda_1 + \lambda_2 + d. \tag{2.10}$$

Now, the critical current of the junction shows modulation patterns given by

$$I_c(\Phi) = I_{c,max} \left| \frac{\sin \pi\Phi/\Phi_0}{\pi\Phi/\Phi_0} \right| \tag{2.11}$$

Here, Φ is the total flux through the junction, which can be written in terms of the applied magnetic field as $\Phi = BA_{eff}$. In case this $A_{eff} = wd_{eff}$, and to get this value, we have to consider a closed contour(dashed line) inside the junction such that either the current density $\mathbf{j} = 0$ or $\mathbf{j}$ is perpendicular to the contour used for getting flux values as shown in 2.2(a)(here we make use of the equation $\frac{\hbar}{e^*}\nabla\varphi = \frac{m^*}{ne^{*2}}\mathbf{J}_s + \mathbf{A}$ from Gizburg Landau theory [42]). The total effective area of the junction is marked in shades of blue. Now, as seen in equation 2.11, the critical current of the junction modulates with external flux Φ, and whenever Φ/Φ_0 is a nonzero integer, the critical current of the junction goes to zero. This is known as the Fraunhofer pattern of the junction due to its resemblance to a single-slit diffraction pattern. Since it has to do with the spatial variation phase across a junction in a magnetic field, it provides a powerful tool for studying the quality of the junction.

Now, in the case of a planar thin film-based Josephson junction where $t \ll \lambda, w$, the effective area of the junction needs to be redefined to account for the flux-focusing effect. In this case, the contour, which satisfies the requirement of $\mathbf{j} = 0$ or is perpendicular to $\mathbf{j}$ is shown in figure 2.2(b) along with the lines representing screening current sketched on the left electrode [51]. The effective area in this case is $A_{eff} \approx w^2/2 + wd$, which is twice the area of the triangular region plus the area of the insulating section. Rosenthal et al. showed that the effective area for a planar thin film junction is given by $A_{eff} = w^2/1.84 + wd$ [51]. This roughly corresponds to the area marked in shades of blue figure 2.2(b).

2.2.5 SQUIDs

Superconducting QUanutum Interfence Devices(SQUIDs) work by combining the Josephson effect and fluxiod quantization effect [52]. They can be used as a very sensitive magnetic flux to voltage converter. In the following, we will discuss briefly the working principles of both DC and RF SQUIDs.

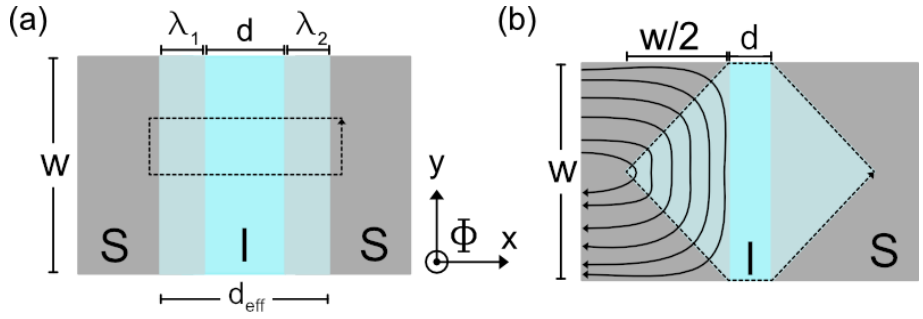

Figure 2.2: (a) Schematic of a Josephson junction of width w and superconducting electrode separation of d in an external magnetic flux Φ (corresponding to a magnetic feild B).The effective area of the junction is shown in shades of blue. (b) A planar thinfilm junction in an external magnetic field. The black lines correspond to the screening current in the electrodes, and the effective area of the junction is given by the region marked in shades of blue.

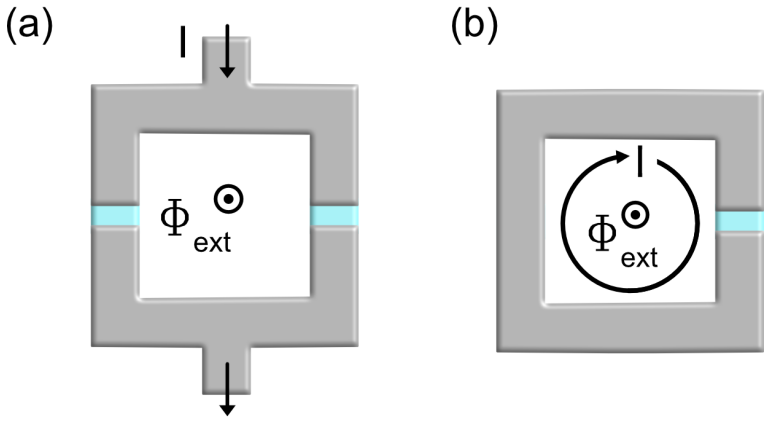

Figure 2.3: Schematic of a (a) DC-SQUID formed out of two Josephson junctions connected by a superconducting loop and (b) an RF SQUID consisting of a single Josephson junction subject to an externally allpied magnetic flux Φ_{ext}

DC SQUID

The DC SQUID consists of a superconducting loop of inductance L interrupted by two Josephson junctions, with applied external flux (Φ_{ext})through the loop as shown in figure 2.3(a). The total current through SQUID I can be written in terms of current through the Josephson junction in the two loop arms as [52]

$$I = I_{c1} \sin \varphi_1 + I_{c2} \sin \varphi_2 \tag{2.12}$$

Since our loop is superconducting, from fluxoid quantization, we can write

$$\varphi_1 - \varphi_2 - \frac{2\pi\Phi}{\Phi_0} = 2\pi n \tag{2.13}$$

where the total flux enclosed by the loop is given as $\Phi = \Phi_{ext} - LI_s$ with I_s being the screen current through the loop. Now, if we assume the two junctions are identical with $I_{c1} = I_{c2}$ and the loop inductance L to be very small and rewrite φ_1 as φ for simplicity, then by inserting equation 2.13 in equation 2.12 we get,

$$I = 2I_{c1} \left| \cos \frac{\pi \Phi_{ext}}{\Phi_0} \right| \sin \varphi = I_c(\Phi_{ext}) \sin \varphi \tag{2.14}$$

with I_c being the critical current of the SQUID. From here, we can see that a SQUID acts like a Josephson whose critical current modulates as a function of flux through the loop. For the finite loop inductance case, there is no analytic expression for the SQUID current, and in this case, we will have to use numerical methods to calculate the critical current of the SQUID [53]. To quantify the impact of L, we can define the screen parameter of β_L of the DC SQUID as $\beta_L = LI_c/\Phi_0$, where for $\beta_L \ll 1$ we can neglect the effect of the inductance such that $\Phi \approx \Phi_{ext}$.

RF SQUID

Unlike DC SQUID, in RF SQUID, only a single Josephson junction is incorporated into the superconducting loop, as shown in figure 2.3(b). As the name suggests, the RF SQUID can only be probed using microwaves, and this is usually done by coupling it inductively to a tank circuit [52]. The details of an RF SQUID coupled to a resonator are discussed in Appendix A. Now, like in the case of DC SQUID, we can apply fluxoid quantization to arrive at

$$\varphi - \frac{2\pi\Phi}{\Phi_0} = 2\pi n \qquad \text{or} \qquad \varphi = \frac{2\pi}{\Phi_0} \left(\Phi_{ext} - LI \right) \tag{2.15}$$

which is a self-consistent equation since I is a function of φ, and needs to be solved numerically, just like for the finite inductance case of DC SQUID. Here, we can also define a screening parameter as $\beta_L^{RF} = 2\pi I_c L/\Phi_0$. Now, assuming a sinusoidal CPR, we can rewrite equation 2.15 as

$$\frac{\Phi_{ext}}{\Phi_0} = \frac{1}{2\pi} \left(\varphi - \beta_L^{RF} \sin \varphi \right). \tag{2.16}$$

The external flux is plotted in terms of the phase across the junction in figure2.4. As seen here, if the $\beta_L^{RF} \ll 1$, the flux due to the screening current becomes negligible, and the flux to phase conversion, in this case, is rather linear. For finite $\beta_L^{RF} < 1$, the flux to conversion is nonlinear, with a sinusoidal curve imposed on top due to the sinusoidal CPR. In this case, if we invert the curve, the flux to phase conversion is single-valued. Where for $\beta_L^{RF} \geq 1$, the flux to phase conversion curves is multivalued in some regions, and the curve will be hysteretic around φ values, which are an odd multiple of π. In this case, phase biasing the SQUID around the odd multiple of the value of π is not possible. So, in all our experiments, we want to work at $\beta_L^{RF} \ll 1$.

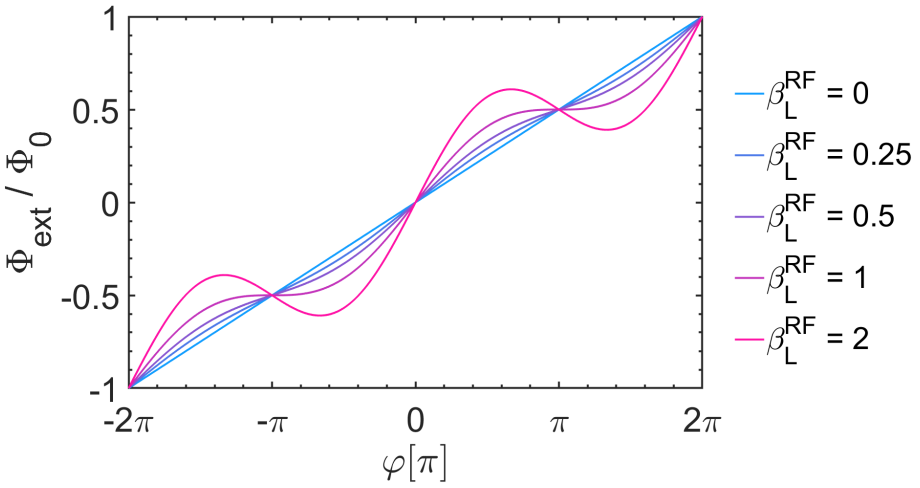

Figure 2.4: Plot showing external magnetic flux in terms of phase φ across the junction for an RF-SQUID for various values of β_L^{RF}. As seen here, $\beta_L^{RF} \ll 1$, is have linear phase-flux conversion, but for $\beta_L^{RF} < 1$, it becomes nonlinear due to the sinusoidal contribution from the CPR. If we invert this curve for $\beta_L^{RF} \geq 1$, then the phase across the junction will be hysteretic and will skip over the regions around which φ which an odd multiple of π.

2.3 Introduction to SNS Junctions

In this subsection, we will take a look at the transport in SNS junctions, as this thesis deals with junctions of the form S-TI-S.

2.3.1 Andreev reflection, ABS and MAR

Let us start by looking at the scattering properties of an NS interface. When an electron with energy E less than the superconducting gap is incident on an NS interface, as shown in figure 2.5(a), we would expect it to reflect back as there are no available quasiparticle states inside the superconducting gap. In such cases, no current can be transferred from N to S. However, in 1964, A. F. Andreev theoretically showed that at an NS interface, a different process can occur, which will allow for charge transfer between the N and S sides [54]. The microscopic scattering mechanism which converts quasiparticle current to Cooper pair current is called Andreev reflection and is schematically shown in figure 2.5(b).

Here, an incident electron with $E < \Delta$ forms a Cooper pair with an electron at energy $-E$ of opposite spin and momentum and is transferred into the superconductor. Since it is an elastic scattering process, to preserve spin, charge and momentum, a hole is retro-reflected in the metal side with energy $-E$ and opposite spin. The Andreev reflection process is also reversible, which means that if instead of an electron, a hole is incident on the NS interface, a Cooper pair will

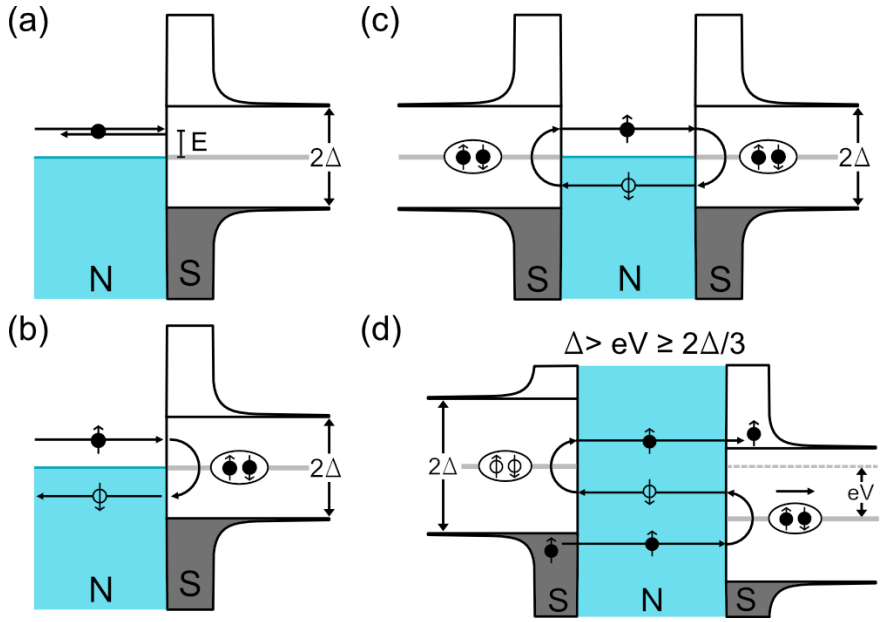

Figure 2.5: Schematic of NS interface with an incident electron on $E < \Delta$ showing (a) normal reflection due to the unavailability of superconducting quasiparticle states inside the superconducting gap and (b) showing the Andreev reflection process in which the electron is converted into a Cooper pair along with a retro-reflected hole at energy $-E$ and thus allowing charge transport across the interface. Schematic representation of (c) Andreev bound states and (d) MAR process in an SNS junction. In panel (d), V corresponds to the voltage drop across the junction.

be annihilated, and an electron is backscattered into the normal side. The effect of Andreev reflection on charge transport was studied by Blonder, Tinkham and Klapwijk (BTK) in 1982, and they showed that the transparency or transmission probability of the interface determines the probability of Andreev reflection [55].

Now, let us consider an SNS junction in which two superconducting electrodes are interrupted by a normal region. In an SNS junction, the Andreev reflection process can occur in the two NS interfaces in a consecutive manner, as shown in figure 2.5(c). Here, a Cooper pair from the left superconducting electrode is Andreev reflected into the normal region as a counter-propagating electron-hole pair, and at the right superconducting electrode, they are Andreev reflected to form a Cooper pair. This results in the accumulation of phase and the total phase, which can be expressed in terms of the phase acquired at the various sections of the junction as $\varphi_{tot} = \varphi_L + \varphi_N + \varphi_L$, where φ_L, φ_R, φ_N are the phase acquired at left interface, right interface and normal section of the junction respectively. When ϕ_{tot} acquired by a charge transfer process across the junction is in an integer multiple of 2π, discrete subgap states called Andreev bound states (ABSs) are formed. ABSs facilitate the Josephson coupling across an SNS junction and are fundamental to understanding the nature of transport across these junctions.

For instance, in an SNS junction, when the linear part of IVC (for $V > 2\Delta$) is extrapolated to zero voltage, it does not go to zero (ohmic response, $V = IR_N$) like in the case of a superconducting tunnel junction. This is due to the presence of multiple Andreev reflections (MAR) in these junctions (see figure 2.5(d)), and residual current at zero voltage is called excess current (I_{ex}), and the value of I_{ex} depends on the strength of the interface barrier [56, 57]. Moreover, the MAR features can be observed in the differential conductance of an SNS junction as peaks or dips at voltage values, $V = 2\Delta/n$, where $n = 1, 2, 3...$ and reflect the number of Andreev reflections (n-1) [58].

2.3.2 Classification of SNS junctions

Based on various length and/or energy scales, SNS junctions of length l can be classified into either short or long and ballistic or diffusive transport regimes. The main two length scales used for classifying SNS junctions are electron mean free path l_e and superconducting coherence length in the normal region ξ_N. Here, l_e is the average length electrons travel in between collisions and is given by, $l_e = v_F\tau_e$, with v_F being the Fermi velocity and τ_e being the elastic scattering time. ξ_N represents the characteristic length scale over which there is electron-hole coherence inside the N region. For ballistic transport in the N region, $\xi_N = \hbar v_F/\Delta$ and for diffusive case $\xi_N = \sqrt{\hbar D/\Delta}$, where D is the diffusion constant. Another important parameter that can used for classifying SNS junctions is the Thouless energy $E_{Th} = \hbar/\tau_N$, where τ_N is the charge crossing time across the N region. For the ballistic case $E_{Th} = \hbar v_F/l$ and for diffusive case, $E_{Th} = \hbar D/l^2$. If $E_{Th} \gg \Delta$, then the junction is in the short limit and if $E_{Th} \ll \Delta$ then we have a long junction. In table 2.1, we have summarized all the transport regimes based on the parameters discussed above.

Transport regime	Short	Long	ξ_N	E_{Th}
Ballistic	$l < l_e, \xi_N$	$\xi_N < l < l_e$	$\hbar v_F/\Delta$	$\hbar v_F/l$
Diffusive	$l_e < l < \xi_N$	$l_e, \xi_N < l$	$\sqrt{\hbar D/\Delta}$	$\hbar D/l^2$

Table 2.1: Transport regime of an SNS junction

2.3.3 Short ballistic junctions

In this thesis, we are mostly interested in working in the short junction limit. This is because, in this case, the energy dispersion relation of ABSs takes rather a simple form as the phase φ_N acquired inside the normal channel can be ignored. For short ballistic junctions, the dispersion relation connecting the energy E_n of

the nth ABS pair, with a transmission probability τ_n, to phase difference $\varphi = \varphi_2 - \varphi_1$ across the junction is given by [59, 60]

$$E_n^{\pm}(\varphi) = \pm\Delta\sqrt{1 - \tau_n \sin^2(\varphi/2)}. \tag{2.17}$$

The dispersion relations of ABSs for various τ_n values are plotted in figure 2.6(a). As seen here, the gap between the Andreev levels is smaller at $\varphi = \pi$, and is given by $E_{gap}(\pi) = 2\Delta\sqrt{1-\tau_n}$. When the transmission probability of the channel is unity, the energy gap closes. The energy levels E_n^- and E_n^+ can be thought of as ground $|g\rangle$, and excited state $|e\rangle$ energies of ABSs that lie inside the superconducting gap, and they transport current in forward and backward directions, respectively [61, 62]. The different states of Andreev levels are plotted in 2.6(b) following the semiconducting picture. One can drive transition between $|g\rangle$ and $|e\rangle$ with microwave radiation. However, it is rather difficult as one requires ABSs with very high transmission probabilities to be accessible by the typical operating range of microwave circuits ($\omega/2\pi \simeq$5-10 GHz). For instance, we work mostly in the 4-8 GHz frequency range and if we assume a typical Δ_{Al} of 180 μeV for Al electrodes, we need ABSs with τ values close to 0.991, which is very high and hard to obtain. Apart from the $|g\rangle$ and $|e\rangle$ states, it is also possible to have another kind of state in an SNS junction, namely odd states $|o\rangle$. Here, either both E_n^- and E_n^+ levels of the bound state pair are empty or filled. The odd state results in no net current transport [61–63]. This is because, in one case, there is no Cooper pair transfer across the junction and in the other, equal and opposite amounts of Cooper pairs are exchanged between the electrodes.

We can instead make use of the CPR of the Andreev-bound states, which connects supercurrent to the phase across the junction, to obtain information about them. One can go from the ABS dispersion to the CPR using the relation [59, 60],

$$I(\varphi) = \frac{2e}{\hbar}\frac{\partial E}{\partial \varphi} \tag{2.18}$$

and at zero temperature, the CPR of the short ballistic junction with n mode of transmission probabilities τ_n can be written as [60],

$$I(\varphi) = \frac{e\Delta(T)}{2\hbar}\sum_{n=1}^{N}\frac{\tau_n \sin(\varphi)}{\sqrt{1 - \tau_n \sin^2(\varphi/2)}} \tag{2.19}$$

At finite temperature T, the population of the Andreev levels will change according to Fermi-Dirac distribution, and the equilibrium CPR of the junction can be written as

$$I(\varphi, T) = \frac{2e}{\hbar}\sum_{n=1}^{N}\left[\frac{\partial E_n^+}{\partial \varphi} f_n^+ + \frac{\partial E_n^-}{\partial \varphi} f_n^-\right] \qquad \text{or,} \tag{2.20a}$$

$$I(\varphi,T)=\frac{e\Delta(T)}{2\hbar}\sum_{n=1}^{N}\frac{\tau_n\sin(\varphi)}{\sqrt{1-\tau_n\sin^2(\varphi/2)}}\tanh\left(\frac{\Delta(T)}{2k_BT}\sqrt{1-\tau_n\sin^2(\varphi/2)}\right). \tag{2.20b}$$

Here, $f_n^{\pm}=1/(1+e^{E_n^{\pm}/k_BT})$ is the Fermi-Dirac distribution, k_B is the Boltzmann constant and $\Delta(T)$ is temperature dependent superconducting gap.

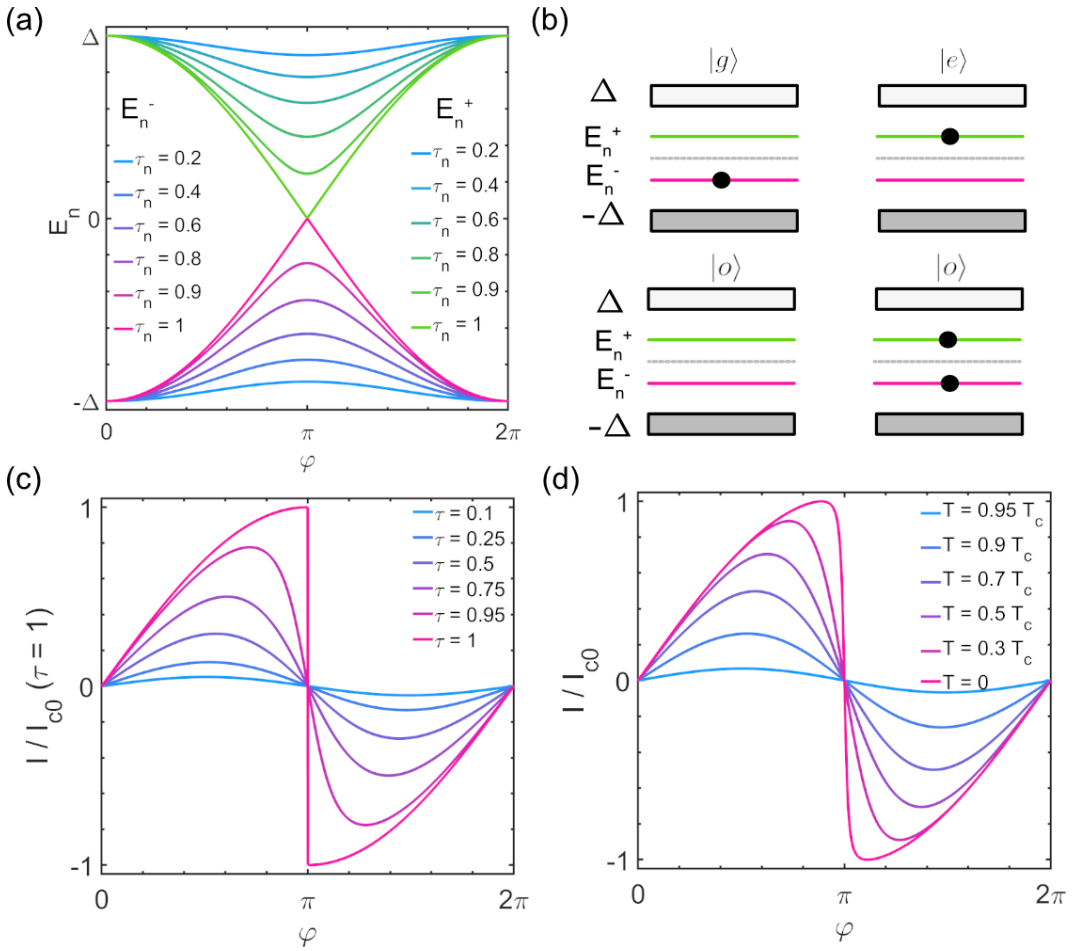

Figure 2.6: (a) The energy dispersion relations of ABSs plotted as a function of phase φ for various transmission probabilities (τ_n). (b) The semiconductor picture of band structures corresponding to a pair of ABSs in $|g\rangle$, $|e\rangle$ and $|o\rangle$ states. Here, only the $|g\rangle$ and $|e\rangle$ results in net current transport. (c) Calculated CPRs (at $T=0$) of a short ballistic SNS junction for various τ_n values. The CPRs are highly forward skewed in case of high τ_n values, and for low τ_n values, they evolve into a sinusoidal CPR. (d) Normalized CPRs of a short ballistic SNS junction with $\tau_n = 0.9999$ for various temperatures showing the evolution of CPR into sinusoidal CPR at high temperatures.

In figure 2.6(c), we have plotted the CPR of a single channel short SNS junction with varying τ values. Here, we can see that for a small τ value, the CPR resemble a sinusoidal curve, whereas as τ values go up, they get more and more slanted or

skewed. So, a more skewed CPR should indicate a higher transmission probability of the normal channel. The temperature dependence of the CPR of a junction with $\tau = 0.9999$ is plotted in figure 2.6(d), and here we have a skewed CPR at lower temperatures, and as temperature goes up, the CPR starts evolving into a sinusoidal curve. These behaviours can be seen mathematically by taking $\tau_n \to 0$ limit of equation 2.20b to first arrive at the Ambegaokar-Baratoff formula for superconducting tunnel junction [64] and then at the DC Josephson equation[46] by taking $T \to 0$ limit as,

$$I(\varphi) = \frac{\pi\Delta(T)}{2eR_N} \tanh\left(\frac{\Delta(T)}{2k_BT}\right) \sin\varphi \overset{T\to 0}{=} \frac{\pi\Delta(T)}{2eR_N} \sin\varphi \tag{2.21}$$

where, R_N and $\Delta(T)$ are normal state resistance and temperature-dependent superconducting gap, respectively. Here the normal state conductance is given by the Landauer formula $G_N = R_N^{-1} = 2e^2/h \sum_n \tau_n$.

2.3.4 Short diffusive junctions

In the case of the short diffusive junction, instead of a discrete spectrum of ABSs, we have a dense spectrum. From random matrix theory, we get the distribution of various transmission probabilities in a diffusive wire as [65],

$$\rho(\tau) = \frac{\pi\hbar G_N}{2e^2} \frac{1}{\tau\sqrt{1-\tau}} \tag{2.22}$$

This is known as the Dorokhov distribution, and it is plotted in figure 2.7(a). As seen here for diffusive wire, most of the modes are distributed around the extreme end of transmission probabilities, and there are modes in the whole range of [0,1]. So, to calculate the CPR of a short diffusive junction, we can replace the sum in equation 2.20a with an integral in the interval $\tau = [0, 1]$ covering the full range of transmission probabilities as [62]

$$I(\varphi, T) = \frac{e\Delta(T)}{2\hbar} \sin(\varphi) \int_0^1 \frac{\tau\rho(\tau)}{\sqrt{1-\tau\sin^2(\varphi/2)}} \tanh\left(\frac{\Delta(T)\sqrt{1-\tau\sin^2(\varphi/2)}}{2k_BT}\right) d\tau. \tag{2.23}$$

The CPRs of a short diffusive junction at various temperatures are plotted in figure 2.7(b) along with the zero temperature case of the ballistic junction with $\tau = 1$ for comparison. Unlike the short ballistic case (magenta line) with highly skewed CPR with maximum occurring at phase $\varphi_{max} = \pi$, the zero temperature CPR of the short diffusive junction (green line) is not as skewed, and the maximum of the CPR occurs at $\varphi_{max} \simeq 0.627\pi$. This is due to the presence of modes with a bimodal distribution of transmission probabilities in a diffusive wire. Like in the case of short ballistic junctions, we see the CPR evolving into a sinusoidal CPR at higher temperatures.

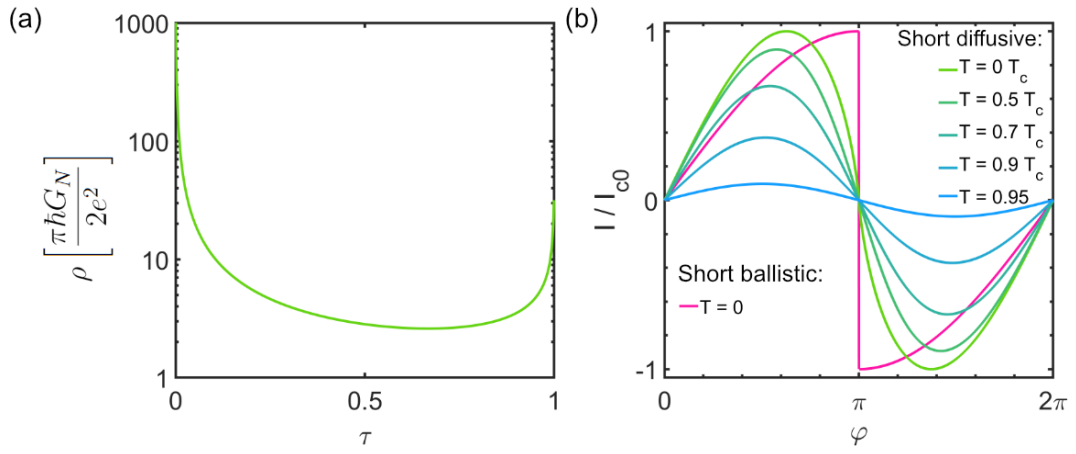

Figure 2.7: (a) Dorokhov distribution of transmission probabilities used for modelling diffusive wire. (b) Temperature evolution of CPRs of a short diffusive SNS junction. Here, the magenta line corresponds to the zero temperature limit of CPR of a short ballistic junction with $\tau_n = 1$. As seen here, the value at phase φ_{max} at which CPR maximum occurs is smaller for short diffusive junction compared to the ballistic case.

2.4 Topology in condensed matter system

In this section of the thesis, we will briefly go through topology and how it is related to the band structure of materials in condensed matter physics(CMP). We will introduce the Berry phase and how it is connected to the topological properties of materials. Then, we will provide a brief description of topological insulators and Bi_2Se_3, the material of choice for this thesis.

2.4.1 Topology and topological invariant

Let us start by looking at topology. Topology is a branch of mathematics which deals with conserved properties of a geometric object under continuous deformation like stretching, contracting, bending, twisting, etc, without cutting or glueing. The property of the object that does not change under continuous transformation is known as a topological invariant. For instance, consider a sphere, and it can be smoothly transformed into a disk, and topologically, these two shapes are equivalent. Whereas spheres and doughnuts are not. They are distinguished by counting the number of holes, and there are no smooth deformations which will take us from one to the other. The topological invariant, in this case, is an integer known as the genus g of shape and using the Gauss-Bonnet theorem, we get [66, 67]

$$2 - 2g = \frac{1}{2\pi} \int_s K dA \tag{2.24}$$

where K is the Gaussian curvature K of the shape. Now, for a sphere, $g = 0$ and for a torus, $g = 1$, making them topologically distinct. This idea can be applied to the band structure of materials. There are trivial insulators like vacuum with normal band gaps, and there are insulators with non-trivial topology with inverted band gaps. The existence of such topological distinct band structures can be understood in terms of a geometric phase called the Berry phase [68, 69], and we will discuss it first.

2.4.2 Berry Phase

One of the key ingredients for the topological description of material is the Berry Phase [69]. It refers to a geometrical phase factor acquired by the state of a system when subject to an adiabatic change following a closed path in the parameter space of the Hamiltonian describing the system [68]. For a material system in CMP with Bloch state $|u(\mathbf{k})\rangle$ going in close contour C in k space, the Berry phase γ_C can be defined as:

$$\gamma_C = \oint_C \mathbf{A} \cdot d\mathbf{k} \qquad \text{with} \quad \mathbf{A} = i \langle u(\mathbf{k})| \nabla_{\mathbf{k}} |u(\mathbf{k})\rangle . \tag{2.25}$$

The Berry phase is similar to the Aharnov-Bohm phase but is defined in the reciprocal space. $\mathbf{A}$ in the above equation is called the Berry connection, which resembles a vector potential from electromagnetism. So, we can define a Berry magnetic field or Berry curvature given by $\mathcal{F} = \vec{\nabla} \times \mathbf{A}$ and using Stokes theorem, we can write equation 2.25 as

$$\gamma_C = \oint_C \mathbf{A} \cdot d\mathbf{k} = \int_S \mathcal{F} d^2\mathbf{k} \tag{2.26}$$

Here, S is the surface of k-space connected to the contour C. Because of time-reversal(TR) symmetry, material systems can only take Berry phase values of either 0 or π. For trivial insulators, the Berry phase is zero, and for a topological insulator, it takes a value of π. In the following section, we look at the Integer quantum Hall effect to connect the Berry phase to the topological invariant of band structures [69].

2.4.3 Integer quantum Hall effect

The discovery of the integer quantum Hall effect(IQHE) by von Klitzing et al. in 1980 marked a turning point in CMP. In 2D electron gas (2DEG) systems, at strong magnetic fields, one observes precisely quantized Hall resistance plateaus in terms of fundamental constants, h, Planck's constant, and e, the charge of an electron [70–72] This precise quantization applies to even disordered or irregular samples. This is a result of the dissipationless 1D chiral edge states in these systems, which propagate in a single direction (based on the magnetic field direction) without backscattering. Thouless, Kohomoto, Nightingale and den Nijs (TKNN)

showed that the theoretical explanation of this phenomenon required the application of ideas from topology [71, 73]. The topological invariant for IQHE is the Chern number n, and it can be written in terms of Berry curvatures as[8, 71]

$$n = \frac{1}{2\pi}\int_{BZ} \mathcal{F} d^2\mathbf{k}. \tag{2.27}$$

Here, the Chern number n corresponds to the total Berry flux or phase in the whole Brillouin zone [8, 66], taking integer values. Like in the case of the genus g of the shapes from section 2.4.1, systems with different Chern numbers belong to topologically distinct classes and their band structures can not be smoothly transformed into each other. So, the interface between topologically distinct materials, the band gap needs to close, and this results in edge states. The IQHE conductance can be written in terms of Chern number n as $\sigma_{xy} = n\frac{e^2}{h}$. Since n can only take integer values by construction, which does not change under smooth variation of the Hamiltonian of the system, the IQHE effect is robust against local perturbations like defects [8].

2.4.4 Topological insulators

The Chern number for a material where TR symmetry is not broken is zero. However, with the theoretical advancements in topological band theory, a new type of invariant was introduced for case TR holds, namely the $\mathbb{Z}_2$ for systems with spin-orbit coupling [8, 74–76]. With the help of $\mathbb{Z}_2$, which takes two values, either $\nu = 0$ or $\nu = 1$, we classify materials into trivial and topological insulators. In 2D, we only need a single $\mathbb{Z}_2$ invariant to distinguish trivial ($\nu = 0$) and topological insulators (TIs) ($\nu = 1$). 2D-TIs or quantum spin hall insulators were first theorized by Kane and Mele in 2005 [77]. They later were theoretically proposed and experimentally observed in mercury telluride quantum well devices[78, 79]. To understand the band structure of a 2D-TI, we can use a simple schematic shown in figure 2.8(a). The sketch of the band structure of the semiconductor is shown in the left-most part of the diagram, showing both s (purple) and p (orange) orbitals [75]. In the case of materials with strong spin-orbit coupling, these s(purple) and p (orange) bands invert, and they can form an inverted bandgap with nontrivial topology, as shown in the second and third diagrams 2.8(a). Now, if we consider the edges of a topological insulator and a trivial insulator like a vacuum, and since here we have to go from $\nu = 1$ to $\nu = 0$, like in the case of IQHE, we will have metallic edge states connecting the two insulators due to bulk boundary correspondence [8, 75]. This is depicted in the rightmost diagram in 2.8(a). Unlike IQHE, in the case of 2D-TI, due to TR symmetry, the edge states are helical, meaning that, in a 2D-TI, opposite spins propagate in opposite directions.

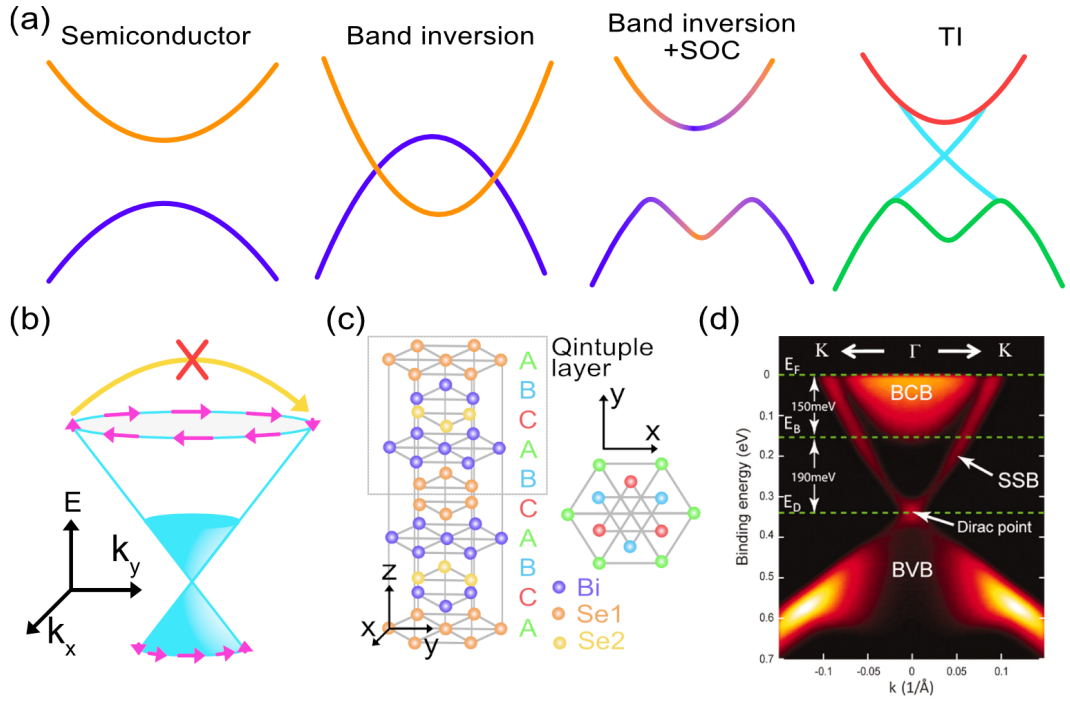

Figure 2.8: (a) Simple schematic showing band structure evolution resulting in the formation of a topological insulator. From left to right, the band structure of semiconductor, band structure showing band inversion, inverted band gap in the presence of strong spin-orbit coupling and band structure of TI showing TSSs along with bulk valence and conduction bands. (b) Dirac dispersion in a 3D-TI showing the special spin texture. TSSs are protected against backscattering, as indicated by the arrow, as the two sites have different spin orientations. (c) Crystal structure of Bi_2Se_3 showing quintuple layer and stacking. (d) An ARPES image of the band structure of Bi_2Se_3 showing both bulk bands and Dirac bands, adapted from [80].

In three dimensions, if we consider a cube, we would expect each surface to have an $\mathbb{Z}_2$ invariant associated with them. However, since these surfaces are not fully independent, we have in total there are four topological invariants given as $(\nu 0; \nu 1, \nu 2, \nu 3)$ [74, 81]. For instance, vacuum, which is topologically trivial, has variants (0;0,0,0). Out of these, the main invariant is $\nu 0$, which lets one classify materials into strong ($\nu 0 = 1$) and weak ($\nu 0 = 1$) topological insulators [8]. In weak topological insulators, the Fermi circle encloses an even number of Dirac cones, and they are not topologically protected. However, in the case of strong 3D-TI with $\nu 0 = 1$, one has an odd number of Dirac cones enclosed by the Fermi circle, and one of them will be uncoupled from others, allowing for protected topological surface states(TSSs) with special spin texture, as shown in figure 2.8(b) [8]. As seen here, the spin direction and propagation direction are locked together, and because of this, TSSs are protected against backscattering, as this would require a spin flip. The strong 3D-TI nature was first experimentally observed in $Bi_{0.9}Sb_{0.1}$ alloy, and later other materials like Bi_2Se_3, Bi_2Te_3, Sb_2Te_3, etc were identified [82].

In this thesis, we use Bi_2Se_3 with invariants (1;0,0,0), which is one of the most readily available 3D-TI materials. Bi_2Se_3 has a rhombohedral crystal structure and a monolayer of Bi_2Se_3 is formed out of a quintuple layer of two Bi and three Se layers as shown figure 2.8(c) [83]. Compared to other materials from the family Bi_2Se_3, it has a large bulk band gap of 0.3 eV and a simple band structure where the Dirac point is located at the $\bar{\Gamma}$ point well separated from the bulk valence band (BVB) and bulk conduction band (BVB). An angle-resolved photoemission spectroscopy (ARPES) image with the band structure of Bi_2Se_3, adapted from [80], is shown in figure 2.8(d). Though TIs are expected to have an insulting bulk, materials like Bi_2Se_3, Bi_2Te_3, Sb_2Te_3, etc., suffer from unintentional bulk doping due to defects. So, in these materials, the TSSs coexist along with bulk states, making the electrical transport analysis cumbersome [8, 36]. Over the years, compensation doping has been used to reduce the bulk contribution. However, this comes at the expense of electron mobility [15, 25–27, 29, 30, 32–34]. In our case, in order to reduce the bulk contribution to the electric transport by increasing the surface-to-volume ratio of the 3D TI, we use Bi_2Se_3 nanoribbons [84–86].

2.5 Probing topological properties using superconducting devices

The Dirac equation, which describes a relativistic spin half particle, is one of the most celebrated equations in physics [1]. It predicted the existence of antiparticles of fermions, which are distinct from the fermion itself. This led to the discovery of positron, the anti-electron, by Carl D. Anderson in 1933 [2] and other anti-matter particles. In 1937, Ettore Majorana devised an elegant modification to the Dirac equation that predicted a particle that could be its own antiparticle [3], namely Majorna fermion. In terms of second quantization, notation this means that $\gamma = \gamma^\dagger$, where $\gamma^\dagger$ (γ) corresponds to the creation operator (annihilation) operator for Majorana fermions. As of now, there has not been any experimental evidence for any elementary particle being a Majorana Fermion. The field of condensed matter physics(CMP) is known for the ability to host various collective excitations or quasiparticles, like phonons, excitons, polarons, magnons, and skyrmions, which do not exist in free space. Recent theoretical advancements in condensed matter physics identified some material systems where one could have quasiparticles, which are its own holes [9–13, 87–89]. Such excitation is believed to follow non-Abelian statistics or, in other words, exchanging (or braiding) two such particles has a non-trivial outcome, unlike the fermions or bosons, which get their wavefunctions multiplied by a factor of -1 or +1, respectively. There has been growing interest in detecting Majorana Fermions in material systems, as they might be able to pave a path towards topologically protected quantum computing [5–7].

As Majorna fermions are their antiparticle, the CMP version of them can be thought of as an equal superposition of electrons and holes [8, 11, 88, 89] A natural place to look for them is in superconductors, as the Boguliubov quasiparticle have both electron and hole component. In an s-wave superconductor, the quasiparticle can be written as $b = uc_{\uparrow}^{\dagger} + vc_{\downarrow}$, where $c^{\dagger}(c)$ is the fermion creation (annihilation) operator and u and v corresponds to the weight of electrons and holes respectively. Now, $b^{\dagger} = v^{*}c_{\downarrow}^{\dagger} + u^{*}c_{\uparrow}$ and this is distinct from a b. To get the Majorana condition, we need to have a spinless superconductor. In case of a spinless superconductor with spin-triplet (or p-wave) pairing such that quasiparticlecan take the form $\gamma = uc_{\uparrow}^{\dagger} + u^{*}c_{\uparrow}^{\dagger}$, then we have $\gamma = \gamma^{\dagger}$, which is Majorana fermion [11, 88]. Although Sr_2RuO_4 is predicted to have p-wave pairing and Majorana fermions are expected to occur at vortices, it has not been confirmed experimentally [11, 88–90].

With the advent of topological materials like topological insulators, there have been predictions for observing various hybrid devices involving s-wave superconductors and unconventional metals like topological insulators to nanowires with high spin-orbit coupling [8–11]. In particular, hybrid S-TI-S junctions with TSSs are expected to provide a platform for hosting Majorana Bound States (MBSs) [8–11, 89]. When a conventional BCS superconductor with s-wave symmetry of the order parameter is placed in contact with an unconventional metal like TI with Dirac surface states, the induced superconducting gap of the TI can be topological at certain conditions [8–10]. Fu and Kane showed that the proximity-induced superconductor could have an order parameter with an $p_x + ip_y$ symmetry, and S-TI-S junction formed out of such unconventional superconductors can support MBSs at zero energy at a phase bias of π, as part of ABSs that transport the charge across them [9–11, 91, 92].

Moreover, as discussed at the beginning of this Chapter, even though TIs are expected to be bulk insulating with conducting TSSs, most of the easily available ones, i.e. the family of Bi_2Se_3, come with unavoidable bulk conductivity due to vacancy defects [8, 36]. So, detecting the signatures of TSSs with transport measurements is challenging. This is because the bulk states in TI materials usually show diffusive transport, and if we implement them in an S-TI-S junction form, the current contributions from the diffusive bulk states will be lower (assuming short junction limit $I_c^{diff} = 2.07\Delta/eR_N$), compared to ballistic states (assuming short junction limit $I_c^{ball} = \pi\Delta/eR_N$) that might originate from TSSs. This way, we can detect some signatures of TSSs using supercurrent transport.

In the following, we will look at some of the details of having MBSs in an S-TI-S junction and will discuss briefly how to detect them.

2.5.1 Majorna bound states in TI-superconductor hybrid devices

Consider an S-TI-S junction as shown in figure 2.9(a). Assume that the Fermi level is close to the Dirac point of the TI, and all transport contributions come from TSSs with linear dispersion relation. Now, The ABS corresponding to an electron with spin up travelling normal to the superconducting electrodes with a wavevector having $k_y = 0(\ \theta = \tan^{-1}(k_y/k_x) = 0\ )$ is shown 2.9(b) [32, 87, 92]. In this case, due to the special spin texture of TSSs, due to forbidden backscattering, this would require a spin flip. So, this zero-angle mode is always transmitted with a probability of 1. Since we induced superconductivity in a topological material to form the junction, the zero angle mode is MBS at the phase of $\varphi = \pi$, which is a ground state excitation of topological superconductor, rather than conventional ABSs [87, 92]. The dispersion relation of the MBS, in general, can be written as [93]

$$E_m^{\pm} = \pm\sqrt{\tau_m}\Delta\cos\left(\frac{\varphi}{2}\right) \tag{2.28}$$

Here, $E_m^{\pm}$ corresponds to energies of MBS with different parity and τ_m is the transmission probability of the MBS and for an S-TI-S junction $\tau_m = 1$ [87, 92]. The τ_m in an S-TI-S junction could be controlled by adding magnetic materials on top of the TI-weak link, allowing one to protect the MBS from continuum states [93]. The dispersion relation of the MBS is plotted in figure 2.9(c) with various τ_m values for comparison. Here, the only difference in bound state spectrum between various τ_m is in the reduction in amplitude. The most striking feature of MBS dispersion is that, unlike the case of ordinary ABSs, they are 4π periodic. Though two energy levels cross each other at a phase value of π, since they have opposite parities, transitions between them are forbidden. But if there are parity-switching events like quasiparticle poisoning, this will not hold. So, if there are no parity switching events, we should observe a 4π periodic Josephson effect from MBS [9, 94].

The 4π periodicity of MBS can be seen by taking the derivative of the MBS dispersion to obtain the CPR as

$$I_m = \frac{2e}{\hbar}\frac{\partial E_m}{\partial\varphi} = \frac{2e}{\hbar}\sqrt{\tau_m}\Delta\sin\left(\frac{\varphi}{2}\right) = I_{m0}\sin\left(\frac{\varphi}{2}\right). \tag{2.29}$$

The 4π periodic CPRs of MBS with various τ_m values are plotted in figure 2.9(d). So, to detect MBSs, we have to look for signs of 4π periodic Josephson effect. Now, any other bound state that propagates at an $\theta \neq 0$ is a conventional Andreev Bound State [87, 92]. So, in an S-TI-S junction, the MBS are expected to coexist alongside conventional ABSs with 2π periodic bound states spectrum.

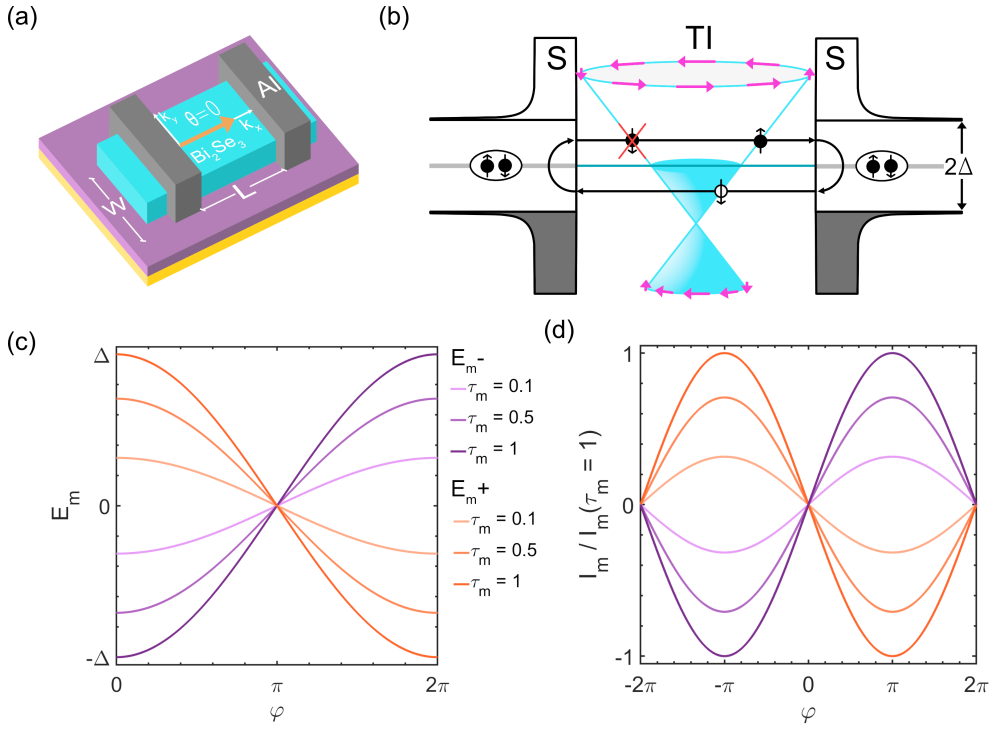

Figure 2.9: (a) Sketch of an S-TI-S junction showing the $k_y = 0$ MBS. (b) MBS in an S-TI-S junction shows protection against backscattering of the TI-weak link due to spin momentum locking. This mode, which travels normal to the superconducting electrodes, is thus always transmitted. (c) Energy dispersion of MBS with different τ_m values. For S-TI-S junction $\tau_m = 1$. (d) Plot showing the CPR of MBS for different transmission probabilities.

2.5.2 Fabry-Pérot resonace and transmission probability of an S-TI-S device

In an S-TI-S junction, we can have a chemical potential mismatch between the section of the TI covered by the superconductor (or normal electrodes) and the bare TI part that forms the weak link. We can think of this situation as an electrical equivalent of the well-known Fabry-Pérot(FP) cavity from optics. Here, instead of photons, we have our electron wave, and instead of mirrors, we have a barrier formed due to the chemical potential mismatch at the interface [21, 95]. A simple schematic showing FP cavity in an S-TI-S junction is figure2.10(a). For the general case, we will assume that the junction is in a normal state as this has nothing to do with superconductivity or TSSs and can be applied to other devices with two semi-transparent interfaces [95–97]. Also, assume that the Fermi wavelength (λ_F) needs is smaller than the length l of the junction so that it can fit electron waves. Now, electron waves shown in green and red going to the right electrode can interfere if their phases are coherent. For constructive interference,

we have the condition, $2lk_F = 2\pi n$, where k_F is the Fermi wavevector, l is the length of the junction and n is an integer [95–103]. Such interference of electron waves can be seen as periodic oscillations of conductance as a function of the gate voltage or bias voltage of the device [95–97]. FP conductance oscillation has been experimentally observed in various quasi-1D systems, including carbon nanotubes, quantum Hall edge states, semiconducting nanowires, and graphene nanoribbons, etc [95–103].

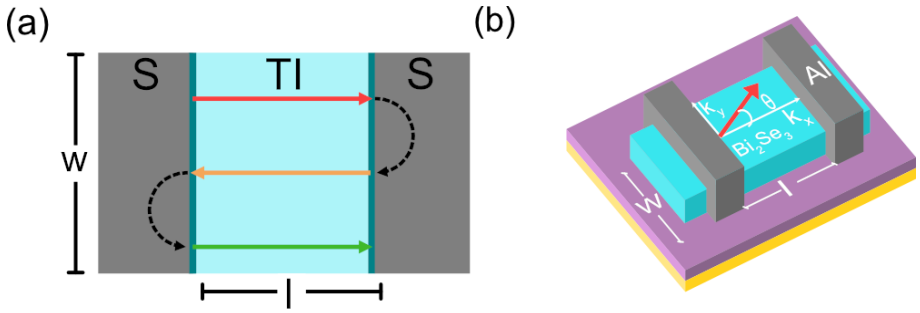

Figure 2.10: (a) Schematic of an S-TI-S junction showing barrier at the S-TI interface due to chemical potential mismatch. Red, yellow and green correspond to charge carriers undergoing reflection at the barrier to create FP resonance in conductance. (b) Sketch of an S-TI-S junction showing a mode travelling $\theta = \tan^{-1}(k_y/k_x)$, which would result in a conventional ABS.

Now, in the case of Dirac materials, because of the presence of the linear dispersion that protects against backscattering, the transport across an S-TI-S junction can have FP transmission resonance due to Klein tunnelling. [21, 104] The periodicity of FP resonances in terms of chemical potential is given as $\Delta\mu = hv_F/2l$, where v_F corresponds to the Fermi wave velocity. Whenever the k_x component of the wavevector(k) of transport modes, shown in figure 2.10(b), satisfies the FP resonance condition, we have higher transmission through the junction. This can be seen in the angle ($\theta = \tan^{-1}(k_y/k_x)$) dependence of the transmission probability of the junction given by $\tau_{\mu r} = 1 - |r|^2$, with [21, 104]

$$r = 2e^{i\phi}\sin(k_x l)\frac{\sin(\phi) - \sin(\theta)}{e^{-ik_x l}\cos(\phi+\theta) + e^{ik_x l}\cos(\phi-\theta) - 2i\sin(k_x l)} \tag{2.30}$$

Here, $\phi = \sin^{-1}(\mu_r \sin\theta)$ with $\mu_r = \mu_{wl}/\mu_{el}$ being the ratio of chemical potential μ_{wl} at the weak link to the ratio of chemical potential at μ_{el}. Though this was originally derived for graphene, it can applied to TI materials as well [104].

We calculated the transmission probability $\tau_{\mu r}$ of various modes in Al-Bi_2Se_3-Al junction of length $l = 100$ nm, width $w = 300$ nm, and thickness $t = 20$ assuming $\mu_r = 0.5$ and a typical k_F value of 0.55 nm^{-1}. The resulting polar plot is shown in 2.11 (a) as orange curve. Here, one sees the oscillation of transmission resonance with respect to θ. For lower angle modes, the oscillation has a lower amplitude,

and $\tau_{\mu r}$ values are close to one. But at higher angles, it oscillates with higher amplitudes and goes close to $\tau_{\mu r} = 0$. To get an idea of how it affects the ABSs in this junction, we have plotted $1 - E_{gap}/\Delta$, where E_{gap} is the gap in the ABS spectra at phase π [21]. Here, we see that the mode at $\theta = 0$ is gapless, and there are also some modes with very small gaps, and depending on the value of temperature, we might perceive them as gapless in our measurements [21].

Even though equation 2.30 provide the transmission probability of various modes in an S-TI-S junction, the in adds an extra parameter to the analysis, namely μ_r. So, throughout this thesis, we assume an extreme chemical potential mismatch between our weak link and electrodes and, in this case, the equation for transmission probability simplifies to [105, 106],

$$\tau = \frac{k_x^2}{k_x^2 \cos^2(k_x l) + k_F^2 \sin^2(k_x l)}. \tag{2.31}$$

To provide a comparison between τ (blue curve) and $\tau_{\mu r}$ from before, we have plotted them in figure2.11(b) with the same junction parameters asin figure 2.11(a) with various μ_r values (curves with shades of orange). As seen here for lower μ_r value, both the expressions start to converge.

In the case of TI nanoribbon-based devices, one can have transversal quantization along the k_y direction due to the size as $k_y = 2\pi(n + 1/2)/P$, where n is an integer and $P = 2(w + t)$ is the perimeter of the TINR [91, 107, 108]. One of the immediate effects of this is that, instead of the continuous spectrum of τ value covering all angles, we will have a mode with discrete θ values or, in turn, τ values. But even more importantly, we have an additional factor of 1/2 in the equation, arising from the Berry phase picked up by the Dirac fermion while circulating around the nanoribbon [107], and this has a huge impact as this means we no longer have the $k_y = 0$ mode. The Dirac dispersion will form into subbands with energy spacing given by [91, 107, 108],

$$E_n = \pm\hbar v_F \sqrt{k_x^2 + \left(\frac{2\pi(n + 1/2 - \Phi/\Phi_0^N)}{P}\right)^2} \qquad \text{with} \qquad \Phi_0^N = \frac{h}{e}. \tag{2.32}$$

The energy dispersion of a TI nanoribbon with $P = 100$ nm, assuming $v_F = 5.5 \times 10^5$ m/s for Bi_2Se_3, is plotted in figure 2.11 (d) and (e) for $\Phi = 0$ and $\Phi = \Phi_0^N/2$ respectively. As seen here, to get back to the case of no energy gap that supports MBS, one needs to apply flux of $\Phi_0^N/2$ along the axis of the nanoribbon. It is important to mention here that we did not apply any axial magnetic field in any of our measurements. Now, in figure 2.11(c), we have plotted the transmission probabilities of two devices with length $l = 100$ nm, thickness $t = 20$ and width of 150 nm (magenta circles) and 300 nm (orange circles), respectively, assuming transversal quantization. As seen here, depending on the width of the junction, the number of modes and the transmission probabilities of the modes change.

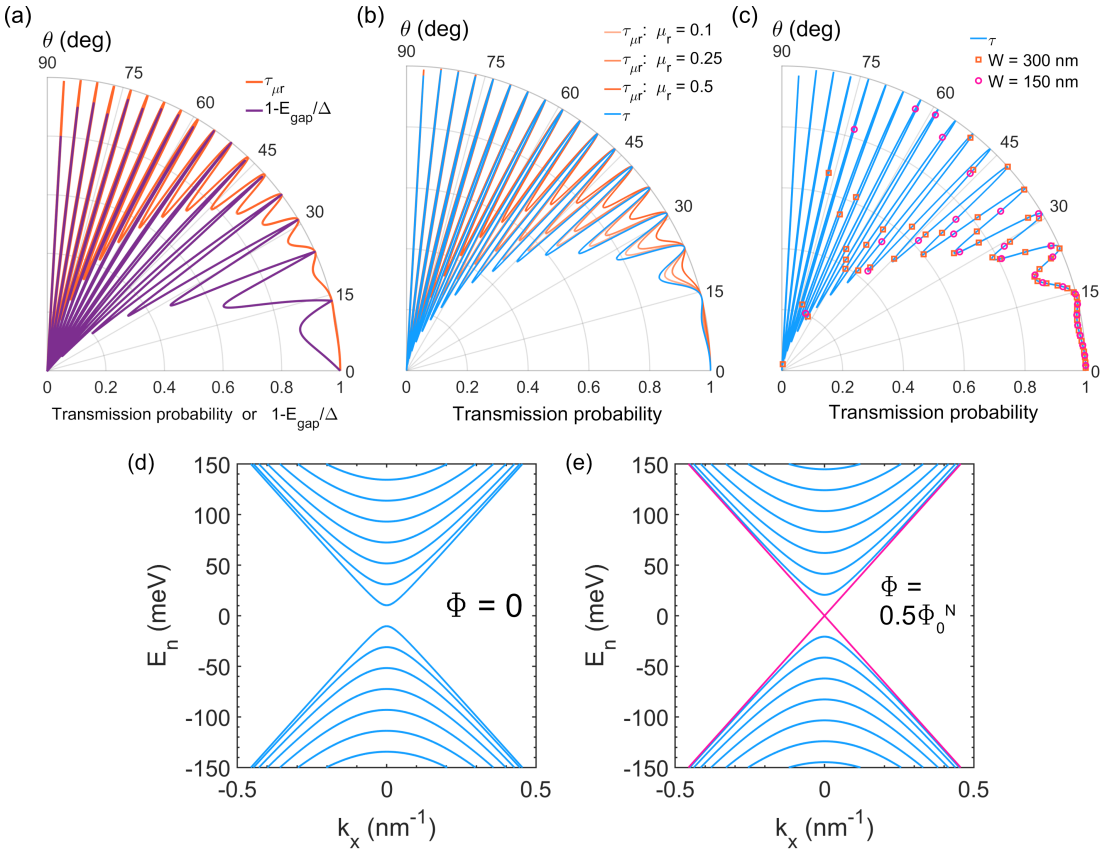

Figure 2.11: (a) Angle dependent ($\theta = \tan^{-1}(k_y/k_x)$) transmission probability $\tau_{\mu r}$ (ornage) and $1 - E_{gap}/\Delta$ (purple) calculated for device of with $l = 100$ nm,$w = 150$ nm and $t = 20$ nm assuming $\mu_r = 0.5$. (b) Transmission probability calculated using equation 2.44 with various μ_r values (shade of orange) along with the curve assuming extreme Fermilevel mismatch (blue) calculated using equation 2.45. (c) Plot showing discrete τ values for devices with two different widths, 150 nm (orange) and 300 nm(magenta), in the presence of transversal quantization. The blue line is the same as the previous plot. Energy dispersion of Dirac surface state in the presence of transversal quantization result in subbands with (d) gap in the spectrum for $\Phi = 0$ and (e) gapless spectrum for an applied external flux of $\Phi = 0.5\Phi_0 n$. In the case of transversal quantization, applying an axial magnetic field to compensate for the contribution due to the Berry phase is essential to have MBS in S-TI-S junctions.

2.5.3 Detecting Majorana bound states

As seen in the previous section, S-TI-S junction has the potential to host MBS, and they should have 4π periodic bound state spectrum and a corresponding 4π periodic CPR. For observing MBS, we need to look for Josephson effects with 4π periodic CPR signatures [106]. Ideally, pure MBS in a junction will result in a Fraunhofer pattern with $2\Phi_0$ periodicity, which will emit Josephson radiation at a frequency $f_J/2$, which is half of the Josephson frequency and thus will also show

twice the voltage spacing in Shapiro steps etc [106]. However, it is important to note here that, in a measurement, if the temporal variation of the phase across the junction is slower compared to the inelastic scattering time or the quasi-particle poisoning time, one will not observe any 4π periodic Josephson effect, and in this case, the 2π periodicity of the CPR will be restored [9, 94]. Because of this, DC measurements, which are in general slow, will not be sufficient to detect MBS, and it is essential to use microwave-based measurement to characterize topological insulator-based junctions[9, 94].

2.5.4 Advancements in hybrid S-TI-S junctions

Over the past decade, Josephson junctions based on TI materials have been fabricated and extensively studied experimentally to look for signatures of topological superconductivity in these systems. Some of the studies based on TI systems can be found in [17–21, 23, 27, 32, 35, 109–111]. Unfortunately it is impossible to discuss them all here. The DC measurements that tried to observe the 4π periodic Josephson effect in S-TI-S junctions included CPR extractions using biased asymmetric DC-SQUIDs [17, 18, 27, 109, 110], and Fraunhofer pattern measurements of single junctions [110, 112–114], phase-controlled junctions [24], etc. Since now known that DC measurements are not sufficient for detecting MBS, the recent studies based on TI-junctions primarily focus on Shapiro step measurements at frequencies larger than any relaxation or poisoning rate [19–21, 23, 32, 35] or microwave probing of phase-biased Josephson junctions [115] or measurements of Josephson readiation[116]. In the case of Shapiro steps measurements, missing odd integer steps were reported, and this pointing toward the possible presence of 4π periodic modes in TI junctions [19–21, 23, 32, 35, 111, 117, 118]. Deacon et al. observed emission of radiation at half the Josephson frequency in HgTe-based gate-tunable junctions and this maybe points towards 4π periodic Josephson effect in the junctions [116]. Also, Murani et al., performed AC susceptibility measurements in an Bi based Josephson junction coupled to a multimode resonator, and the observed losses attributed to the junction admittance at phase bias of π may have been a signature of gapless topological bound states [115]. Now, it is essential to point out that the undisputed signature of Majorana-bound states is yet to be reported.

2.6 Al-Bi_2Se_3-Al junctions at Chalmers

In this section, we quickly discuss the progress with Al-Bi_2Se_3-Al made at Chalmers before the beginning of this PhD study to add more context. Since TI materials like Bi_2Se_3 are known to have doped bulk carriers, we make use of nanoribbons in our studies to have a higher surface-to-volume ratio and thereby reduce bulk contributions. The Bi_2Se_3 nanoribbons used in our studies were grown at the

Institute of Chemical Physics, the University of Latvia, by our collaborators using a physical vapour deposition technique. The details of the growth process and magnetotransport characterization of these nanowires can be found in [84–86]. From the magnetotransport characterization, we know that in our Bi_2Se_3 nanoribbons, we have TSSs coexisting along with bulk carriers and carriers due to an interfacial 2DEG formed at the bottom interface of the TI-nanoribbon which is in contact with the substrates. In these measurements, only surface states from the top surface of the nanoribbon are visible, and the bottom ones are masked by the accumulated 2DEG. The Fermi level of the top TSSs states are located roughly 170-190 μeV above the Dirac point. The typical values of various parameters we get from these measurements are summarized in the table 2.2. Also, from Shubnikov-de Haas (SdH) oscillations, we get the mobility values of roughly 7000 $cm^2V^{-1}s^{-1}$ and 2000 $cm^2V^{-1}s^{-1}$ for top surface states and trivial 2DEG respectively.

n_{TS} (cm^{-2})	n_{Int} (cm^{-2})	n_B (cm^{-2})	E_F^{TS} (meV)	E_F^B meV	k_F (nm^{-1})
2.1-2.6×10^{12}	1.5-3.8×10^{13}	1-4×10^{18}	170-190	40-60	0.55

Table 2.2: Typical values of various parameters of Bi_2Se_3 nanoribbons used in this study (adapted from [85]). Here n_{TS}, n_{Int}, n_B correspond to the carrier densities of the Dirac surface states at the top, the accumulated interlayer 2DEG and bulk carriers, respectively. Also, E_F^{TS} and E_F^B correspond to the location of the Fermi level for surface states and bulk, respectively, and k_F corresponds to the typical value of the Fermi-wave vector.

2.6.1 Highly transparent Al-Bi_2Se_3-Al

Following the works on various TI-based junctions [16, 119–121], Kunakova et al. experimentally demonstrated highly transparent Al-Bi_2Se_3-Al devices fabricated on TINRs. A summary of the main results from this work is provided in figure 2.12 [22]. An SEM image and schematic of the S-TI-S junction are shown in the figure 2.12(a) and (b), respectively. As seen in the top part of the schematic, these junctions can be described as SIS'I'-N-I'S'IS junctions, where S corresponds to the Al electrode with superconducting gap Δ, S' being the proximized superconductor inside the TI with an induced superconducting gap Δ', N is the normal part representing the bare TI section of the junction and I and I' corresponding to the barrier between the S and S' and S' and N respectively. A typical IVC of the device measured on one of the junctions is shown in figure2.12(c), showing the hysteric behaviour of our junctions. This is assumed to have its origin in elevated electron temperature after the junction switches to the normal state. The junction typically shows an induced gap 160-175 μeV and an I_cR_N product ranging from 20-180 μV [22]. Since the value-induced gap Δ' is very close to Δ_{Al}

of Al, we usually model these junctions as 2D planar junctions of the S'I'-N-I'S' for simplicity as given in the bottom section of figure 2.12(b) [22].

In all our advice, we have an excess (I_{exc}) pointing towards the Andreev reflection process in these junctions. Using the Flesberg model to connect the I_{exc} to the transparency of the I' interface of these junctions, one finds typical values ranging from 0.65-0.85. The conductance spectra of one of the junctions for various temperatures are shown in figure2.12(d), and here one can see dips in the spectra at voltage value $V = 2\Delta'/en$, with n being an integer. This is due to the MAR process in our junctions, and together with I_{exc}, they demonstrate the high transparency of these junctions [22]. In figure 2.12(c), the extracted conductance dips corresponding to voltage values of $2\Delta'$, Δ' and $2\Delta'/3$ are plotted as a function of temperature, and solid lines correspond to fits of Δ' made using the formula [58, 122, 123]

$$\Delta'(T) = \frac{\Delta_{Al}}{1 + \gamma\sqrt{\Delta_{Al}^2(T) - \Delta'^2(T)}/K_B T_c}, \tag{2.33}$$

with $\gamma \propto R_B/\rho_N\xi_N$, ρ_N and ξ_N being the resistivity and coherence length of Bi_2Se_3 nanoribbon respectively and R_B the resistivity of the interface I between Al electrode and Bi_2Se_3. For the fitted curve shown figure2.12(e), $\gamma = 0.5$ and typical value of γ for Al-Bi_2Se_3-Al junctions ranges in between 0.2-0.9 [22].

2.6.2 Missing first Shapiro step Al-Bi_2Se_3-Al

Now, we will look at Shapiro step measurements performed on Al-Bi_2Se_3-Al. Though it is common to see reports of S-TI-S junctions with attenuated odd Shapiro steps in the literature, most of the junctions measured at Chalmers did not show this feature. The data from one of the devices (B53-41) that showed missing the first Shapiro step is provided in figure 2.13. The most important distinction between device B53-41 and the devices that did not show the missing odd step is in the width. Device B53-41, with a length of 80 nm and width of $5\mu m$ fabricated on an STO substrate (uses layout B, see Chapter 3 for more), is one of the widest nanoribbon-based Al-Bi_2Se_3-Al single junctions measured in our group. In general, we do not prefer very wide single junctions as they tend to have high critical currents and a large number of transport modes. So, if we were to employ them to study unconventional nature in our junctions, any unconventional signatures would be masked by a large number of conventional bound states.

The IVC of the device is shown in figure2.13(a), and the junction has an I_c of 28.4 μA and $R_N = 5.5\Omega$. Figure2.13(b) and (c) show the maps of the conductance plotted as a function of DC voltage and microwave power at two different RF irradiation frequencies, 1.56 GHz and 1.91 GHz. At 1.56 GHz, we can see the first odd Shapiro step is missing, and it reappears at a frequency of 1.91 GHz. Now, by taking 1.91GHz as the threshold frequency ($f_{4\pi}$), we can estimate the

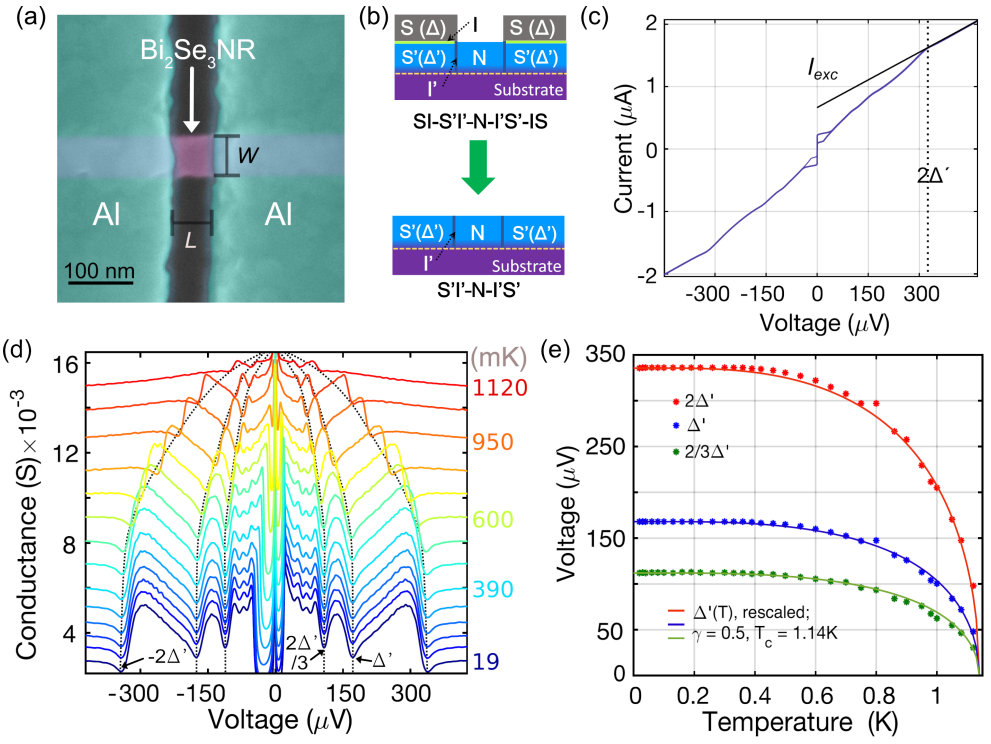

Figure 2.12: (a) Colored SEM image of fabricated Bi_2Se3 nanoribbon Josephson junction (b) Schematic representation of a planar 3D TI Josephson junction. The superconducting electrodes (S) that induce superconductivity in the 3D TI underneath, indicated as S', are shown in grey. The green line indicates the barrier I between S and S', while the dark grey region shows the barrier I' between S' and N representing the part of the 3D TI not covered by the electrodes. For large enough transparency between the 3D TI and Al, one can model the system as a planar 2D junction (lower panel). (c) IVC of the junction B45-C1 measured at 20 mK. The solid black line is a linear extrapolation to zero voltage used to extract the excess current I_{exc}, while the black dotted line indicates the value of twice the induced gap Δ' .(d) (dI/dV) as a function of bias voltage for junction B45-C1 measured at various temperatures. (e) Temperature dependence of the first three dips in the conductance spectra n = 1; 2; 3 (corresponding to $2\Delta'$; Δ' ; $2/3\Delta'$). The solid red, blue, and green curves are the calculated temperature dependences of the induced gap $\Delta'(T)$ in agreement with the equation, considering the parameter γ =0.5 and that the Tc of the junction is 1.14 K. The calculated curves are scaled to the experimentally determined Δ' for n = 2 (adapted from [22]).

maximum amount of 4π periodic current that might be carried by the junction as [32], $I_{4\pi}^{max} = hf_{4\pi}/2eR_N \simeq 70$ nA which is roughly 400 times smaller than the I_c of the junction. This might have to do with the junction being really wide and thereby supporting more regular transport modes.

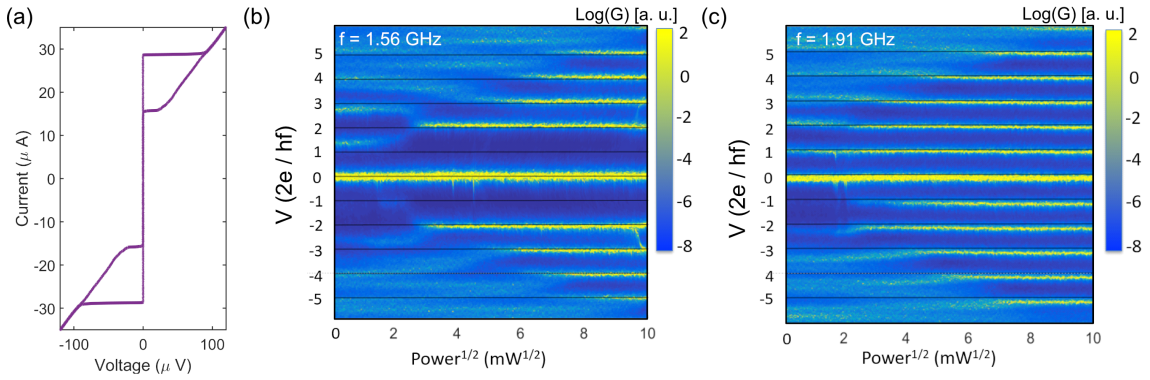

Figure 2.13: (a) IVC of a wide Al-Bi_2Se_3-Al junction (B53-41) measured at 20 mK with length, L = 80 nm and width, W = 5μm. Conductance map showing Shapiro steps as a function of normalized DC voltage and applied microwave powder at a frequency of (b) 1.56 GHz with missing first Shapiro step and (c) 1.91 GHz with reappearance of Shapiro step [This figure is based on measurements by Gunta Kunakova and Thilo Bauch].

Motivations for this thesis

Compared to some of the state-of-the-art S-TI-S junctions based on MBE-grown TINRs with in-situ desposited epitaxial superconductors, our junctions are rather modest in terms of technology. As discussed above, we use nanoribbon grown with a simple PVD technique along with an ex-situ deposited superconductor with e-beam evaporation technique. Kunakova et al. showed Al-Bi_2Se_3-Al with high transparencies [22]. But, from magnetotransport, we know that apart from TSSs, there are substantial amounts of carriers in our nanoribbon originating from the bulk carrier and trivial 2DEG [85]. How much of the supercurrent is carried by TSSs? Which transport regime are our junctions in? Why do we not observe missing odd Shapiro steps in our narrow junctions? A recent experiment by Rosenbach et al. showed a similar width dependence of missing Shapiro steps in BSTS-based junctions and pointed out it could have been due to transversal quantization [32]. Could it be the case in our junctions? From the angle-dependent transmission probabilities of TI surface states discussed in the previous section, we saw that there could be transport modes with transmission probabilities very close to 1. Do we have these modes in our junction? If so, can we detect them?

Through this thesis, we try to answer these questions. By doing so, we hope to improve our understanding of S-TI-S junctions in general and the nature of transport phenomenology in them.

3 Fabrication and experimental techniques

In this chapter, we will discuss the device fabrication process and measurement setups used as part of this thesis. In the first section, we will go through the DC devices and their fabrication, and then we will discuss the design considerations and fabrication procedures used for making devices for microwave measurements. In the second section, we briefly describe the setups used for both DC and RF measurements. We will also provide an example of fitting resonance data of CPW resonators that are inductively coupled to TI-based RF-SQUIDs.

3.1 Device Fabrication

3.1.1 Fabrication of S-TI-S Junction devices for DC measurements

Junction layout

Throughout the thesis, we use two different S-TI-S junction layouts. We will refer to them as layout A and layout B. In the case of layout A, the two Al-electrodes of the junction are placed parallel to the transverse direction of the topological insulator nanoribbon(TINR), as shown in figure 3.1(a). Here, the separation between the electrodes of the junction defines the junction length, and the width of the TINR defines the width of the junction. As a result, we only have control over the length of the junctions and the widths of junctions are fixed by the width of TINRs. In this layout, the transport will be very well confined within the region between the two electrodes, and we can have transport modes that go around the perimeter of the TINR along the transversal direction. A sketch of a junction with layout B is shown in figure 3.1(b). Here, the two Al-electrodes of the junction are placed parallel to the axis of the TINR. In this case, the width and separation of the Al electrodes define the width and length of the junction, respectively, which can be controlled lithographically. Unlike layout A, here the ends of the junction are open, and we do not expect any modes that go around the perimeter of the TINR as the path around the TINR will be extremely long (about 20-40). Figure 3.1(c) and (d) show SEM images of fabricated S-TI-S junctions with layouts A and B, respectively.

Fabrication Process

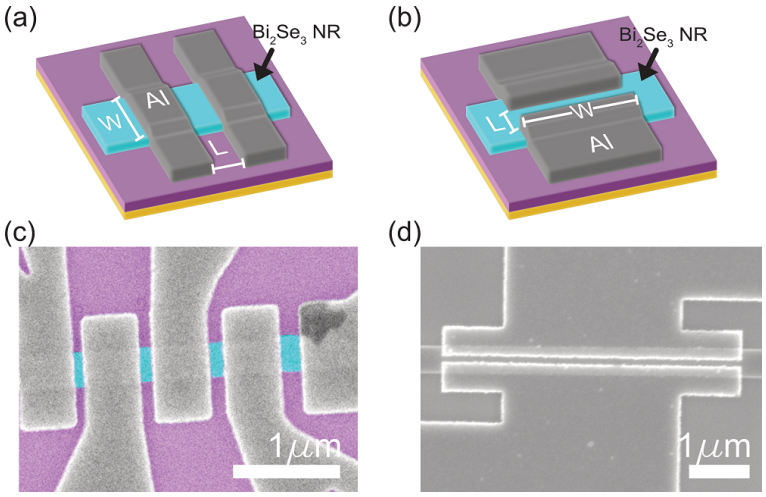

Figure 3.1: (a) Schematic depicting a TI-junction with layout A. Here, the Bi_2Se_3 nanoribbon is shown in cyan, Al electrodes are shown in grey, and the substrate is shown in purple. This device allows modes that go around the perimeter of the TINR. (b) Schematic showing a TI-junction with layout B. Since the ends of the junction are open in this layout, these device does not support transport modes that go around the TINR.(c) and (d) SEM images of fabricated Al-Bi_2Se_3-Al junctions with layout A and layout B, respectively.

For fabricating the Al-Bi_2Se_3-Al Junction devices, we use pre-patterned SiO_2(300 nm)/Si or STO or sapphire substrates with alignment marks for e-beam lithography (EBL). In the usual transfer process, the TINRs are transferred from the growth glass plate to the substrates by bringing them in contact or by using cleanroom tissue paper cut into triangles to pick TINRs and place them on the substrate. After the transfer process, the TINRs for device fabrication are identified with the help of an optical microscope and (or) atomic force microscopy (AFM). The patterns for EBL are made using AutoCAD software, and the EBL exposures are done following the recipes given in Appendix B. In all EBL recipes involving TINRs, the baking temperature and time per resist layer are limited to 130°C and 2 minutes, respectively, to limit degradation of the TINR. After the development of the sample, we use optical microscopy to assess the quality of the process. Then we use a very mild oxygen plasma (25 W, 50 mbar, 5s) to clean any remaining resist residue. Then, the chips are loaded into an Ar ion beam etching (IBE) machine and etched at an angle of 5° for 30s to remove the native oxide from the surface of the TINRs before deposition of contacts. We perform this for every device we fabricate. Now, prior to venting the load lock of the IBE chamber, the load lock of the e-beam evaporator used for metal evaporation is opened to allow for quick sample loading. Thereafter, the samples are quickly taken out of

the IBE machine and loaded into e-beam evaporator within a minute to reduce re-oxidation of the etched surface. As a final step, contact layers consisting of Pt (3nm)/ Al (80-120 nm) are deposited, and the samples are lifted off in hot acetone at 50°C.

3.1.2 Suspended S-TI-S Junctions with local gates

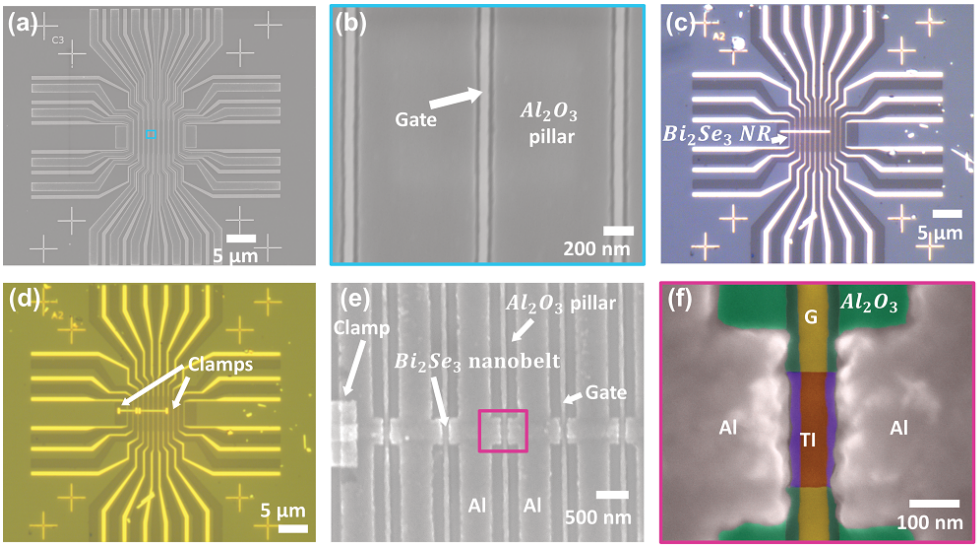

Figure 3.2: (a) SEM image of the gates structures along with support pillars. (b) zoom-in on the area of the SEM image from panel (a) marked with a blue rectangle. Here, one can see the gate structures with a width of $\simeq$ 50 nm in between the gaps (100 nm) of Al_2O_3 support structures. (c) Optical image after the deposition of Bi_2Se_2 nanoribbons using PDMS-assisted transfer. (d) Optical image showing TINRs clamped down after first EBL and metal(Ti(5nm)/Au(80-100nm)) deposition. (e) SEM image after depositing Al electrodes. (f) Zoom-in on the area of the SEM image from panel (e) marked with a magenta rectangle showing a single suspended S-TI-S junction.

To make the suspended junctions, we use pre-patterned sapphire substrates with alignment marks as well as local gate electrodes (Ti(5 nm)/Au(25 nm)/Pd(5 nm)) and Al_2O_3 support pillars. The pillars are raised by an amount of 18 nm compared to the gate electrodes to allow airgap for gating. The nanoribbons are deposited on the gate-pillar structures using either the substrate contract method or the PDMS-assisted transfer technique. PDMS-assisted transfer is already established for 2D materials, and we used commercially available PDMS films from Gel-Pak [124]. Unlike the commonly used PDMS for mechanical exfoliation with a higher retention level X4 (a way of Gel-Pak to quantify adhesion or amount of dangling bonds), we use PDMS stamps with X0 grade with a lower retention level to reduce polymer residue. The stamping process utilizes an aligning microscope

with a homemade attachment. We found that sometimes the TINRs curl up during the stamping process, and with the spinning of a layer of resist on top, they relax back to normal conformation. So, after the transfer, we do a first step of EBL, followed by metal evaporation (Ti(5nm)/Au(80-100nm)) to let the TINRs relax and then hold them in place with clamps for improved alignment accuracy in the junction defining step. This also allows us to clean the surface of the nanoribbons before defining the junctions. For this, we use hot acetone at 50°C followed by an IPA dip and nitrogen drying. Then, another step of EBL followed by evaporation of Pt (3nm)/ Al (100-120 nm) is performed, as in the case of normal junctions, to get the suspended junctions. The different stages of this fabrication process are shown in figure 3.2.

3.1.3 Gated devices with h-BN dielectric

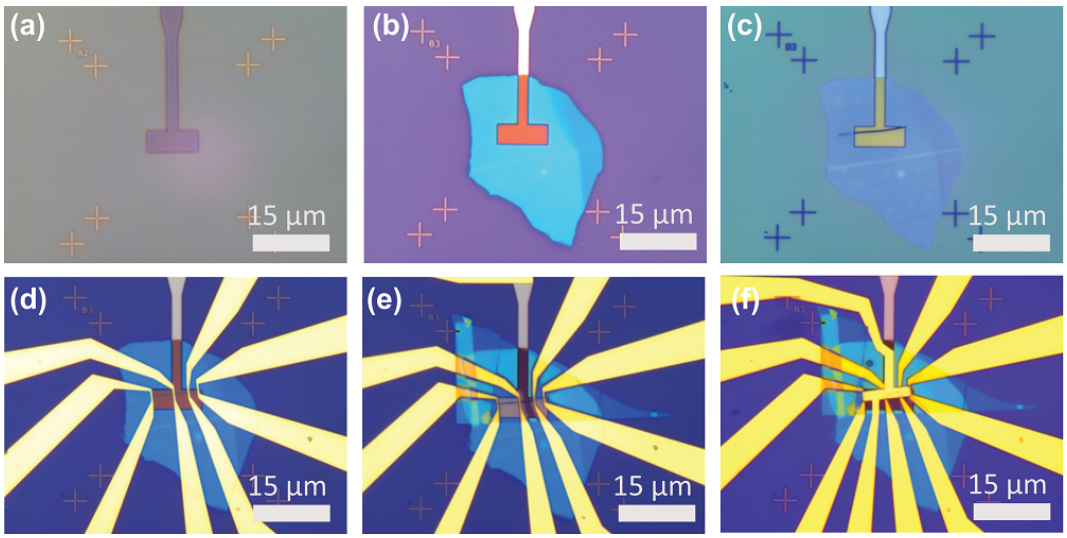

Figure 3.3: Images showing various fabrication steps involved in making h-BN gated TI devices. Optical images taken after (a) defining the backgate electrode, (b) after the first h-BN stamping step for the bottom gate, (c) after placing the TINR, (d) after defined electrical contacts, (e) after the second h-BN stamping step and (f) after defining the top gate electrodes.

We start with an SiO_2/Si substrate with pre-patterned alignment marks and local back gate electrodes (Ti(5 nm)/Au(25 nm)/Pd(5 nm)) as shown figure 3.3 (a). We then first stamp exfoliated h-BN flakes on top of the gate with the help of PDMS, and then we use PDMS stamps to selectively place TINRs onto the gate/h-BN stack as shown in figures 3.3 (b) and (c), respectively. Then, we define contacts using EBL lithography followed by evaporation of Ti(5nm)/Au(50-80). The h-BN for the top gate dielectric is placed with the help of another stamping

process, which is followed by patterning of top gate electrodes as shown 3.3 (e) and (f), respectively.

3.1.4 Al-Bi_2Se_3-Al based RF-SQUID coupled to CPW resonator

Design of CPW resonators

Superconducting resonators are one of the key ingredients for circuit quantum electrodynamics. In this thesis, we make use of Coplanar waveguide(CPW) resonators to characterize our RF-SQUIDs based on Al-Bi_2Se_3-Al junctions. In this section, we will go through some of the main considerations in designing CPW resonators used in the thesis. When designing a coplanar waveguide(CPW) resonator, one wants to match the characteristic impedance $Z = \sqrt{L_l/C_l}$ of the waveguide to the measurement setup with impedance $Z_0 = 50\Omega$. Here, L_l and C_l correspond to the inductance and capacitance per unit length of the CPW. Usually, these are obtained by doing full electromagnetic simulations using commercially available software like Sonnect, Microwave Office, etc. But one can get a reasonable estimate of the parameters of the CPW resonator by using the conformal mapping method that involves solving the elliptic integral considering the geometry of the device [125–127]. Here, we make use of this method. Our resonators are fabricated on a sapphire substrate (thickness = 525 μm) with a magneton-sputtered NbN film of thickness 100nm. For calculating the parameters of our waveguide, we assume a London penetration depth of $\lambda_L = 300$ nm for the NbN film. Our CPW resonators have a central conductor width of $s = 10$ μm, and the separation between the central conductor and ground plane is $g = 5$ μm (see figure 3.4(a)). The values of various parameters of the CPW calculated using the conformal mapping method are given in table 3.1.

Substrate	ϵ_{eff}	C_l (F/m)	L_l (μ H)	Rs ($\mu\Omega$/m)	$Z(\Omega)$
Sapphire ($\epsilon_r \simeq 11$)	5.7	157	0.78	10	72

Table 3.1: CPW resonator parameters obtained using conformal mapping. Here, we use NbN film with a thickness of 100 nm and $\lambda_L = 300$ nm. In the table ϵ_{eff} corresponds to the effective dielectric constant, C_l, L_l, and R_s respectively correspond to the capacitance, inductance and resistance per unit length of our CPW, and Z is the characteristic impedance.

As seen in table 3.1, our CPW has a characteristic impedance of 72 Ω, which is larger than the $Z_0 = 50\Omega$. However, we can still extract the resonance parameters of our devices reasonably from the measurements. Our microwave measurement setup can only take 5 mm×5 mm sized chips, and we put two quarter-wavelength resonators ($\lambda/4$), namely RL on the left and RR on the right side of the chip,

coupled to a feedline in the middle of the chip as shown in figure 3.4(b). The two resonators are designed to have a low fundamental frequency such that at least four higher harmonics of the individual resonators occur in our measurement range of 4-8 GHz (see section 3.2.2). The values of coupling capacitances (C_c) between the feedline and the resonators(see figure 3.4(c)) are estimated from the measured resoance of parameters as given by 3.4(see section 3.2.2). From the parameters of our CPW in table 3.1, we can get estimates of the effective parallel lumped components close to the resonance frequency. For the capacitance C_R, inductance L_R and resonance frequency f_r of our $\lambda/4$ resonators of length l we get [127],

$$C_R = C_l \frac{l}{2}, \qquad L_R = L_l \frac{8l}{\pi^2}, \qquad \text{and} \qquad f_r = \sqrt{\frac{1}{2\pi L_R (C_R + C_c)}}. \quad (3.1)$$

Various design parameters of the two resonators RL and RR are given in table 3.2.

Resonator	l (mm)	C_R (pF)	L_R (nH)	l_C (μm)	C_c (fF)	f_r^{design} (MHz)
RL	36	2.80	22.76	200	3.5	627
RR	30	2.34	18.96	300	4	752

Table 3.2: Table indicating the values of various parameters obtained for the two CPW resonators RL and RR.

Design considerations for RF-SQUID

Since we use $\lambda/4$ resonators, the RF-SQUIDs made of our Al-Bi_2Se_3-Al junctions need to be placed at the grounded end of the resonator to couple it inductively to the SQUIDs as shown in figure3.5(a). The coupling between the resonator and the SQUID is given by the mutual inductance (M) between them. We get a rough estimate of the mutual inductance between the centre line and the loop (see 3.4(b)) using the analytic expression [61, 63]

$$M = \frac{\mu_0}{2\pi} l_s \ln \frac{d + w_s}{d} \quad (3.2)$$

where μ_0 is the permeability of free space, l_s and w_s correspond to the length and width of the SQUID loop, respectively, and d is the distance between the central conductor of the CPW resonator and the SQUID loop. It is essential to note that this is not the only parameter we need to optimize in our design. Apart from M, we need to look at the area of SQUID loop A_{loop}, which determines the flux sensitivity of the SQUID loop and the loop inductance L_{loop} of the SQUID which determines the value of the screening parameter β_L^{RF} as well. Ideally, we want to have $\beta_L^{RF} \ll 1$, to guarantee a linear dependence between applied flux and

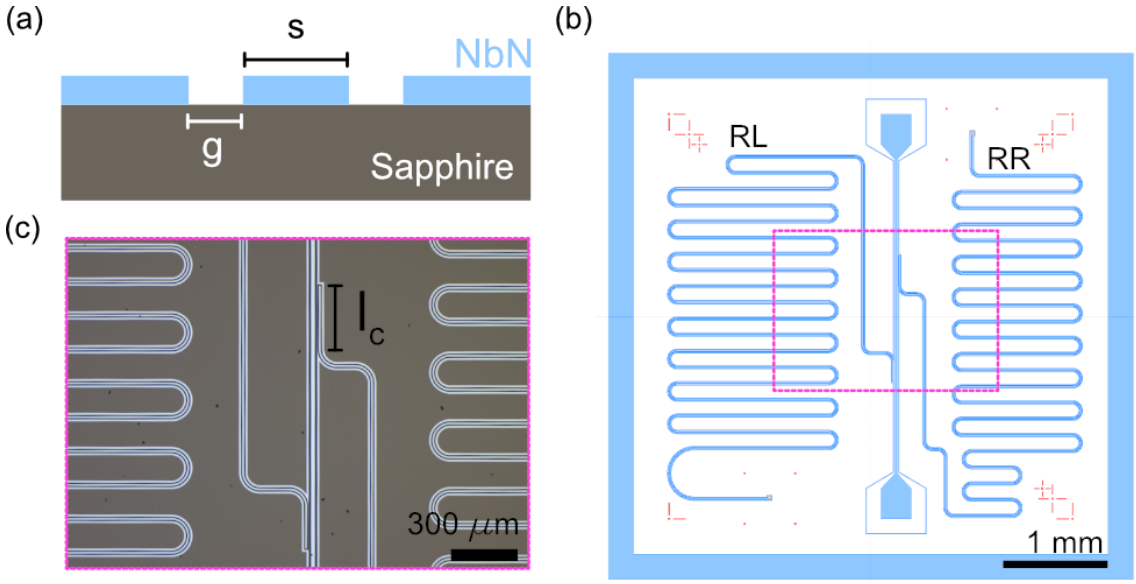

Figure 3.4: (a) Sketch of the cross-section of a CPW resonator showing the width of the central conductor (s) and the gap between the central conductor and ground plane (g). (b) Design of 5 mm×5 mm sized chip containing two $\lambda/4$ resonators RL and RR coupled to a common feedline. (c) Optical image of fabricated CPW resonator chip showing the part where the resonators are coupled to the feedline (marked with a magenta rectangle in panel (b)). Here, l_c marks the coupling length, which determines the values of coupling capacitance C_c.

phase drop across the junction (see section 2.2.5 of Chapter 2). Keeping all this in mind, we designed our RF-SQUID loop to have an area around 100 μm^2, with an arms width of 3μm to reduce L_{loop} and the separation between the SQUID and resonator, d = 500 nm. The fine details for the loop depend a bit on the placement of the TINR forming the SQUID loop. For instance, the optical image of the SQUID device coupled to resonator RL is given in figure 3.4(b). Here, we have l_s = 25 μm, w_s = 13 μm and the total geometric loop area is $\simeq$ 133 μm^2. Using equation 3.2, we get $M \simeq 16$ pH in this case, which serves as a good upper limit. The actual value of M from the measurements will be smaller than this value since the above equation does not take into account the effect of the return currents in the ground plane.

Fabrication procedure

First, a 2-inch sapphire wafer is cleaned and deposited with 100 nm of NbN film with the help of magnetron sputtering. After disposition, the wafers are diced into 5 mm×5 mm sized chips. Then, using EBL, we define an etching mask for the resonator with PMMA resist. The structures are then etched with the help of Ar:Cl_2 reactive ion plasma. After the etching, the chips are examined for

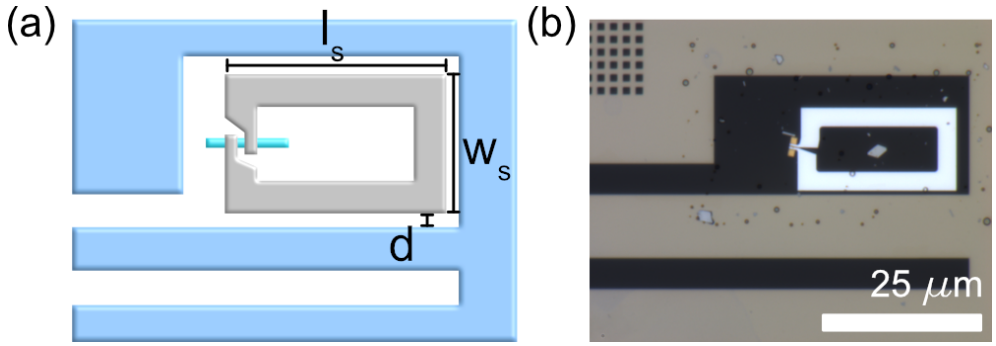

Figure 3.5: (a) Sketch showing an RF-SQUID coupled inductively to the grounded end of a $\lambda/4$ resonator with various dimensions marked. (b) Optical image showing the final S-TI-S based RF SQUID coupled to resonator RL.

quality. Next, we cover the whole chip with PMMA resist for protection during the following step and open a window near the grounded ends of the resonator. We then transfer Bi_2Se_3 nanoribbon through the window opening near the grounded end of the resonators using PDMS stamps as in the case of suspended junctions (see 3.1.2). The ends of the TINRs are clamped to the surface of the substrate with the help of EBL, followed by evaporation of Ti(5 nm)/Au(40 nm). We also perform a cleaning step with hot acetone as described in section 3.1.2. This is followed by an EBL step, which defines the RF-SQUID loop and the S-TI-S junction. We use Pt(4 nm)/Al(100 nm) contacts and follow the same fabrication procedure as described in 3.1.1. The devices are inspected with the help of Optical and atomic force microscopes before measurement.

3.2 Measurement setups

3.2.1 DC measuremnts

All our DC measurements are carried out either in Oxoford Trition closed cycle ^{3}He/^{4}He dilution refrigerator with a base temperature of 20 mK or in a ^{3}He Oxford heliox dipstick with a base temperature of $\approx$ 300 mK. The DC lines of the dilution refrigerator are equipped with RC filters at the 4K stage and copper powder filters at the mixing chamber stage to minimize environmental noise/radiation reaching the device. However, the 300 mK system does not have any high frequency filters. All the IVCs of our devices are measured in current bias mode. The biasing circuit consists of a voltage source and a bias resistor R_{bias} for current biasing and a sampling resistor R_{sam} that is used for probing the current supplied to the device (see figure 3.6). Both the voltage drop across the device and R_{sam} are measured using a setup consisting of two low-noise SRS560 differential amplifiers connected to a DAQ system from National Instruments to get, respectively, the

voltage and current across the device. For small magnetic fields (< 100 mT), we use homemade superconducting coils biased with the help of a low-noise current source.

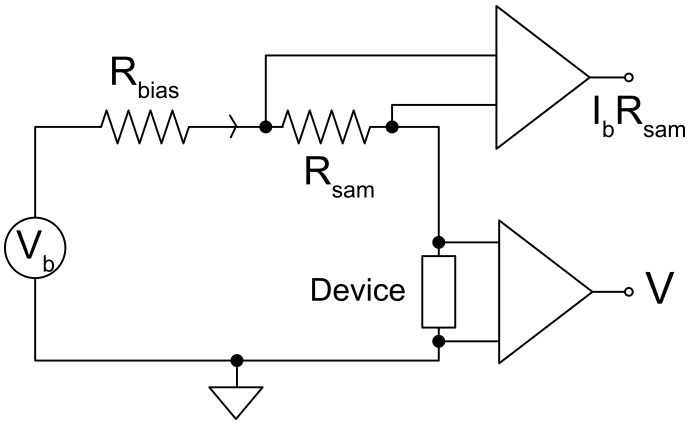

Figure 3.6: DC measurement setup showing the current bias circuit.

3.2.2 Microwave measurements

Measurement setup

All the microwave measurements discussed in the thesis were carried out in ^{3}He/^{4}He dilution refrigerator. The detailed experimental setup used for the measurements is depicted in figure 3.7. The cryostat uses a magnetic field shield (several layers of μ-meatl) around the sample box to protect the device from a magnetic field environment and is indicated with a blue rectangle in figure 3.7. We use a vector network analyzer (VNA) to carry out the resonance measurements on our devices. The RF lines going into the fridge are fitted with attenuators at every temperature stage of the cryostat to minimize thermal and instrument output noise reaching the device. In total, we have signal attenuation of $\simeq -96$ dB (line+attenuators) between the VNA and the device. The return lines from the device pass through a set of circulators, filters and amplifiers before being read back with the second port of the VNA. At the 4K stage, we use a low noise HEMT amplifier in the return line with a bandwidth of 4-8GHz and provides a gain of +30dB. Moreover, we also use a room-temperature amplifier(labelled RA) to boost the signal from the device. The flux biasing of the SQUID is done with the help of a homemade superconducting coil, which is biased with a low-noise current source.

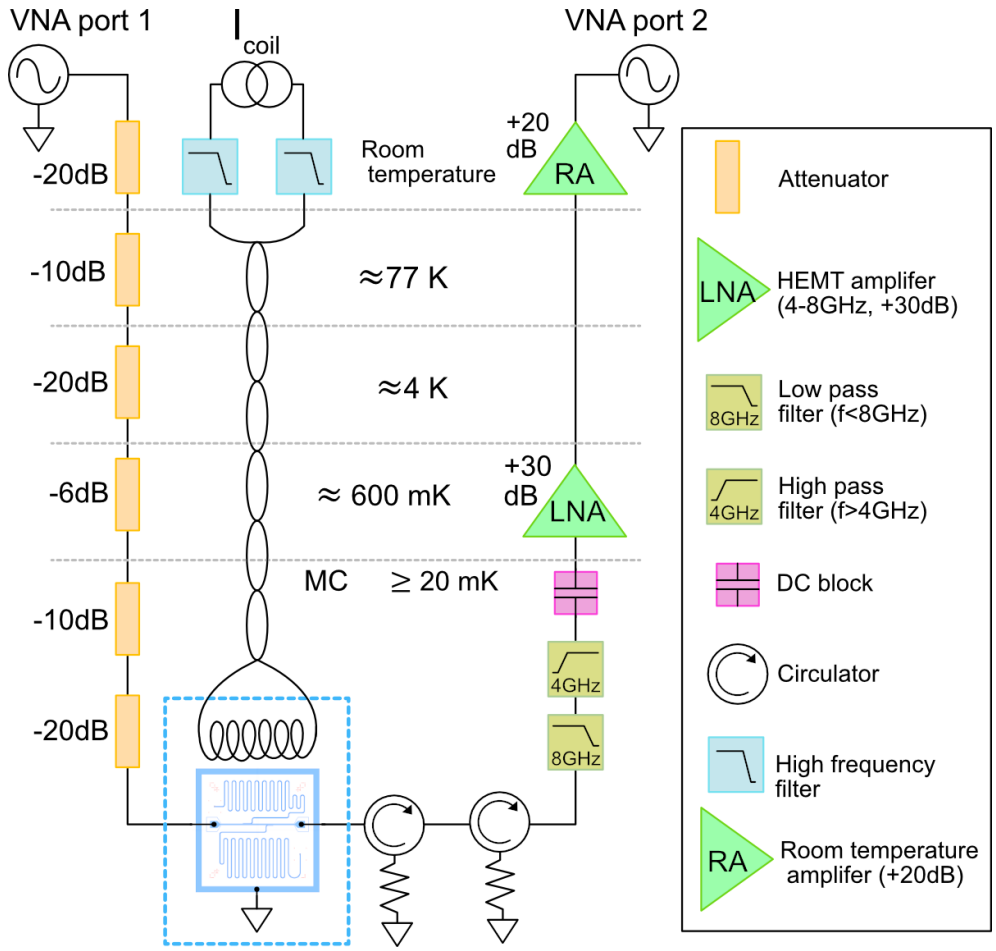

Figure 3.7: Microwave measurement setup probing for reading out the Al-Bi_2Se-Al based RF SQUID devices.

Fitting resonance of the CPW resonators

To get to the various resonance parameters of our devices, we fit the complex scattering coefficient S_{21} obtained from the measurements with the VNA using the following equation [127–129]

$$S_{21}(f) = ae^{i\alpha}e^{-2\pi f\tau}\left[1 - \frac{(Q_l/|Q_{ext}|)e^{i\phi}}{1 + 2iQ_l(f/f_r - 1)}\right]. \tag{3.3}$$

The second part of the equation enclosed in the square bracket represents the response of an ideal resonator with resonance frequency f_r, external quality factor $Q_{ext} = |Q_{ext}|\exp\{(-i\phi)\}$ due to the coupling to the external circuitry (capacitive coupling to the feedline shown in Fig. 3.4 (c)) where ϕ quantifies the impedance mismatch of the resonator and measurement setup (feedline), and loaded quality factor $Q_l = (|1/Q_{ext}| + 1/Q_{int})^{-1}$. Here, Q_{int} describes the internal losses, such as

dielectric, and conductor losses. $|Q_{ext}|$ is determined by the coupling capacitance C_c and can be approximate for small values of C_c as [130]:

$$|Q_{ext}(f)| = \frac{C_R + C_c}{4\pi f Z_0 C_c^2}, \tag{3.4}$$

with Z_0 the impedance of the external circuitry (feedline).

The first part of the expression (outside the square brackets) accounts for other losses or gains in amplitude or phase changes in the measurement setup. Together, they are called the cable delay, and here, a accounts for additional amplitude changes, α accounts for phase shifts, and τ accounts for any electronic delay in the measurement setup. The fitting is done following the circle fit protocol described by Probst et al.[129], with a Matlab script derived from the Python library created by them. In figure 3.8, we show a typical resonance curve from one of our resonators along with the fitted curves. In this case, from the fitting procedure, we get resonance frequency $f_r = 8.1655$ GHz, loaded quality $Q_l = 41363$, external quality $Q_{ext} = 69300$ and internal quality $Q_{int} = 72991$.

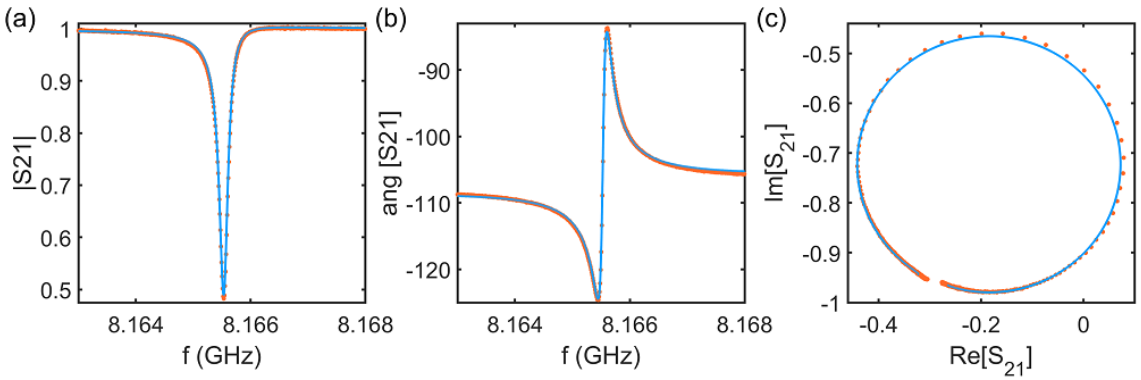

Figure 3.8: Example of resonance data (orange) and along with fits using the protocol by Probst et al. [129]. (a) Magnitude of S21 vs frequency, (b) phase of S21 vs frequency and (c) scattering coefficient plotted in the complex plane showing the typical resonance circle.

4 Transversal quantization and ballistic transport in Al-Bi_2Se_3-Al junctions

A significant obstacle to studies aimed at emulating MBSs using S-TI-S junction is the presence of unintentionally doped bulk states that coexist with TSSs, making the electrical transport analysis cumbersome [8, 36]. As briefly discussed in chapter 2 (see section 2.6), the approach we adopted for reducing the bulk contribution to the electric transport is to increase the surface-to-volume ratio of the 3D TI by growing the material in the shape of nanoribbons or nanobelts [84–86]. However, due to the reduced dimensions of the Bi_2Se_3 NRs-based devices, quantization effects become relevant. In the first section of this chapter, we will demonstrate the width dependence of the current density of our junctions and explain why this is an indication that most of the supercurrent is carried by the top surface [28](Paper I). In the following section, we will provide proof of quasi-ballistic transport over a micrometre scale in Al-Bi_2Se_3-Al by the observation of Fabry-Pérot (FP) resonances in both normal and superconducting states [131] (Paper III). We will also address the discrepancy in the observed FP resonance frequencies in previous studies on Bi_2Se_3 based devices [132, 133] and show, both numerically and experimentally, that transversal, besides coexisting longitudinal, quantization effect provides a more plausible explanation for the observed discrepancy than renormalization of Fermi velocity[132, 133].

4.1 Evidence for size effect from supercurrent current density

Consider an S-TI-S junction with layout A (see Chapter 3 section 3.1) as shown in figure 4.1(a). Here, in the normal region (bare TINR) of the junction, we have TSSs extending over the entire perimeter of the nanoribbon, and supercurrent should be carried by both the top and bottom surfaces of the nanoribbon. For reduced dimensions and assuming zero external magnetic flux, the transverse momentum k_y, perpendicular to the current, is quantized as:

$$k_y = 2\pi(n + 1/2)/P \tag{4.1}$$

where $P = 2w + 2t$ is the perimeter of the nanoribbon with w the width and t the thickness of the nanoribbon,and n is an integer [28, 108]. Here, the factor 1/2 comes from the Berry phase in TIs, and because of this,$k_y = 0$ mode will be absent in these junctions. Now, the modes with $k_y \sim 0$ remain on the top surface while the modes with $k_y \gg 0$ are winding around the perimeter of the TINR. From magnetotransport studies performed on our Bi_2Se_3 nanoribbons [85], we know that at the bottom surface of the TINR, which is in contact with the substrate, there is an accumulation layer of trivial 2DEG and one does not observe the Shubnikov-de Haas oscillations from the bottom TSSs. This is attributed to the lower mobility of bottom surface states. Moreover, our Bi_2Se_3 nanoribbons show significant bulk carrier density. Naturally, the question arises: What carries the supercurrent in our junctions? In the following section, we will look at the Josephson current density of our junctions as a function of the junction width, which, in our case, corresponds to the width of the nanoribbons. Then, we will try and connect it to TSSs [28].

4.1.1 Experimental details

We fabricated Al-Bi_2Se_3-Al junction (layout A) with varying widths from ∼50 nm to about 1 μm. For this, we used substrates of Si/300 nm SiO_2 and $SrTiO_3$ (STO) containing pre-patterned alignment marks and TINRs (see Chapter 3 section 3.1). We used two different growth batches of TINRs, and all devices fabricated on specific substrate types utilized TINRs from the same growth batch. The SEM images of the fabricated Al/Bi_2Se_3/Al junctions for two different nanoribbon widths are shown in figure 4.1(b) and (c).

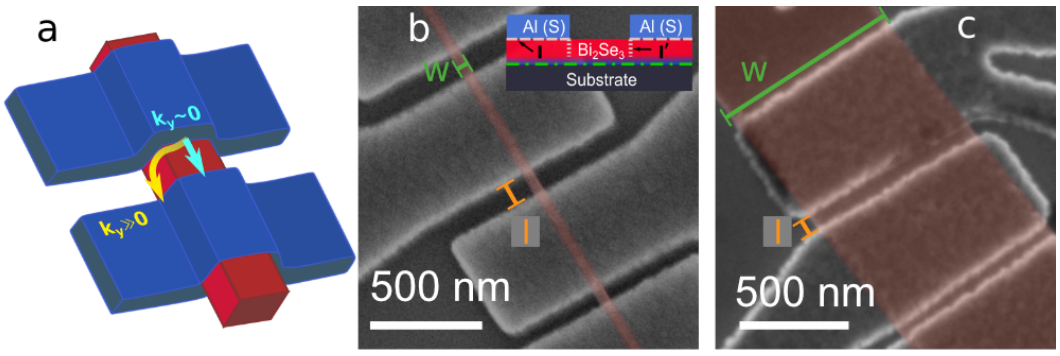

Figure 4.1: (a) Schematic of a Bi_2Se_3 nanoribbon Josephson junction. The arrows indicate transport modes carrying supercurrent by TSSs at the top surface (cyan, $k_y \sim 0$) and around the perimeter (yellow, $k_y \gg 0$) of the nanoribbon. (b) and (c) Partly coloured SEM images of the junctions fabricated on Bi_2Se_3 nanoribbons with different widths w. Here, l indicate the lengths of the junctions. Inset in panel (b) is a schematic cross-section of a junction, dot-dashed green line highlights the location of a trivial 2DEG [85].

A typical IVC of one of the TINR-based Josephson junctions at 19 mK is shown in figure 4.2(a). For the analysis, the critical current I_c is obtained using the forward scan and then converted to critical current density J_c by dividing I_c by the width of the junction w. The device's normal state resistance R_N is determined by considering the linear section of the IVC above $2\Delta'$, which is twice the induced gap of the TI-junction.

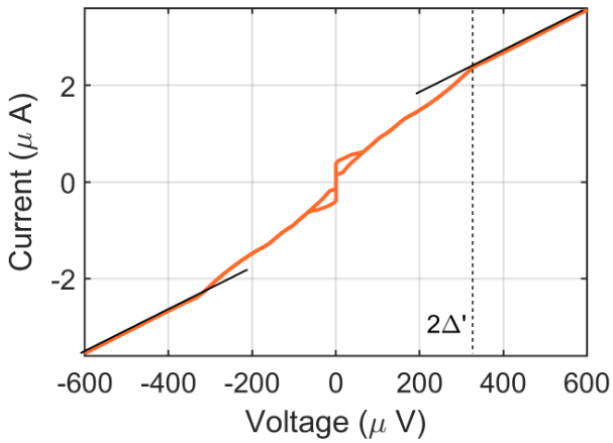

Figure 4.2: Current-voltage characteristic of a Bi_2Se_3 nanoribbon junction ($I_c = 0.36$ μA, $l = 70$ nm, $t = 16$ nm, $w = 430$ nm) measured at $T = 20$ mK, the solid black lines are linear fits of the IVC at high bias voltages. The departure from linearity observed below V = 340 μV corresponds to twice the induced gap, with gap $\Delta' = 170$ μV (see the dashed line).

In figure 4.3(a)and (b), we plot the dependence of the J_c as a function of the w for devices fabricated on Si/SiO_2 and STO substrates, respectively. The blue and orange dots in these plots correspond to junctions with lengths $50 - 80$ nm and $100 - 110$ nm, respectively. Here, for devices of similar length scales, one clearly sees a sharp decrease in J_c with the width w of the TINR at lower-width scales. In figure 4.3(b), we have included a 10 μm wide junction fabricated in layout B (see Chapter 3 section 3.1) for which no winding modes are expected to contribute to the Josephson transport, and J_c seems saturated. We note that the value of J_c changes by a factor of 5-6 when going from the narrowest nanoribbons of 60 nm to the widest ones. In contrast, if we look at the specific resistance of the device, given as $R_N \times (w)$, we get a behaviour almost independent of w for the devices on both the Si/SiO_2 and STO substrates. This allows us to exclude strong modifications/deterioration of the junction-specific resistance (arising from the growth of TINR) as the potential cause for J_c dependence.

What is the origin of this peculiar $J_c(w)$ phenomenology?

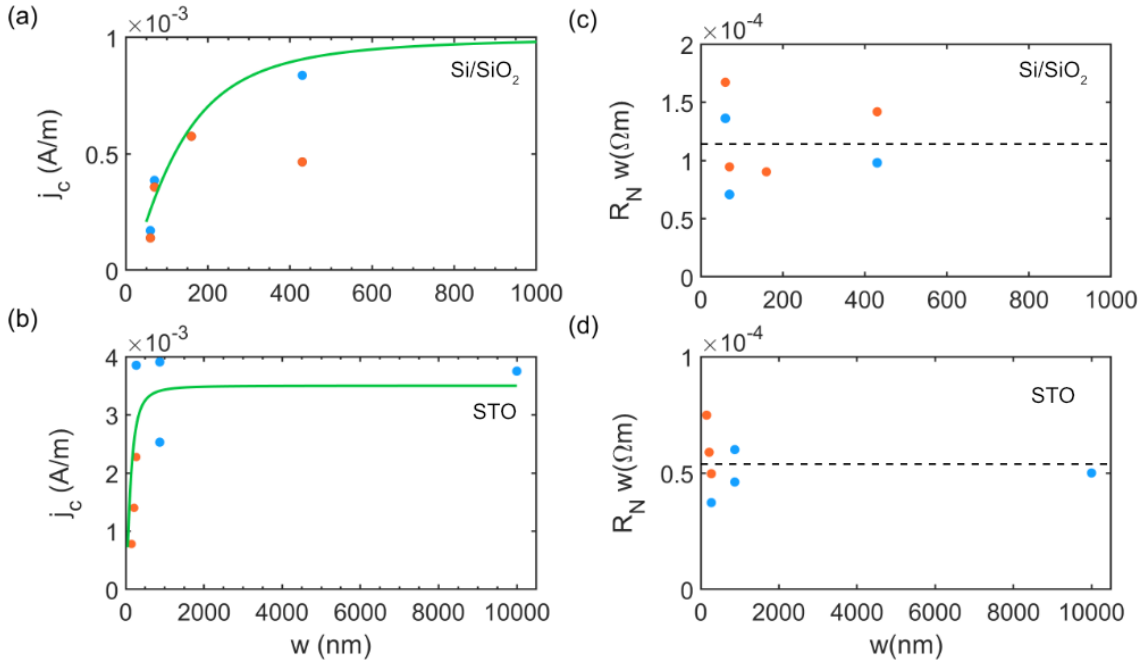

Figure 4.3: (a) Critical current density as a function of TINR width for Josephson junction devices realized from the same growth batch on a Si/SiO_2 substrate. (b) Critical current density as a function of TINR width for Josephson junctions realized from a second growth batch (different from those shown in panel (a)) on a $SrTiO_3$ substrate. All measurements were performed at $T = 20$ mK. The blue and red dots are for junction lengths $50-80$ nm and $100-110$ nm, respectively. (c) Specific resistance as a function of TINR width for Josephson junction devices realized from the same growth batch on a Si/SiO_2 substrate. (d) Specific resistance as a function of TINR width for Josephson junctions realized from a second growth batch (different from those shown in panel (c)) on a $SrTiO_3$ substrate. All measurements were performed at $T = 20$ mK. The blue and red dots are for junction lengths $50-80$ nm and $100-110$ nm, respectively.

4.1.2 J_c (w) and relatives number of modes on top surface

To explain this observed J_c behaviour, we will make use of the transversal quantization of TSSs. From equation 4.1, for a Fermi wave vector k_F of the nanoribbon, we can get the total number of modes n_{tot} as

$$n_{tot} = k_F P/2\pi - 1/2. \tag{4.2}$$

Also, from geometric considerations(see figure 4.4(a) for layout), one can obtain number of modes that are travelling only on the top surface of the junction as [28]

$$n_{top} = k_F PW/4\pi l((w/2l)^2 + 1)^{-1/2} - 1/2. \tag{4.3}$$

Now, for a given junction dimension, we can define the relative number of modes travelling only on the top surface as $n_{rel} = n_{top}/n_{tot}$. Using a typical k_F value

$k_F = 0.55$ nm^{-1} for our TINRs [85], we calculated the width dependence of n_{rel} for three different junction lengths, 50, 75 and 100 nm (see the dashed lines in figure 4.4 (b). For $l = 100$ nm, we obtain a reduction of the relative number of modes travelling only on the top surface by a factor of 5 when reducing the junction width from 900 nm to 50 nm. We also calculated the supercurrent density of junctions considering the angle dependence of the transmission coefficients (as in ref. [21], see Chapter 2 section **??**) of each transport mode travelling only on the top surface. For this, we used equation 2.30, assuming a chemical potential mismatch μ_r of 0.1 between the normal TI weak and superconducting electrodes. As seen in figure 4.4 (b), both J_C (solid lines) and n_{rel} (dashed lines lines) follow qualitatively the same behaviour and qualitatively reproduces the measured J_c *vs* width dependence given in figure 4.3(a) and (b). Here, the solid lines in the measured data represent the calculated relative number of transport modes for $l = 100$ nm. This suggests that, in our devices, only the modes travelling on the top surface contribute to the Josephson current. This is also in agreement with the expected saturation value of J_c for the 10 μm wide device, where the contribution of winding modes to the total Josephson current is negligible.

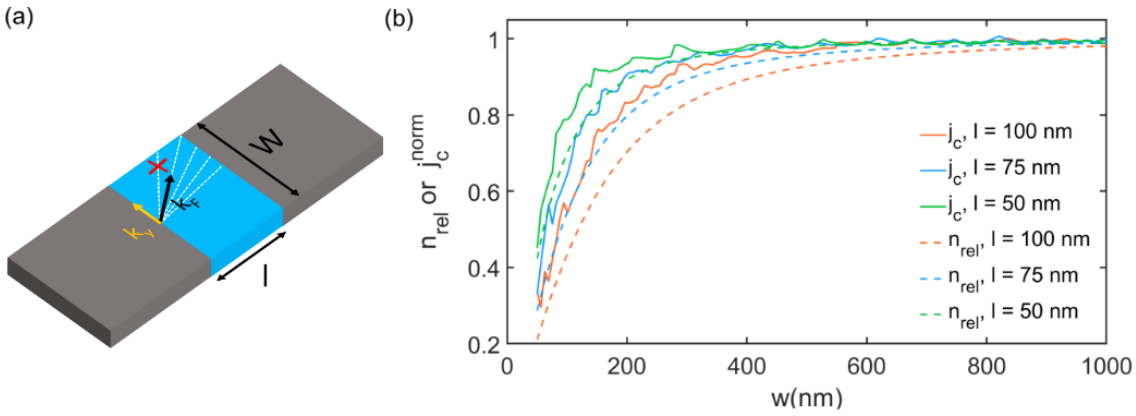

Figure 4.4: (a) Sketch of a planar TI junction with electrodes separation L and width W. The dashed lines indicate quasi-particle trajectories. The maximum transversal momentum for which the transport mode still propagates only on the top surface is indicated by k_y. For larger transversal momentum the quasiparticle trajectory has to wind around the TINR and does not contribute to the critical current (red cross). (b) Relative number of transport modes $n_{rel} = n_{top}/n_{tot}$ propagating only on the top surface (dashed lines) and corresponding normalized critical current density (solid lines) as a function of junction width for three different junction lengths.

A potential reason for this observation might be the reduced mobility of TSSs at the bottom surface of the TINR [85]. Here, the trivial 2D gas at the interface with the substrate overlaps with the Dirac states, and they might fall under a diffusive transport regime. Thus, they might be contributing less to the Josephson transport in our devices. However, this observation does not entirely rule out

contributions of the bulk states to the J_c as they might be present as constant background in the data discussed here. Moreover, in Chapter 5, we will show how to quantify the contribution of diffusive bulk modes to the total Josephson current by analyzing the CPR.

4.2 Fabry-Pérot resonance and ballistic transport

In mesoscopic and nanoscale devices, quasi-ballistic transport of phase-coherent electron waves between two semi-transparent interfaces manifests as Fabry-Pérot (FP) resonance/interference of electronic conductivity. Here, the constructive interference of reflected electron waves between the two interfaces results in resonant transmission whenever $k_F l = \pi n$, with k_F the Fermi wave vector, l the distance between the interfaces, and n a non-zero integer [95]. One can observe FP resonances in the form of periodic oscillations of the conductance of the device as a function of chemical potential [95–97]. Such resonances have been experimentally observed in quasi-1D systems like carbon nanotubes, quantum Hall edge states, semiconducting nanowires, and graphene nanoribbons [95–103]. This phenomenology can also be interpreted as transport through quasi-bound states localized between the two interfaces resulting from finite-size quantization.

In conventional material systems in 2D device geometries, one does not expect to observe interference effects as angle averaging over various electron propagation directions would lead to a vanishing interference pattern [134]. However, the Klein tunneling [104] process intrinsic to Dirac materials, such as in Graphene and TIs, results in a subset of highly transmissive propagation trajectories (modes) at specific angles, allowing the observation of interference effects in two-dimensions [98, 135–137]. Moreover, additional FP resonances can appear due to quantization along the transversal direction [136–139]. Though experimental studies of TI-devices have demonstrated independently demonstrated FP resonances [132, 133, 140], and transversal quantization in TI-devices [141], the 2D aspect of FP resonances in TI-materials is still lacking. Moreover, in studies performed by Finck et al. on Bi_2Se_3 devices [132, 133], there was a discrepancy in the observed periodicity and expected periodicity of FP oscillations from the length scale of the device. These results were interpreted in terms of Fermi velocity renormalization, resulting in an order of magnitude reduction of Fermi velocity reduction. But in the following section, numerically and experimentally, we look at FP resonance in our junctions, and we will provide an alternate explanation for the observed periodicity of FP resonances by considering transversal quantization [131].

4.2.1 Numerical model of FP resonance in TI-devices

Consider an S-TI-S junction of length l in layout A (see Chapter 3 section 3.1) formed out of a nanoribbon width w and thickness t as shown in figure 4.5(a).

We can decompose the momentum k of transport mode into transverse and longitudinal components denoted as k_y and k_n, respectively and define the associated mode trajectory angle $\theta = \tan^{-1}(\frac{k_n}{k_y})$. Now, as discussed in section 4.1, we assume that the transverse momenta in the TI-junction are quantized, forming subbands as $k_y = 2\pi(n+1/2)/P$ (see equation 4.1). For simplicity, we will consider the case where $w \gg t$ such that $k_y \simeq (n+1/2)\pi/w$. Now, for a given chemical potential μ and Fermi velocity v_F, the transmission probabilities of the different transport modes arising from the TSSs (in extreme Fermi-level mismatch limit) are given by

$$\tau_n(\mu) = \frac{k_n^2}{k_n^2 \cos^2(k_n l) + (\mu/\hbar v_F)^2 \sin^2(k_n l)}, \tag{4.4}$$

with $k_n = [(\mu/\hbar v_F)^2 - k_y^2]^{1/2}$ [105]. Using the Landauer formula, we can compute the normal state (zero-bias) conductance of the device as $G(\mu) = G_0 \sum_n \tau_n(\mu)$, where $G_0 = e^2/h$, h the Planck constant, and e the elementary charge.

The calculated zero bias conductance of a TI-junction as a function of μ for a junction length $l = 100$ nm and typical Fermi velocity $v_F = 5 \times 10^5$ m/s [84] for varying widths w ignoring the thickness given in figure4.5(b). Here, linear backgrounds have been removed from every curve for clarity (denoted as G_{bgr}). For wide devices, at low chemical potentials (near the Dirac point at $\mu = 0$), there are conductance oscillations with a period given by $\Delta\mu^L = \hbar v_F \Delta k_F = h v_F/2l$, with $\Delta k_F = \pi/l$ due to finite size quantization along the length of the junction. Away from the Dirac point, with high values of μ, faster oscillations characterized by a period $\Delta\mu^W \simeq h v_F/2w$, originating from the finite-size quantization along the perimeter of the nanobelt ($\sim 2w$) become prominent. However, when junction widths approach the length of the junction, the superposition of conductance oscillations with similar periods ($\Delta\mu^W \simeq \Delta\mu^L$) makes it challenging to identify periodic oscillations. To resolve this, we use Fast Fourier transform(FFT). As seen in figure4.5(c), the FFT shows a width-independent peak at low frequencies given by $f_\mu^L = 1/\Delta\mu^L = 2l/h v_F$ and at higher frequencies, we have a peak dispersing linearly with the width, $f_\mu^W = 1/\Delta\mu^W = 2w/h v_F$. Moreover, we also observe higher harmonics of the width scale appearing approximately at frequencies given by $m \cdot f_\mu^W$, with m an integer larger than 1.

At finite source-drain bias voltage V_b, the current through the device can be calculated using the Landauer formula $I = (2e/h) \int_{\mu_1}^{\mu_2} T(\epsilon - \epsilon_D) d\epsilon$, where μ_1 and μ_2 are the chemical potentials of the left and right contact, respectively, and $T(\epsilon - \epsilon_D)$ is the transmission probability as a function of energy (distance from Dirac point ϵ_D) [139]. The numerically calculated differential conductance of a device with $l = 100$ nm and $w = 1.5$ μm, assuming transmission probability in equation 4.4 and symmetric contacts ($\Delta\epsilon_D = eV_b/2$ with $V_b = (\mu_l - \mu_r)/e$), is given in figure 4.5(d). On a large energy range, we have the typical FP diamonds with characteristic period $\Delta\mu^L = h v_F/2l \simeq 10.3\ meV$ (see the upper

panel) associated with the length of the device. The corresponding periodicity along the source-drain voltage direction is given by $\Delta V_b^L = 2\Delta\mu^L/e$.

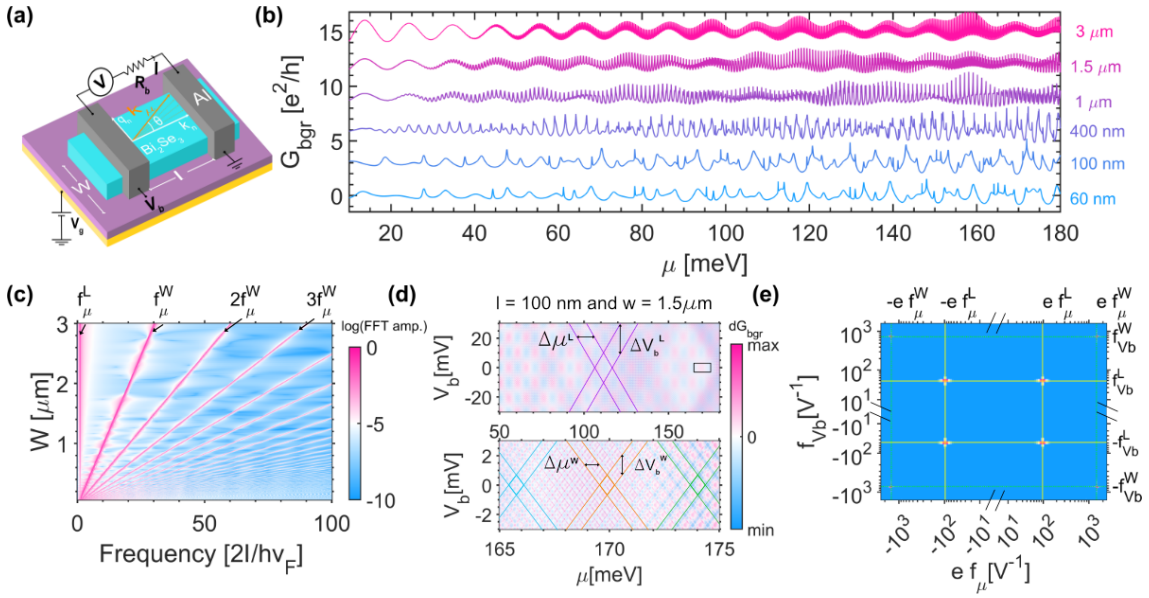

Figure 4.5: (a) Sketch of the device geometry. (b) Numerically calculated conductance (G_{bgr}) as a function of chemical potentialμ for a device with length $l = 100$ nm and widths ranging from 60 nm to 3 μm. (c) FFT of G_{bgr} vs. μ traces for various device widths. (d) FP oscillations of the conductance as a function of chemical potential and source-drain bias (upper panel) calculated for a device of dimension l = 100 nm and w = 1.5 μm. The four purple lines indicate an FP diamond arising from the resonance condition along the length of the junction. Here, the distance between the parallel lines along the chemical potential direction is given by $\Delta\mu^L$, whereas the distance along the bias voltage direction is given by $e\Delta V_b^L = 2\Delta\mu^L$. The lower panel is a zoom-in of the region indicated by the black rectangle in the upper panel. FP diamonds, due to transversal quantization, given by periodicities $\Delta\mu^W$ and $e\Delta V_b^W = 2\Delta\mu^W$ are indicated in three different chemical potential regions. There are additional features inside these diamonds, and the visibility depends on the region of μ under consideration. (e) The two-dimensional Fourier transform of the FP oscillation shown in the upper panel in (d). The solid yellow and dashed green lines indicate the locations of the characteristic frequencies f_μ^L and f_μ^W, respectively.

On smaller energy scales (see lower panel in figure 4.5(d)), we observe oscillations related to $\Delta\mu^W \simeq hv_F/2w \simeq 0.69\ meV$ and higher harmonics given by $\Delta\mu^W/m$. The corresponding period along the source-drain voltage direction is given by $\Delta V_b^W = 2\Delta\mu^W/e$. Like before, we make use of 2D-FFT of the full conductance map given in figure 4.5(e) to identify the two main frequencies f_μ^L and f_μ^W along the f_μ axis [139]. Along the f_{V_b} axis, these peaks appear at frequencies $f_{V_b}^L = ef_{\mu,L}/2$ and $f_{V_b}^W = ef_\mu^W/2$.

4.2.2 Experimental observations

FP resonance in the normal state of Al-Bi_2Se_3-Al Junctions

Figure 4.6(a) shows the experimental setup used for electrical characterization along with the SEM image of two junctions, C1 and C2, fabricated on the same Bi_2Se_3 nanoribbon of width $w \simeq 430$ nm and thickness $t \simeq 16$ nm. Here, we will discuss the data from device C1 with $l = 100$ nm, and data from the adjacent 70 nm long device(C2) can be found in [131]. We use backgates defined on the backside of the SiO/Si substrates for the gate-dependent measurement provided here. First, we are interested in the normal state transport of the device, and we apply an out-of-plane magnetic field of 30 mT to quench superconductivity in the Al electrodes. To get the differential conductance matrix of the device as a function of bias voltage, V_b, and gate voltage, V_g, we take the current-voltage characteristic (IVC) at every gate voltage and numerically differentiate the curves ($G = dI/dV_b$). Moreover, we remove a smooth background along the source-drain voltage and gate voltage directions to visualize the data better, and the resulting differential conductance (G_{bgr} at 20 mK) map of device C1 in the normal state is shown in figure 4.6(b).

We take the derivative of the conductance with respect to gate voltage dG_{bgr}/dV_g of the conductance map (figure 4.6(c)) to identify the diagonal features (indicated by lines) in the conductance map better [139]. We then apply a 2D-FFT to determine the period of these oscillations. In the 2D-FFT provided in figure 4.6(d), we observe two clear peaks at frequencies $\simeq \pm$ 216 V^{-1} along the f_{V_b} direction and $\simeq \pm$ 0.085 V^{-1} along the f_{V_g} direction, respectively, (see crossing point of horizontal and vertical dashed magenta lines) resulting from lines with a negative slope that form the diamond pattern of the FP oscillations shown in figure 4.6(c). The peaks corresponding to the positive sloped lines of FP resonance are less clear than their counterparts. The obtained frequency in source-drain bias is close to the expected value $f^W_{V_b} = 208\ V^{-1}$, related to transversal quantization. From the observed peak position of $f^W_{V_b} = 216$ V^{-1} we get a subband spacing of $\Delta\mu^W = e/2f^W_{V_b} = 2.3$ meV. To highlight the peak features in the 2D-FFT data further, we integrate the 2D-FFT plot along the f_{V_g} axis and thus obtain reduced FFT shown in figure 4.6(e). Here, close to the location of the expected frequency $f^W_{V_b} \simeq 208$ V^{-1}, we observe a clear peak, whereas the higher harmonics ($m \times f^W_{V_b}$) are not visible. In figure 4.6(f), we plot the reduced FFT obtained by integrating the 2D-FFT along the f_{V_b} axis. We see clear peaks at $f_{V_g} \approx \pm 0.085\ V^{-1}$.

We can now use the relation $ef^W_\mu = 2f^W_{V_b}$ to translate a gate voltage change δV_g into a chemical potential change $\delta\mu = \alpha e \delta V_g$ by assuming a linear change of μ with V_g. From the observed peaks $f^W_{V_g}$ and $f^W_{V_b}$ we obtain $\alpha = f^W_{V_g}/2f^W_{V_b} \simeq 2.0 \times 10^{-4}$. Note that for the full range of applied gate voltages (-20 to 20 V), μ changes by roughly 8 meV and since the chemical potential of Bi_2Se_3 nanoribbons is at least 160 meV above Dirac point [84, 85], it is reasonable to linearize the typical

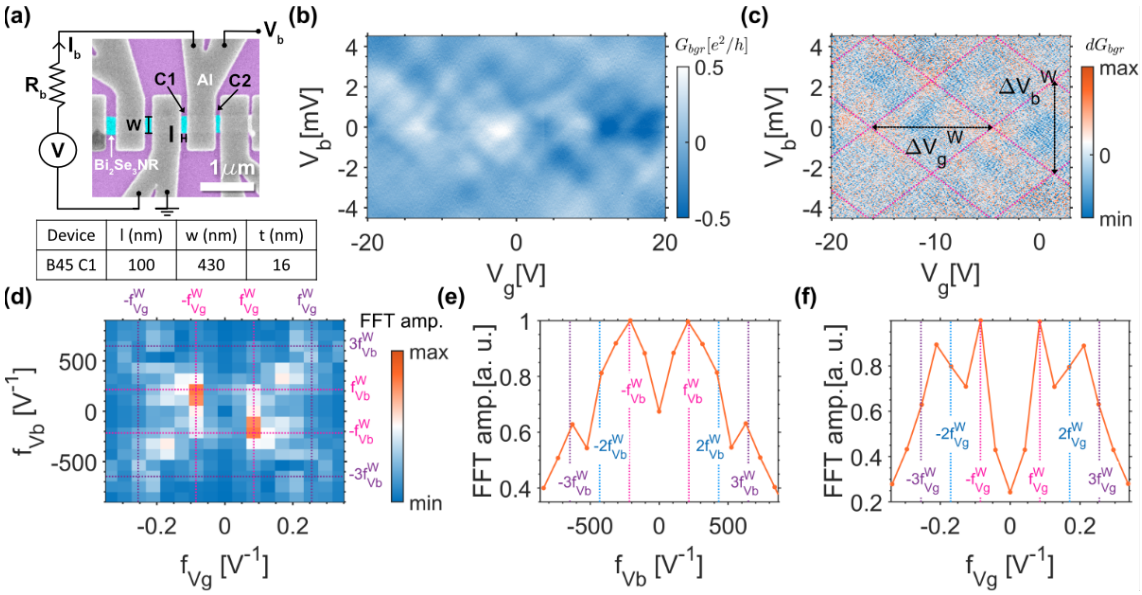

Device	l (nm)	w (nm)	t (nm)
B45 C1	100	430	16

Expected FP period (meV)		Expected frequency (V^{-1})		Measured peak position (V^{-1})		$\alpha = f^W_{V_g}/2f^W_{V_b}$
$\Delta\mu^L$	$\Delta\mu^W$	$f^L_{V_b}$	$f^W_{V_b}$	$f^W_{V_b}$	$f^W_{V_g}$	
10.34	2.40	48.36	207.95	216	0.085	2.0×10^{-4}

Figure 4.6: (a) SEM image of the devices (C1 and C2) along with the measurement layout. The dimensions of device C1 are given in the table below. (b) Differential conductance map of the device in terms of bias voltage V_b and back gate voltage V_g after background subtraction showing FP resonances. (c) Colour map showing the derivative of the conductance with respect to gate voltage dG_{bgr}/dV_g of the conductance map shown in panel (b). Here, it is a bit clearer to see the straight lines in conductance that form the chessboard-like pattern. The dashed lines indicate the expected location of the conductance lines of FP resonance originating from quantization along the width. (d) 2D-FFT of the colour map in panel (c) shows two clear peaks (orange) that match the locations of expected frequencies, due to transversal quantization along the perimeter of the nanoribbon, plotted as magenta dashed lines. (e) Reduced FFT as a function of f_{V_b} obtained by integrating the 2D-FFT in panel (b) along the f_{V_g} direction. Clear peaks appear at $f_{V_b} = \pm 218 V^{-1}$. (f) Reduced FFT as a function of f_{V_g} obtained by integrating the 2D-FFT in panel (b) along the f_{V_b} direction. Clear peaks appear at $f_{V_g} = \pm 0.085 V^{-1}$. The table below summarizes all the expected frequencies and measured peak positions in the FFT plots.

$\mu \propto \sqrt{V_g}$ dependence for Dirac materials, that is, assume a linear change of the chemical potential with gate voltage $\delta\mu = \alpha e \delta V_g$. Moreover, since in our measurement, the ranges in both bias and gate voltage axis are less than the energy scale $\Delta\mu^L = 10.3$ meV, we do not observe the periodicity associated with the length of our device in our measurements.

FP resonance in the superconducting state

As seen in section 4.1 of this chapter, we have indications of supercurrents in our junction being carried by bound states arising from TSSs. Here, we provide further proof of this by looking at the effect of FP interference on the superconducting transport properties of our device. The IVC of device C1 measured at temperature $T = 20$ mK and zero applied magnetic field and the gate voltage is shown in figure 4.7(a). We can extract the critical current I_c, the normal state resistance R_n, and the excess current I_{ex},a feature in our junctions due to the Andreev reflection feature (see 2.3.1), from the IVC. In figure 4.7(b-d), we plot the variations of I_{ex}, I_c, and R_n over a gate voltage of -25 to 25V ($\Delta\mu \simeq$10 meV), respectively. Here, we see clear oscillations of all three parameters with respect to V_g.

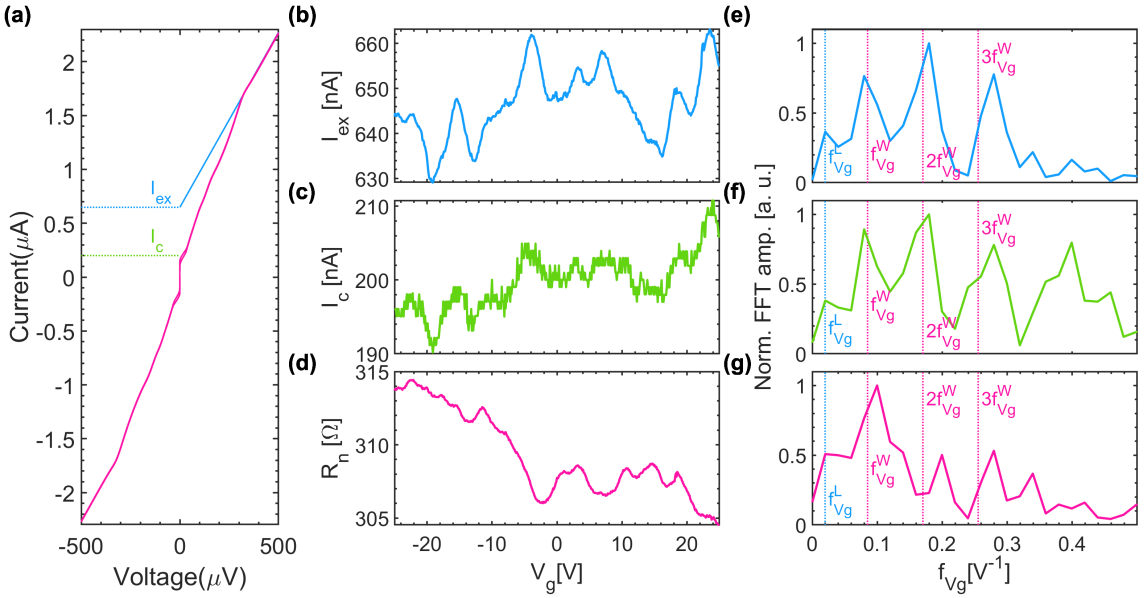

Figure 4.7: (a) IVC of device C1 measured at $T = 20$ mK. The critical current I_c and excess current I_{ex} are indicated by the horizontal lines. Excess current (b), critical current (c), and normal resistance (d) as a function of applied gate voltage. (e-g) FFT of traces from panels (b-d). The expected frequencies $f^L_{V_g}$ from quantization along the length of the device and $f^W_{V_g}$ and two higher harmonics from the quantization around the perimeter of the nanobelt are shown by dashed blue and magenta lines, respectively. For all three quantities, we see clear peaks in the FFT at locations $f^W_{V_g}$. In the case of I_c and I_{ex}, when the junction is in the superconducting state, we can identify clear peaks at $2f^W_{V_g}$ and $3f^W_{V_g}$.

To obtain the periodicity of these quantities, we take the FFT of these curves shown in figure 4.7(e-g). In all three FFTs, we observe multiple peaks. The expected locations of $f^L_{V_g} = e\alpha f^L_\mu$ (blue dashed line) and $f^W_{V_g} = e\alpha f^W_\mu$ (with α extracted from the analysis in the normal states) and the two higher harmonics of it (magenta dashed lines) are plotted in the same panels. One can see that for all

three cases, we observe clear peaks at frequencies $f_{V_g}^W$. For I_c and I_{ex}, there are also clear higher harmonic peaks around $2f_{V_g}^W$ and $3f_{Vg}^W$. Whereas for R_n, the higher harmonic peaks are not well visible. This might be related to the fact that for the extraction of R_n we average over a finite source drain voltage range. From this, we can say that the superconducting transport properties of an S-TI-S junction also inherit the periodicity of FP resonance in the normal state. The observation of harmonics of the transversal quantization frequency in the superconducting state of the junction indicates that the ballistic TSSs carry a substantial part of the Josephson supercurrent [28, 142]. Furthermore, we observe a tiny kink around $f_{V_g}^L$ in all three FFT curves. However, since the gate voltage range $\Delta V_g = 50V$, corresponding to a chemical potential change of $\Delta\mu = e\alpha\Delta\mu \simeq 10$ meV, barely covers one period of $\Delta\mu^L \simeq 10.3$ meV, we refrain from taking it as a confirmation of FP oscillations related to quantization along the length of the device. Similar behaviour was observed for device C2 with $l = 70$ nm in both the normal and superconducting states [131].

FP resonance in a micrometre scale TI-junction

We studied quantum interference effects in an even wider device C4(see layout given figure 4.8(a)) with width w =1.5 μm and length l=160 nm to provide further proof of the ballistic nature of the TSSs. Since device C4 has layout B (see Chapter 3 section 3.1), we do not expect any transport modes that go around the perimeter of the nanoribbon, and the width of the device should define quantization along the transversal direction. The conductance map measured at 20 mK (zero magnetic fields), after removing the linear background, as a function of the source-drain voltage and the gate voltage is shown in figure 4.8(b). Here, one can immediately see that the measured data are slightly more complex to analyze than in the previous case due to subgap features emerging from multiple Andreev reflections in the junction. Nevertheless, by taking the derivative along the gate voltage direction of the measured differential conductance matrix, we observe the typical diamond pattern of FP resonances (see figure 4.8(c)). On close examination, one can see that the FP diamonds are not symmetric compared to the previous device (see slanted diamond features indicated by dashed lines). This can be attributed to the asymmetry in contact resistance [139] and might originate from asymmetry in contact areas due to slight miss-alignment in the lithographic step for defining contacts. We picked one of the dominant diagonal features and added dashed lines with the expected periodicity of FP resonance attributed to the width scale of the device, including the effect of asymmetric contact resistance (see below for more details). One can see that even faster modulating features occur between those lines coming from higher harmonics of the width scale.

The 2D FFT of the conductance map given figure 4.8(c) is shown in figure 4.8(d). The asymmetry in the contacts of the device manifests as an asymme-

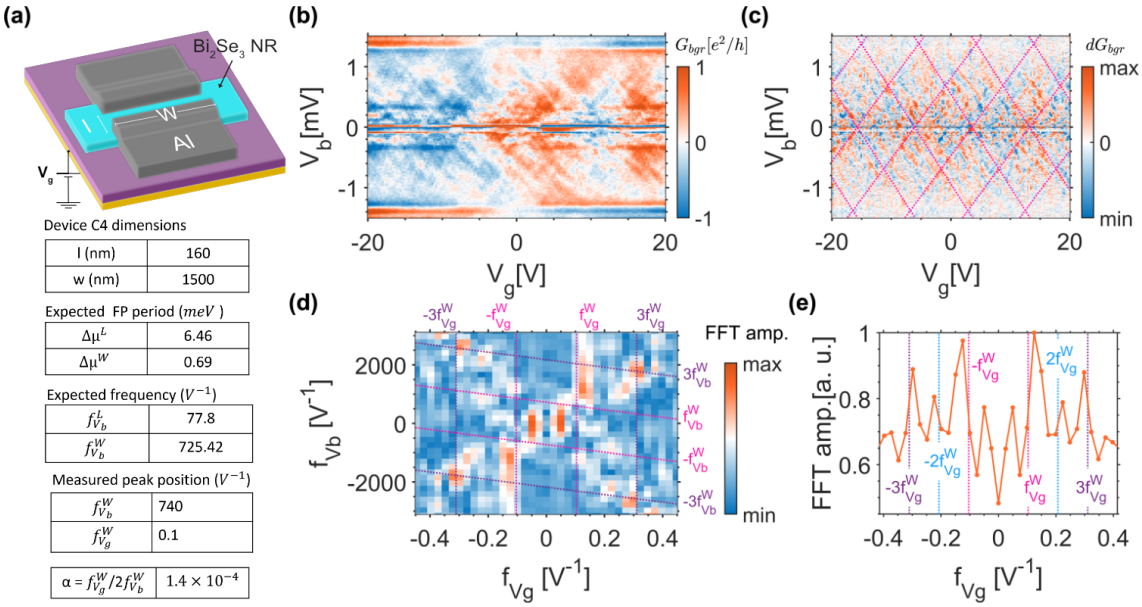

Figure 4.8: (a) Sketch of the device C4 along with the dimensions given in the table below. (b) Differential conductance map of the device as a function of V_b and V_g after background subtraction showing FP resonances. (c) Colour map of dG_{bgr}/dV_g of the conductance map shown in panel (b) along with dashed lines to indicate the expected diamond pattern of FP resonance resulting from finite size quantization along the transversal direction of the device. (d) 2D-FFT of the colour map shown in panel (c), along with the expected frequencies and their third harmonics plotted as dashed magenta and green lines. Here we see peaks corresponding to $3f^W_{V_b}$ around $2000V^{-1}$ (f) Reduced FFT as a function of f_{V_g} showing peaks around $f^W_{V_g} \simeq \pm 0.11V^{-1}$ (magenta vertical dashed line) and $3f^W_{V_g} \simeq \pm 0.32V^{-1}$ (violet vertical dashed line).

try in the location of the peaks along the source-drain voltage bias direction (see the slanted dotted lines). We consider the distance between the peaks along f_{V_b} for positive and negative frequencies to eliminate the effect of asymmetric contacts. From the four distinguishable dominant peaks in the 2D FFT plot, we extract a frequency of $\simeq 2230\ V^{-1}$ along the f_{V_b} direction, which is close to the expected frequency value $3f^W_{V_b} = 2176V^{-1}$, corresponding to the third harmonic of $f^W_{V_b}$. Along the f_{V_g} axis, this peak is located at $\simeq 0.31V^{-1}$. Like before, we can transform the gate voltage change from those two peak positions into a chemical potential change $\delta\mu = \alpha e \delta V_g$, with $\alpha \simeq 1.4 \times 10^{-4}$. Since the peaks are rather broad along the f_{V_b} axis, we take the reduced FFT of the 2D-FFT by integrating over the f_{V_b} axis, shown in figure 4.7(e). Here we observe six peaks located close to the expected values $f^W_{V_g} \simeq \pm 0.10V^{-1}$, $2f^W_{V_g} \simeq \pm 0.21V^{-1}$, and $3f^W_{V_g} \simeq \pm 0.31V^{-1}$. This observation of FP resonance due to transversal (width) quantization in device C4 points towards quasi-ballistic transport over a few micrometres via the TSSs in our Bi_2Se_3 nanoribbons. This length scale is an order of magnitude larger than

the typical phase coherence length reported for Bi_2Se_3 from quantum interference effects, such as weak anti-localization, in magneto-transport measurements [86]. A possible reason for this observation could be that weak anti-localization corrections in the conductance are mainly determined by diffusive trajectories and, therefore, less sensitive to ballistic transport modes.

5 Current-phase relation of Al-Bi_2Se_3-Al junctions

The CPR of a Josephson junction is one of the most crucial characteristics related to the symmetry of the order parameter and nature of transport across the junction [143]. One can gain insights into various aspects of a junction by studying the CPR. Conventional superconducting tunnel junctions, proposed by Brian Josephson in 1962 [46], have a sinusoidal CPR. Deviations from the conventional Josephson effect result in a non-sinusoidal CPR [47, 143]. As discussed in Chapter 4, most of the current in an S-TI-S junction must be carried by highly transparent ABSs arising from TSSs, and this should manifest as a slanted CPR. Here, we utilize a simple asymmetric SQUID measurement technique to extract the CPR of our Al-Bi_2Se_3-Al junctions and provide estimates of the current carried by ABS fromTSSs by fitting the obtained CPR to a model taking into account the contribution of ballistic TSSs and diffusive bulk states. We also discuss the evolution of the CPR with temperature and the effect of inductance in the CPR extraction process.

5.1 CPR extraction with asymmetric SQUID technique

The CPR of a superconducting junction can be probed using various DC and RF measurement techniques. Out of these, one of the simplest and most commonly used techniques for extracting the CPR of a junction is the current biased asymmetric DC-SQUIDs measurement [26, 27, 144–146]. For this, the test junction with unknown CPR of the form $I_t = I_{t,c} \cdot f(\varphi_t)$ connected in parallel to a reference junction having known CPR $I_r = I_{r,c} \cdot g(\varphi_r)$ forming a dc-SQUID loop. Here, $I_{t,c}$ ($I_{r,c}$) and φ_t (φ_r) correspond to the critical current and phases across the test (reference) junction, respectively. Typical critical current asymmetries required for the extraction of the CPR are in the range of 15-20[142, 144]. Figure 5.1(a) shows the sketch of an asymmetric SQUID device. For a total SQUID loop inductance L and applied magnetic flux Φ_{ext}, the phase across the test junction is given by

$$\varphi_t = \varphi_r + \frac{2\pi\Phi}{\Phi_0}, \tag{5.1}$$

with $\Phi = \Phi_{ext} - L\left[I_r(\varphi_r) - I_t(\varphi_t)\right]/2$ the total magnetic flux through the SQUID loop (assuming the L is distributed equally among the two arms of the SQUID) and Φ_0 the superconductive flux quantum [147]. Equation 5.1 is a transcendental equation and requires numerical methods to solve. But, if L is small enough such that the screening parameter $\beta_L = (I_{r,c} + I_{t,c})\, L/\Phi_0 \ll 1$, we can drop the terms including inductance from equation 5.1 and it reduces to $\varphi_t \simeq \varphi_r + 2\pi\Phi_{ext}/\Phi_0$. Due to the large asymmetry of the critical currents, upon application of Φ_{ext}, the maximum critical current of the SQUID is obtained for $I_r = I_{r,c}$ at $\varphi_{r,max}$, where the current through the reference junction is maximized, while the phase across the test junction, φ_t, varies approximately linearly with Φ_{ext} as [144]

$$\varphi_t \simeq \varphi_{r,max} + \frac{2\pi\Phi_{ext}}{\Phi_0}. \tag{5.2}$$

Thus, the CPR of the test junction can be determined by subtracting the constant contribution of the reference junction, $I_{r,c}$, assuming a point-like junction, from the total critical current of the SQUID and converting Φ_{ext} to φ_t using the above equation.

5.1.1 Experimental consideration

Due to the well-studied sinusoidal CPR of tunnel junctions, the original technique of asymmetric SQUID measurement was developed based on them as a reference junction [144]. This is the most preferred form of reference junctions, and in this case, one gets $\varphi_{r,max} = \pi/2$. Over the years, other forms of reference junctions have been implemented in asymmetric SQUID setups. One of the common options are superconducting nanowire weak links or bridges as reference junctions [26, 27, 109, 148, 149]. However, it was shown recently that in some cases, using such junctions as a reference may result in false CPR [149] as the CPR of the nanowire weak link can be multivalued [150, 151]. Moreover, with the experimental requirements and considering the tools we had, fabricating an asymmetric SQUID device with any of these kinds of reference junctions, nanowire weak links or tunnel junctions, calls for multiple lithography steps. However, nano-processing steps, especially the ones involving heating or etching, tend to alter the properties of TI materials. Therefore, we used larger TI junctions as the reference junctions in our measurements [142]. This only required a single lithography step, thus reducing damages to the TI-junctions during device fabrication. In this case, even though the CPR of the reference junction is not known a priori, as long as $I_{r,c} \gg I_{t,c}$, one can still extract the CPR of the test junction. However, in this case $\varphi_{r,max}$ is not $\pi/2$. Earlier experiments have shown that this approach is reliable for extracting the CPR of the test junction [145, 146, 152].

To fabricate asymmetric SQUIDs, we used Bi_2Se_3 nanobelts, which are at least 7-8 μm long, to be able to fabricate both the test and reference junction on the

same nanobelt [22, 31]. We consider both junctions of layout A and layout B as test junctions (see Chapter 3 section 3.1 for more on layouts). However, the main device discussed in this chapter has a test junction with layout A, as this layout is geometrically well-defined compared to layout B. However, we have included extracted CPR from the junction with layout B in the addition data section of this chapter (see 5.4). Since the critical current of the reference junction needs to be 15-20 times larger than the test junction, we only used layout B junctions with typical lengths of 80-100 nm and widths of 5-6 μm for this. At these dimensions, our reference junctions are not point-like, and we expect to see the Fraunhofer patterns with the primary lobe spanning a magnetic field range of roughly 200 μT. This was estimated using the expression for the effective area of a planar junction in the thin film limit given by $A_{eff} = wl + w^2/1.8$ (even though this expression is only valid for $w < \lambda^2/t$, it still provides a reasonable estimate for A_eff) [51, 106]. So, we will have to consider a SQUID loop size such that the modulation period of the SQUID will be much lower than the width of the central lobe of the Fraunhofer pattern from the reference junction. Moreover, for all devices, the width of the SQUID loop is kept at 3 μm in most sections of the loop to minimize kinetic inductance contributions and thus have $\beta_L < 1$.

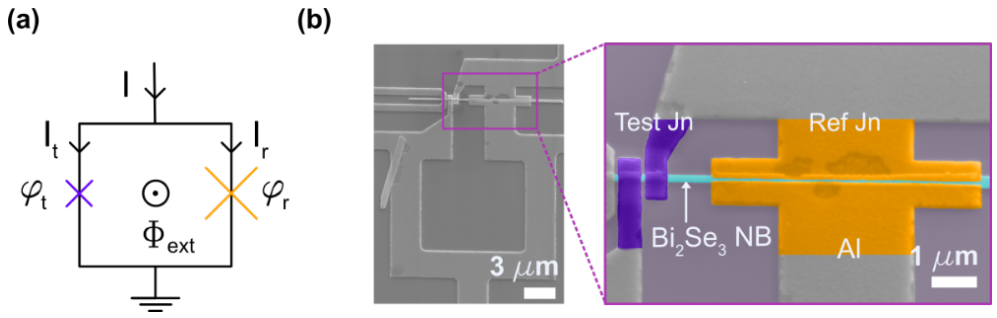

Figure 5.1: (a) Sketch of the SQUID containing both the test (purple) and reference (orange) junction. (b) SEM image of the TI-SQUID device S1 (left panel). The right panel is a false-coloured SEM image showing the test (purple) and reference(orange) junctions formed out of a Bi_2Se_3 nanobelt(cyan).

The SEM images of the asymmetric SQUID device (S1) discussed here are shown in figure 5.1.(b). From a close-up in-lens SEM image (not shown) of the test junction, we found that the width of the nanobelt, and thus the width of the test junction, $w \simeq$188 nm, and the length of the test junction $l \simeq$83 nm. The corresponding length and width of the reference junction are $\simeq$ 80 nm and $\simeq$ 5 μm, respectively. Using AFM imaging, we got the thickness of the nanobelt that forms the junctions to be $t \simeq$ 48nm. From the layout of the SQUID loop, by numerically solving the London-Maxwell equations, we determined the effective area $A_{eff} \simeq$ 200 μm^2. This should result in a modulation period of approximately 10 μT. From the same numerical calculations, we also extract a SQUID loop inductance

value $L \simeq 29$ pH, of which ~ 27 pH correspond to the geometric inductance, and the remaining ~ 2 pH are the kinetic contribution to loop inductance [153]. Here, we used a London penetration depth of $\lambda = 70$ nm, typical for 100 nm thick Al films [154]. From chapter 4, which discussed the Fabry-Pérot quantum interference effects, we know that supercurrent in TI-junctions is mostly carried by quasi-ballistic surface states [142]. So, if we assume the ballistic junction case (junction length $l <$ mean free path $l_e \simeq 200$ nm [84]), the coherence length can be estimated using $\xi = \hbar v_F/\Delta'$, with $v_F \simeq 5 \times 10^5$ m/s the Fermi velocity of the surface states in Bi_2Se_3 [84, 85], and Δ' the induced superconducting gap in the surface state. For a typical $\Delta' \simeq 120 - 180$ μeV extracted from single junction devices [22], we obtain $\xi \simeq 1.8 - 2.7$ μm, which is much longer than the length of our junctions, placing them in the short junction limit [59]. Therefore, we can expect the CPR to be determined by equation 2.20b in section 2.3.3 with τ_n values given by equation 2.31.

5.2 Characterization of asymmetric TI-SQUID

The measurement layout used for characterizing the asymmetric SQUID device is given in figure 5.2(a). We first measured IVCs at 20 mK for different external magnetic fields ($B_\perp$). The IVC of TI-SQUID corresponding to zero applied magnetic field is plotted in figure 5.2(b). As seen here, like in the case of single junctions (see Chapter 4), the IVC show hysteretic behaviour possibly due to heating effects [22, 155]. Since we are interested in the critical current of the device, for the rest of the analysis, we will only consider the bias sections of the IVC when the junction switches from the superconducting state to the resistive state (purple lines)and ignore the section with retrapping current (orange lines). The response of the TI-SQUID with respect to the applied bias current I and external magnetic field $B_\perp$ is plotted in the form of a differential resistance dV/dI map in figure 5.2(c). Here, one can see the modulations of the critical current from the asymmetric SQUID (bright lines).

We used a threshold voltage of 3 μV as the criteria for determining the critical current, $I_{s,c}$, of the SQUID. The obtained critical current modulations of the device are plotted as closed symbols in figure 5.2(d). As expected, we see a background envelope (solid lines) arising from the magnetic field modulation of the critical current $I_{r,c}$ of the reference junction (Fraunhofer pattern). Note that the magnetic field axis in 5.2(d) is offset from $B_\perp$ by $B_{off} = 5\mu T$ to $B_{0\perp} = B_\perp + B_{off}$. This is to account for the constant offset in the measurement setup. From the maxima of the Fraunhofer pattern of reference junction, we get $I_{r,c}$ to be 19.4 μA. Now, to get the current modulations of the test junction (I_t), we remove the background Fraunhofer pattern from $I_{s,c}$. The current-flux relation (CΦR) of our test junction can be obtained by converting the magnetic field to flux, $\Phi_{ext} = B_{0\perp} A_{eff}$ using the observed modulation period of $\simeq 11.6\mu$T ($A_{eff} \simeq 180$

μm^2) corresponding to one flux quantum Φ_0. See figure 5.3(a) showing the extracted CΦR for positive and negative bias currents. From here, we get $I_{t,c} \simeq$ 880 nA, and the critical current asymmetry in our SQUID device is $I_{r,c}/I_{t,c} \approx$ 22. Using the simulated value of loop inductance, $L = 29$ pH, we get $\beta_L \simeq 0.28$, which is not $\ll 1$. So, we must keep the inductance contributions to equation 5.1 to interpret the measurements better.

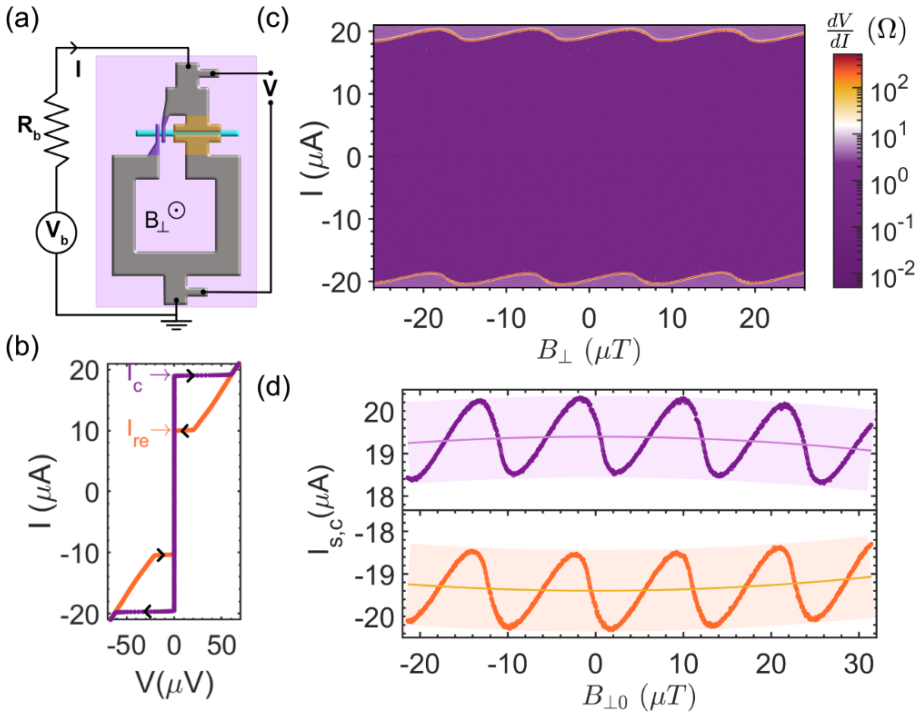

Figure 5.2: (a) Layout of the SQUID with both the test and reference junction made from the same Bi_2Se_3 nanobelt. The current-voltage characteristic is measured using a 4-point setup. (b) IVC at $T = 20$ mK with zero applied magnetic field. The arrows indicate the direction of the sweep (starting from zero), and the IVC shows hysteretic behaviour. Here, I_c and I_{re} correspond to the critical current and retrapping current of the device, respectively. (c) Differential resistance of the SQUID as a function of bias current and externally applied magnetic field measured at $T = 20$ mK. (c) The critical current of the SQUID for positive (upper panel) and negative (lower panel) bias current. The light-coloured lines indicate the background envelope from the magnetic field pattern of the reference junction (Fraunhofer pattern). Here, we adjusted the magnetic field data for a constant offset, B_{off}.

5.2.1 Estimating inductance from CΦR

Using the CΦR of the test junction, we can also get estimates of the loop inductance of the SQUID. From equation 5.2, for the negligible inductance case, when

the external flux is an integer multiple of Φ_0, we get $\varphi_t \simeq \varphi_{r,max}$. Now, if we assume the CPRs of the test and reference junction have the same functional shape, $f(\varphi) \simeq g(\varphi)$, the CΦRs will have the maxima at external flux values, which are an integer multiple of Φ_0. However, from measured CΦR s given figure 5.3(a), the maxima (indicated with magenta and blue arrows) are offset from the corresponding integer values of Φ_{ext}/Φ_0. This shift arises due to the magnetic field produced by the circulating current in the SQUID loop, and this can be quantified in terms of a parameter $\Delta\Phi_L$ defined as the distance between the observed location of the maxima pair (positive and negative current bias)corresponding to an integer Φ_{ext}/Φ_0. From equation 5.1, it is straightforward to see that $\Delta\Phi_L = L(I_{r,c} - I_{t,c})$, with $(I_{r,c} - I_{t,c})/2$ the circulating current in the loop when the SQUID critical current is maximized [147]. From the measured shifts in CΦR, we obtain $\Delta\Phi_L \simeq 0.28\ \Phi_0$ corresponding to a loop inductance value of approximately 29 pH, which is close to the simulated value. The extracted SQUID loop inductances for different temperatures up to 900 mK are given in figure 5.3(b). Here, within the error bars of our data, we do not see a considerable change in the inductance of the SQUID loop with temperature, suggesting that the majority contribution to L comes from the geometric inductance.

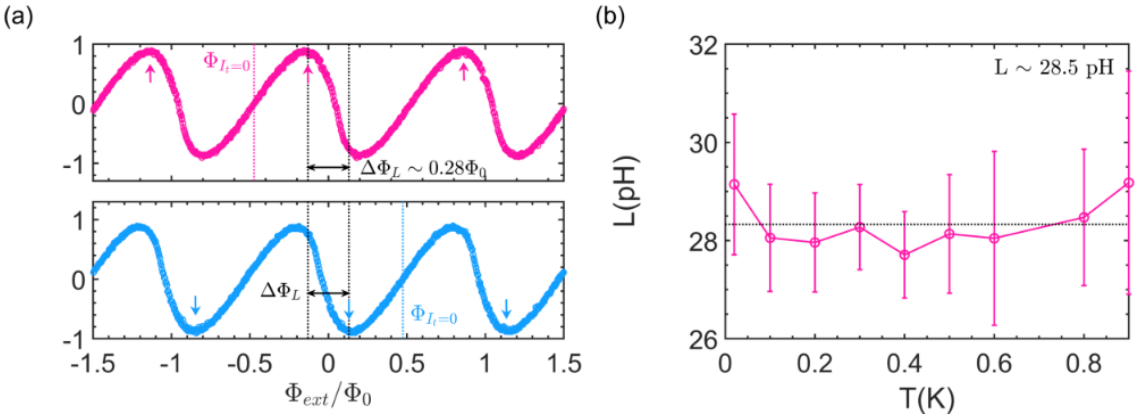

Figure 5.3: (a) Extracted CΦR of the TI test junction at $T = 20$ mK for both positive (magenta) and negative (blue) current bias directions of the asymmetric TI-SQUID and corresponding arrows indicate the location of the maxima of the CΦR. The shift in the location of positive and negative maxima from integer Φ_{ext}/Φ_0 positions due to finite inductance can be quantified in terms of $\Delta\Phi_L = L(I_{r,c} - I_{t,c})$, with $(I_{r,c} - I_{t,c})/2$ being the circulating current in the SQUID loop. (b) Loop inductance of the SQUID estimated using $\Delta\Phi_L$ as a function of bath temperature. The error bars represent the standard deviations of L obtained from different pairs of the CΦR maxima corresponding to various integer Φ_{ext}/Φ_0 locations that are used for estimating $\Delta\Phi_L$. As one can see, L remains constant around the value of 29 pH, confirming that it is dominated by the geometric inductance of the device.

5.2.2 CPR and Skewness

Now, to obtain the CPR of the test junction, we need to convert magnetic flux to the phase drop across the test junction. This can be achieved by subtracting the magnetic flux value at which the current of the test junction goes to zero $\varphi_t = 2\pi(\Phi_{ext} - \Phi_{I_t=0})/\Phi_0$. The extracted CPRs of our junction at various temperatures are shown in figure 5.4(a). Note that these are not the true CPRs of the test junction, as we did not consider the nonlinearity of the flux-phase relation due to the inductance term in equation 5.1. We will address this issue in the section where we discuss the data fitting (see section 5.3). The extracted CPRs are forward skewed at low temperatures and evolve into a more sinusoidal CPR at higher temperatures. In figure 5.4(b), we show the obtained CPR of our S-TI-S junction measured at 20 mK along with a sinusoidal CPR of the same amplitude. The deviation of CPRs from conventional sinusoidal CPR can be quantified in terms of skewness, commonly defined as $S = (2\varphi_{max}/\pi) - 1$, where φ_{max} corresponds to the phase at which the current through the junction is at the maximum value, namely the critical current of the junction [27, 145, 156]. For an ideal short SNS with transmission probability $\tau_n = 1$ (see Chapter 2), one gets a maximum skewness $S = 1$ with $\varphi_{max} = \pi$, whereas for $\tau_n \ll 1$, $S = 0$ (sinusoidal CPR).

We found that for our test junction, $\varphi_{max} = 0.67\pi$ (see the dotted line in figure 5.4(b)) at 20 mK, which corresponds to a skewness $S = 0.34$. Here, even if we consider the inductance of the SQUID loop, the position of φ_{max} does not change since in the limit of a small screening parameter, the extracted CPRs are only affected in a small phase region around odd multiples of π (see section 5.3). Figure 5.4(c) shows the monotonic decrease of the skewness S with increasing temperature, asymptotically approaching zero for higher temperatures. In Chapter 4, we qualitatively showed that most of the current in our junctions is carried by ballistic TSSs. Here, we will compare the skewness parameter to the predictions for different junction regimes to show the validity of our observation. For a short diffusive junction ($\xi > l$ with $\xi = \sqrt{\hbar D/\Delta'}$), one expects a maximum skewness value of $S_D = 0.255$ at zero temperature (see dotted line in figure 5.4(c)) [156]. Below 200 mK, the CPR of our junction shows skewness values above this diffusive limit. So, pure diffusive transport cannot describe the transport in our TI junction. In the fully ballistic limit, using the expression for transmission probabilities τ [105] (see equation 4.4 given in Chapter 4), we obtain $S = 0.41$ at 20 mK, which is larger than the experimentally observed value for S. This would suggest that the Josephson currents in our devices are not carried exclusively by the ballistic TSSs; there might be bulk states contributing to the overall current as well.

This is also supported by the temperature dependence of the critical current (I_c) of the test junction shown in figure 5.4(d). Here, the open symbols correspond to the measured value of I_c extracted from the CPRs given in figure 5.4 (a). As indicated by the dashed lines, around 600 mK, we observe a drastic change in the slope of the I_c vs. T curve. As observed in similar junctions [25, 32], this might

point towards the presence of two different types of Josephson transport channels with different T_c values. The modes with higher T_C (same as the Al electrode, T_c= 1.15K) can be attributed to the ballistic TSSs. In contrast, the Josephson current contribution that vanishes fast, around 600 mK, could be attributed to the diffusive transport modes due to bulk states. Since magnetotransport data from these devices show low bulk mobility values, this also supports the possibility of bulk diffusive transport modes in our junctions [85].

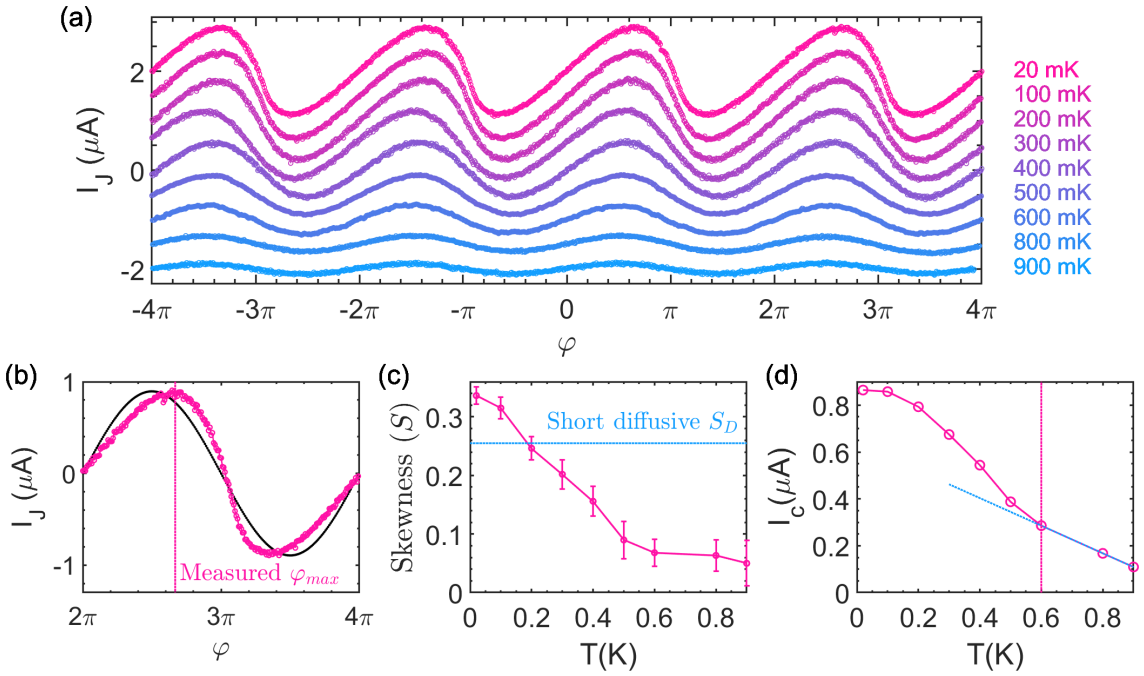

Figure 5.4: (a) Evolution of the extracted CPR of the TI test junction with varying temperature. (b) Extracted CPR at 20 mK (magenta) along with a sinusoidal curve with the same amplitude (black) to emphasize the deviation of CPR from the conventional case. The vertical dotted magenta line indicates the location of φ_{max} for the measured CPR. (c) Measured skewness of CPR vs. temperature. Below 200 mK, S is greater than the zero temperature limit S_D, and the transport of the junction can not be explained fully by pure diffusive transport modes. (d) Critical current of the test junction as a function of temperature. The open symbols are the measured data extracted from the CPRs shown in panel (a). The vertical dotted line indicates the temperature at which the slope of I_c vs T changes. This points towards the presence of two different types of transport channels with a higher (around T_c of Al, 1.15 K) and a lower (around 600 mK) critical temperature.

5.3 Fitting CPR of S-TI-S junctions

We have seen from previous sections of this chapter that supercurrent in our junctions might be carried by TSSs and bulk states. To estimate their contributions, we fit the CPR measured at 20 mK. For the Josephson current carried by the TSSs, we use the model of a short ballistic junction (see equation 2.20b in section 2.3.3) along quantized transport modes with transmission probabilities dictated by the geometry of the device (see equation 2.31) [105, 142]. We remove an oxide thickness of 5nm from the nanobelt dimensions and find the perimeter, $P = 452$ nm. Now, using a typical k_F of 0.55 nm^{-1} based on magnetotransport measurements performed by us on similar Bi_2Se_3 nanobelts [84–86], we calculated τ value for various modes arising from TSSs [21, 32, 105, 142]. A polar plot of the obtained τ values as a function of (continuous) angle θ (see solid line) is given in figure 5.5(b). The transmission probabilities of the individual quantized transport modes are shown as open symbols. We find that, in total, 39 modes are arising from TSSs. As seen in Chapter 4, we have indications that most of the current in our junction is carried by the modes on the top surface of the nanobelt. So, out of the total 39, we only consider the 29 modes (orange open symbols) travelling on the top surface($\theta < 48°$) to be contributing to the ballistic portion of the supercurrent. More than half of these modes have τ values close to 1, resulting in an average τ value of 0.92 for the modes on the top surface. We describe the Josephson current carried by TSSs modes with θ above 48° (purple open symbols) that go around the perimeter of the nanobelt along with the bulk states using a diffusive multi-mode model based on Dorokhov distribution of transmission probabilities [65] (see Chapter 2 section 2.3.4). Since the value of normal state conductance G_N of diffusive channel is unknown, we take it as a fitting parameter in our analysis.

The fitted contributions to the CPR of our junction at 20 mK are shown in figure 5.5(c). Note that to fit the CPR, we had to assume a temperature ($T_{fit} \simeq$ 195 mK) higher than the bath temperature of 20mK. This discrepancy might originate from elevated quasi-particle temperatures or additional current noise typically observed in SNS junctions [144, 157]. Moreover, we also assume a reduced value of T_c for diffusive channel [25, 32] (T_{c2}), and for simplicity, the initial fits are carried out without including inductance the finite inductance effect. The values of the various parameters used in the fitting process are provided in table 5.1.

The best fit is obtained when out of the total critical current of $\approx$ 880 nA (see magenta circles corresponding to measured data and blue line corresponding to the sum of ballistic and diffusive parts) of the test junctions, $\approx$ 657 nA are carried by ballistic TSSs on the top of the junction (orange line), and $\approx$ 223 nA are carried by the diffusive transport modes (purple line). In agreement with our experiment, the presence of these diffusive transport modes with lower skewness will result in an

Fitted parameters				Other parameters	
T_{fit}	γ	T_{c2}	G_N	T_{c1}	k_F
195 mK	0.8	650 mK	1.5×10^{-3} S	1.15 K	5.5 nm^{-1}

Table 5.1: Table showing various parameters used for fitting the measured CPR

overall reduction of the observed skewness of our junction compared to transport carried entirely by the TSS.

As seen in figure 5.5(c), the fitted curves deviate from the measured CPR around $\varphi_t = \pi$ and the measured CPR does not cross zero at $\varphi_t = \pi$. This can be accounted for by including the finite inductance back into the analysis of the CPR. For this, we use the fitted CPR for $L = 0$, and numerically calculate the values of phases φ_t and φ_r across the test and reference junction for each value of external flux Φ_{ext} when the loop inductance $L = 29$ pH [53, 142]. In figure 5.5(d), we have plotted the variation of φ_r and φ_t with respect to φ. Here, one can see deviations from linear behaviour of φ_t (dashed blue lines) around π in the region shaded in grey. Now, by including inductance, we can reproduce the measured CPR relation more accurately, as shown in figure 5.5(e). This is reflected in the residual from the fit ($\Delta I = I_J - I_{fit}$) given in figure 5.5(f). Here, we see a peak around π for the residual corresponding to the fit without inductance(blue curve), and after including inductance, this peak around π in residuals vanishes (green curve). From figure 5.5(e), it can be seen that the loop inductance does not significantly affect the phase position of the maximum of the CPR. This is because the position of the maximum and the minimum of the CPR are outside the phase region where φ_t deviates from the linear dependence on φ (in between the dashed grey lines). Therefore, as mentioned earlier, the various skewness values we extracted for the CPRs are valid, and this is in agreement with the quasi-ballistic nature of our devices. Also, the true CPR of our junctions corresponds to the $L = 0$ fit (blue line) plotted in figure 5.5(e).

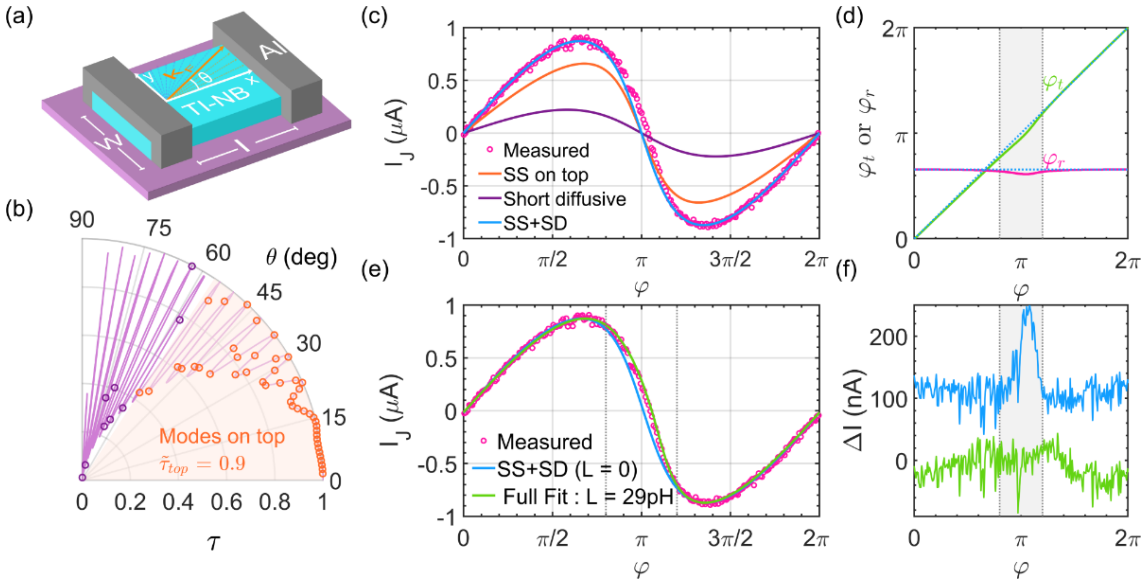

Figure 5.5: (a) Sketch of an S-TI-S junction showing quasi-particle trajectories in terms of the angle θ made with longitudinal momentum axis with $\theta = \tan^{-1}(\frac{k_x}{k_y})$. (b) Angle-dependent transmission probabilities of various transport modes in the junction, assuming extreme chemical potential mismatch at the interface (see equation 2.31). The orange circles correspond to the modes which are fully contained on the top surface of the junction, and the purple dots correspond to the modes that propagate around the nanobelt's perimeter. (c) Measured CPR of the junction at 20 mK (magenta circles) along with fitted curves assuming zero inductance, $L = 0$. The orange curve is the current contribution from the ballistic TSSs on the top surface of the junction, and the purple line shows the diffusive contributions to the CPR. The sum of both ballistic and diffusive modes is given as the blue curve. (d) Variation of φ_t and φ_r with respect to φ, the extracted phase across the junction assuming a linear variation of phase with Φ_{ext}. Most of the deviation occurs around $\varphi \simeq \pi$ (see the shaded region, $0.8\pi - 1.2\pi$). (e) Measured CPR of the junction (magenta circles) along with the fitted curve considering a finite loop inductance of $L = 29$ pH (green line) . The zero inductance fit is given for comparison (blue). The region in between the dashed grey lines corresponds to regions mostly affected by inductance as in panel (d), whereas φ_{max} of the CPR lies outside this region. (f) Difference or residual between the measured data and fit ($\Delta I = I_J - I_{fit}$). The data are offset for clarity. For the zero inductance case, there is a peak in ΔI around π, indicating the deviation of the fitted curve around π from the measurement data. The green curve corresponds to the fit, including the loop inductance, resulting in a pronounced reduction of the peak around π. The shaded region is the same as in panel (d).

5.4 Additional asymmetric SQUID data

Over the course of this PhD study, we measured multiple asymmetric SQUIDs apart from the one discussed in the previous section. Here, we provide some of the data corresponding to those measurements. All the measurements discussed in this section were carried out in our 300 mK ^{3}He dipstick.

5.4.1 CPR from other devices

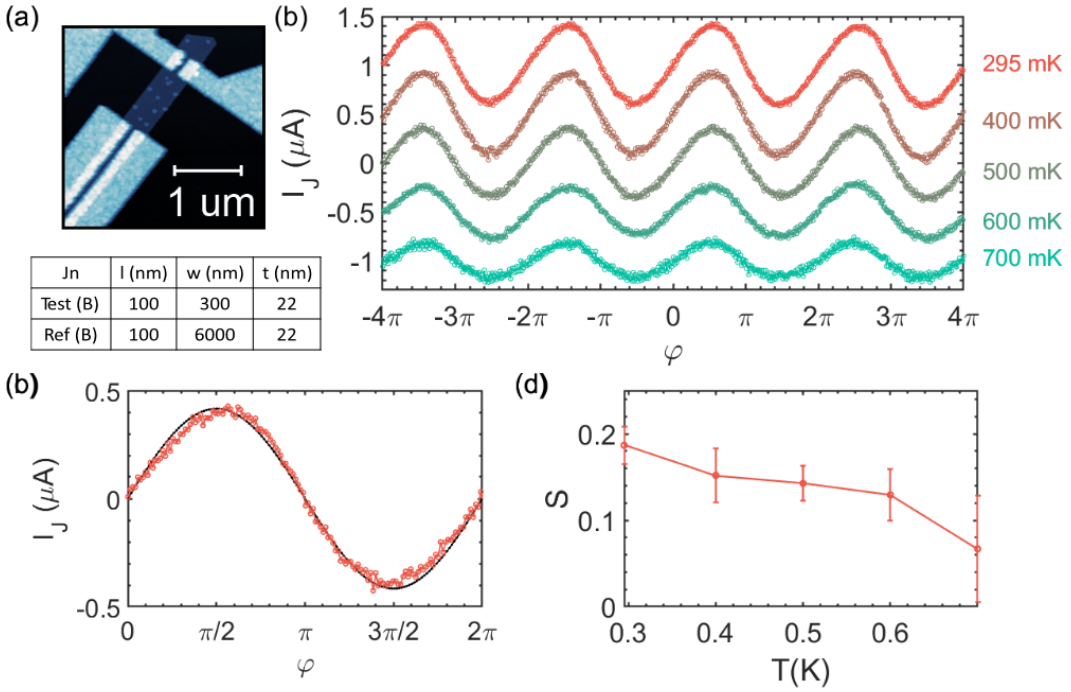

Jn	l (nm)	w (nm)	t (nm)
Test (B)	100	300	22
Ref (B)	100	6000	22

Figure 5.6: (a) AFM of the SQUID with both the test and reference junction made from the same Bi_2Se_3 nanobelt with layout B. Note that the regular triangular patterns visible on the TINR are AFM tip-induced artefacts. The dimensions of the junctions used are provided in the table below. (b) Evolution of the extracted CPR of the TI test junction with varying temperatures. (c) Extracted CPR at 265 mK (orange) along with a sinusoidal curve with the same amplitude (black).(c) Measured skewness of CPR vs. temperature.

Figure 5.6 shows extracted CPR data corresponding to the asymmetric SQUID device $S2$ shown in figure 5.6(a). The test and reference junctions of the SQUID use layout B (see Chapter 3 section 3.1 for more). This SQUID device has a critical current asymmetry of 1:28 between the test and reference junction at 295 mK, and the SQUID loop has the same dimension as device $S1$ (see section 5.1). As seen in figure 5.6(b) and (c), as in the previous case for device $S1$, we observe a skewed CPR at lower temperatures. The skewness of the extracted CPR is plotted

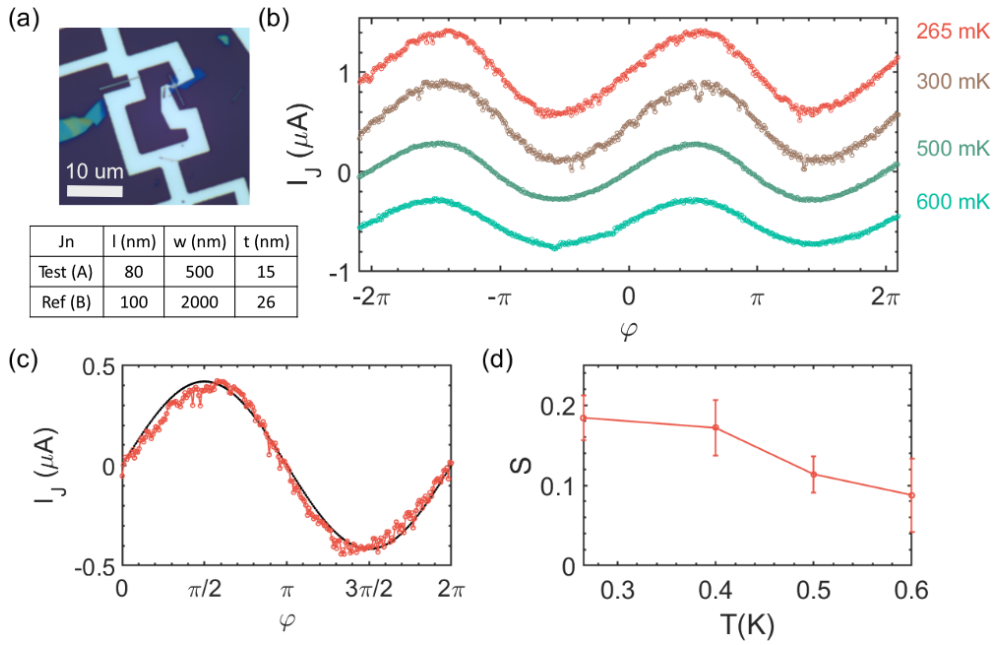

Jn	l (nm)	w (nm)	t (nm)
Test (A)	80	500	15
Ref (B)	100	2000	26

Figure 5.7: (a) Optical image of a SQUID formed out of junctions realized on two different TINRs. Here, the test junction uses layout A, and the reference junction uses layout B. The dimensions of the junctions are provided in the table below. (b) Evolution of the extracted CPR of the TI test junction with varying temperatures. (c) Extracted CPR at 295 mK (orange) along with a sinusoidal curve with the same amplitude (black).(c) Measured skewness of CPR vs. temperature.

in figure 5.6(d). This device also shows a similar skewness value of ≈0.2 around 300mK, and the skewness of the CPR decreases with temperature. Though this is smaller than the maximum skewness value expected for short diffusive junctions, it is consistent with the skewness value from device $S1$ at 300 mK. So, we expect a similar kind of behaviour in this junction where both diffusive and ballistic transport modes carry supercurrent.

In figure 5.7, we have plotted the CPR data extracted from the asymmetric SQUID device $S3$ fabricated using two adjacent Bi_2Se_3 NRs. The dimensions and layout of this device are shown in figure 5.7(a). Unlike previous devices, this device has a reduced critical current asymmetry of 1:11. But this should not affect the extracted CPR much. Looking at the skewness of the device, we have a similar behaviour as devices $S1$ and $S2$. Since two different representative devices showed similar behaviour at 300 mK as the primary SQUID device discussed in this chapter, we can conclude that in our Al-Bi_2Se_3-Al junctions, the transport is carried by both ballistic and diffusive transport modes. Though the contributions from each kind of transport mode might depend on the details of the junctions, we expect the majority of the supercurrent to be carried by ballistic TSSs.

5.4.2 Asymmetric TI-SQUID and Josephson diode effect

The pn-junction diode is one of the widely used components in electronics. They show selective current flow based on biased direction. In recent years, there has been a growing interest in developing a superconducting diode, which superconducts more in one direction than another [158–170]. In various physical systems, the superconducting diode effect (SDE) can arise due to different mechanisms. But one of the key ingredients for observing SDE seems to be the breaking of time-reversal symmetry and inversion symmetry [158, 160–167, 170]. Devices showing superconducting diode effects have been demonstrated experimentally and some them are listed in [160–166, 168–170].

Flux-biased asymmetric SQUIDs with finite β_L are known for having nonreciprocal supercurrent transport at specific flux values [53]. Recently, it was pointed out that asymmetric SQUIDs formed out of junctions with nonsinusoidal CPR can show SDE even when the loop inductance is negligible due to the presence of higher harmonics in the CPR[159, 167]. As we have seen in the previous sections of this chapter, our Al-Bi_2Se_3-Al junctions show slanted nonsinusoidal CPR. So, our asymmetric SQUIDs, realized for the CPR extraction, should act like a Josephson diode. This can be seen in the CΦR plot of device $S1$ given in figure 5.3. (a). Here, at each flux point, the supercurrent value corresponding to positive and negative bias does not correspond to the same magnitude. To quantify this, we make use of the definition of Josephson diode efficiency given by [168, 169]

$$\eta = \frac{I_c^+ - |Ic^-|}{I_c^+ + |Ic^-|} \tag{5.3}$$

where I_c^+ and I_c^- correspond to the critical current positive and negative bias direction, respectively. For device $S1$, we get a diode efficiency of $< 5\%$, which is very small compared to some of the already reported SQUID-based Josephson diodes with efficiencies of roughly 25-40% [168, 169]. This is because the critical current asymmetry in our device is very large as they are designed for CPR extraction, and the relative change in the amplitude of the critical current modulations of the SQUID with external flux is very small (see figure 5.2(d), here $I_c^+ - |Ic^-| \ll I_c^+ + |Ic^-|$ for every value of external magnetic field). This results in reduced diode efficiency.

In figure 5.8, we instead provide data from device $S4$ with a lower critical current asymmetry of 1:4 between junction 1 and junction 2. This level of asymmetry is not ideal for CPR extraction; however it can act as a better superconducting diode. A false-coloured SEM image layout of the SQUID device is provided in figure 5.8.(a). From the IVCs of the device at two different flux values shown in figure 5.8.(b), we can see the supercurrent asymmetry in the device. The full current flux relation of the SQUID device in both positive(red) and negative(green) directions is plotted in figure 5.8.(c) and the diode efficiency η is plotted figure 5.8.(d). Here, we achieved a maximum diode efficiency of $\simeq 12\%$. However,

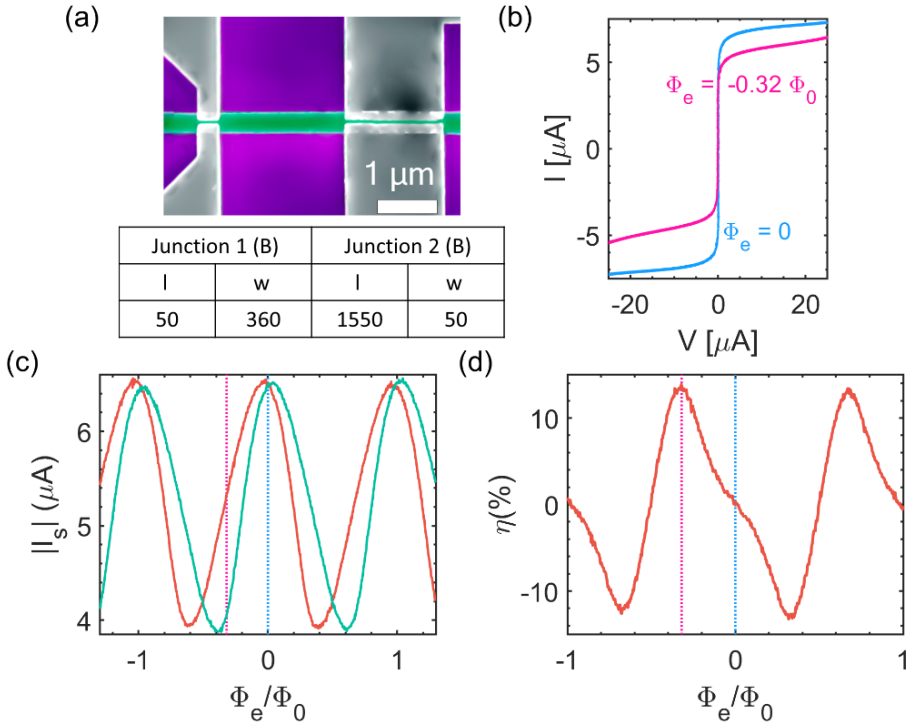

Figure 5.8: (a) False coloured SEM image showing the layout of the asymmetric SQUID *S4* with junctions made from the same Bi_2Se_3 nanobelt. The dimensions of the junctions are given in the table below. (b) The IVC of the device measured at two different flux values, $\Phi_e = 0$ (blue) and $\Phi_e = -0.32\Phi_0$ (magenta), showing asymmetry in I_c^+ and I_c^-. (c) The CΦR of the SQUID device for I_c^+ (red) and I_c^- (green) directions. The dotted line corresponds to the location of IVCs shown in panel (b). (d) Superconducting diode efficiency of the device as a function of flux bias. We get a maximum $\eta \simeq 12\%$ at a flux bias value of $\Phi_e = -0.32\Phi_0$.

this is also smaller than the reported values of efficiencies (25-40%) for SQUID based Josephson diode [168, 169]. From numerical calculations (data not shown), we know that for a simple asymmetric TI-SQUID based on two Al-Bi_2Se_3-Al, the maximum η value we can achieve is less than 25%. This is because, for better diode efficiency, one needs to have SQUIDs formed out of the junctions with CPRs of different functional shapes, and we can not change the shape of the CPRs of our junctions drastically by changing the dimension of the junctions [159]. For higher diode efficiencies, one will have to make use of an asymmetric SQUID made out of a junction with sinusoidal current phase relation and TI-junction [159].

6 AC Susceptibility of a Bi_2Se_3 nanoribbon Josephson junction

In this chapter, we examine the microwave characteristics of a nanoribbon-based Al-Bi_2Se_3-Al junction integrated into an rf-SQUID loop, coupled to a quarter wavelength ($\lambda/4$) coplanar waveguide (CPW) microwave resonator through mutual inductance. Despite the use of nanoribbons to mitigate bulk contributions to transport properties, a significant number of transport modes persist within the topological surface states (TSSs), attributed to the elevated chemical potential in Bi_2Se_3 nanoribbons [85]. Given the relatively large population of resulting Andreev bound states (approximately 50 modes) within our TSSs, and assuming that the relaxation rate of these bound states exceeds both the average level spacing and the coupling strength between the Andreev bound state system and the resonator, we do not expect to observe prominent circuit Quantum Electrodynamics (QED) phenomena like avoided level crossing due to vacuum Rabi-oscillations [61]. Nevertheless, valuable insights into the dynamics of Andreev bound states can still be obtained through the analysis of the ac-susceptibility, as discussed in the subsequent section.

6.1 Ac susceptibility (χ) of a Josephson junction

First, we introduce the concept of magnetic susceptibility following ref. [171] and discuss how it relates to the reactive and dissipative parts of the admittance of a Josephson junction. The magnetic susceptibility is a measure of the current response, δI_{ac}, to a time-dependent ac flux, $\delta\Phi_{ac}$,

$$\chi = \frac{\delta I_{ac}}{\delta \Phi_{ac}}. \tag{6.1}$$

Using the expression of the generalized flux in a Josephson junction $\Phi = \Phi_0\varphi/2\pi$, with $\Phi_0 = h/2e$ the superconductive flux quantum and φ the phase difference across the Josephson junction, we can rewrite:

$$\chi = \frac{2\pi}{\Phi_0}\frac{\delta I_{ac}}{\delta \varphi_{ac}}, \tag{6.2}$$

which has a unit of one over inductance. The corresponding admittance is given by $Y = \chi/i\omega$. The finite frequency susceptibility of a Josephson junction is determined by 3 contributions [172, 173]:

1. The adiabatic Josephson response (frequency-independent):

$$\chi_j(\varphi) = \frac{2\pi}{\Phi_0}\frac{\delta I_j}{\delta\varphi}, \tag{6.3}$$

   with $I_j(\varphi)$ the total Josephson current.

2. The finite frequency nonadiabatic, i.e. dynamical, response due to the relaxation of the Andreev bound state populations:

$$\chi_D(\omega,\varphi) = -\sum_n |I_{nn}|^2 \frac{\partial f_n}{\partial E_n}\frac{\omega}{\omega - i\Gamma_{in}}. \tag{6.4}$$

   Here I_{nn} are the diagonal matrix elements of the Andreev current operator (see Appendix B), and $\partial f_n/\partial E_n$ are the derivatives of the Fermi-Dirac population distributions with respect to the bound state energies E_n. The quantity Γ_{in} describes the diagonal relaxation rate responsible for bringing the ac-driven non-equilibrium population distribution back to a thermal distribution.

3. The dynamical response caused by transitions between the Andreev bound state levels induced by microwave photon emission or absorption:

$$\begin{aligned}\chi_{ND}(\omega,\varphi) = &-\sum_{n,m\neq n} |I_{nm}|^2 \frac{f_n - f_m}{E_n - E_m} \\ &\times \frac{\hbar\omega}{\hbar\omega - (E_n - E_m) - i\hbar\Gamma_{mw}}.\end{aligned} \tag{6.5}$$

   Here I_{nm} are the non-diagonal matrix elements of the Andreev current operator (see Appendix A), and $f_{n,m}$ the Fermi-Dirac population distributions of the n-the and m-th Andreev bound state level, respectively. The quantity Γ_{mw} describes the non-diagonal relaxation rate. The dominating non-diagonal matrix elements are given for electron-hole symmetric Andreev bound state pairs $|I_{n,-n}|$ and $|I_{-n,n}|$ [173, 174].

The total complex-valued magnetic susceptibility is, therefore, given by

$$\begin{aligned}\chi(\omega,\varphi) &= \chi_J + \chi_D + \chi_{ND} \\ &= \chi' + i\chi''.\end{aligned} \tag{6.6}$$

It is important to note that χ_D and χ_{ND} contribute both to the real and imaginary part of the magnetic susceptibility and, therefore, to the reactive and dissipative (lossy) part of the junction admittance $Y = \chi/i\omega$, respectively, whereas χ_J contributed only to the reactive part.

6.1.1 Properties of χ_D

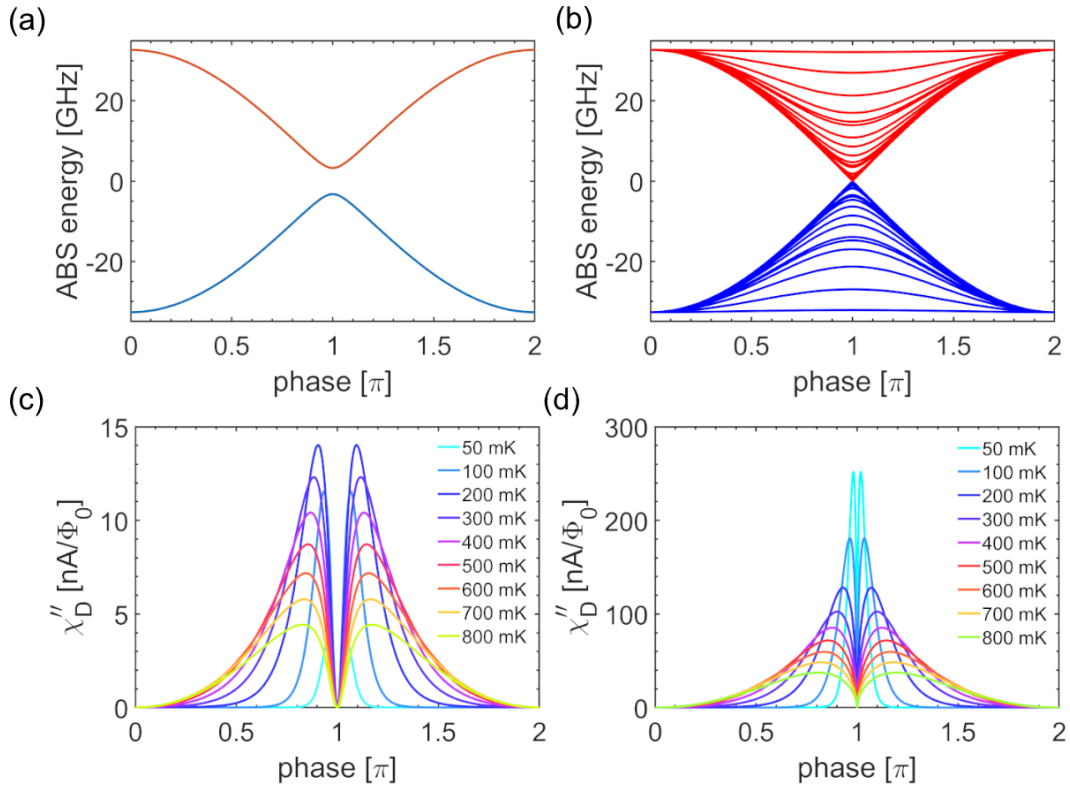

Figure 6.1: (a) Andreev bound state pair for a transmission coefficient $\tau = 0.99$. (b) Andreev bound state spectrum involving topological surface states of a TI nanoribbon. (c) and (d) Population relaxation (diagonal) contribution to the losses χ''_D at various temperatures for the bound state spectrum shown in panels (a) and (b), respectively.

In the following, we will discuss how the properties of χ_D behave as a function of phase, temperature, and frequency. From equation 6.4 we can separate $\chi_D = \sum F_1(\varphi)F_2(\omega)$ in a frequency-independent term $F_1(\varphi) = |I_{nn}|^2 \partial f/\partial E_n$ and a frequency-dependent term $F_2(\omega) = \omega/(\omega - i\gamma_{in})$. In $F_1(\varphi)$ the phase-dependence is given by $|I_{nn}|^2$, i.e. the square of the current phase relation (CPR) with zeros at phase $0, \pi$, and 2π and two peaks located at the extrema of the CPR. The temperature dependence in $F_1(\varphi)$ is given by the derivative of the Fermi-Dirac distribution with respect to the energy $\partial f/\partial E_n$. As a function of energy, it has the shape of a peak (negative) with a half width at half maximum $\sim 2k_BT$ centered at the chemical potential. As a consequence only bound states in the proximity of $2k_BT$ around the chemical potential contribute to χ_D. In figure 6.1 (b) we show the evolution in temperature of the population relaxation losses χ''_D as a function of phase for a single pair of Andreev bound states (see panel (a)). For clarity, here we consider the frequency dependence $F_2(\omega)$ to be a constant equal to one. Upon increasing temperature χ''_D reaches a maximum for temperatures close to

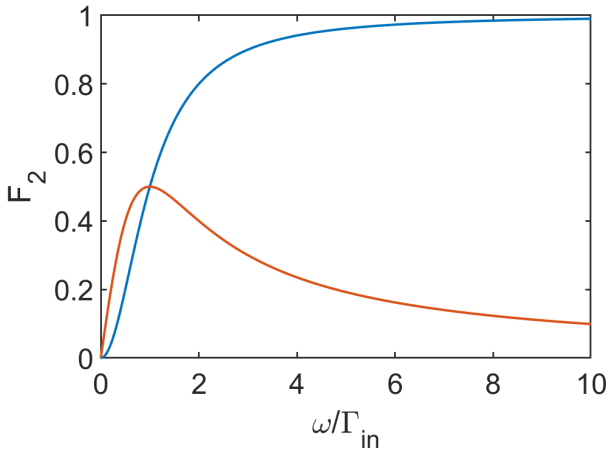

Figure 6.2: Frequency dependence of the real and imaginary part of the population relaxation contribution to the susceptibility χ_D.

the gap in the bound state spectrum $\Delta E_n = E_n(\pi) - E_{-n}(\pi)$. For even higher temperatures the double-peaked feature becomes wider and smaller in amplitude. In Fig 6.1(c) we show the bound state spectrum of an ideal topological surface state using $L = 100$ nm, $w = 89$ nm and a Fermi wavevector $k_F = 5 \cdot 10^8$ m^{-1} (see Appendix A). The corresponding χ_D'' for various temperatures is shown in panel (d). For temperatures larger than the minimum gap ΔE_n only a decay and broadening of the double-peaked feature with increasing temperature is observed.

Next, we discuss the frequency dependence of the real and imaginary part of χ_D shown in figure 6.2. For probing frequencies ω smaller than the inelastic relaxation rate, Γ_{in}, both the real and imaginary part of χ_D start from zero at zero frequency and increase with increasing frequency. For $\omega > \Gamma_{in}$ the real part of χ_D starts to saturate approaching 1, whereas the imaginary part of χ_D decays with increasing frequencies after reaching a maximum at $\omega = \Gamma_{in}$.

6.1.2 Properties of χ_{ND}

Since our junction is shorter than the superconducting coherence length in the TI, $L < \xi$ (see below), hereafter, we consider only microwave transitions between electron-hole symmetric bound states, which is a reasonable approximation for short ballistic junctions [61, 65]. For small probing frequencies $\omega \ll \Delta/h$ one expects microwave transitions between Andreev bound states, $\hbar\omega = E_n(\varphi) - E_{-n}(\varphi) = 2E_n(\varphi)$, only in proximity of $\varphi = \pi$ where the level spacing between electron-hole symmetric bound states reaches a minimum.

In the case of long lifetimes where $\Gamma_{ND} \ll \omega$, this is expected to manifest as a double-peaked pattern in χ_{ND}'' with its center at $\varphi = \pi$. Conversely, if the lifetimes are short ($\Gamma_{ND} \geq \omega$), these two peaks will converge into a single peak.

Additionally, as temperature increases beyond $k_BT > \hbar\omega$, the peak's amplitude begins to diminish. This phenomenon arises from the thermal population of the bound states, nearing 1/2 for Andreev level spacings smaller than k_BT (see eq. 6.5).

6.2 Observed parameters of resonator RL and SQUID loop

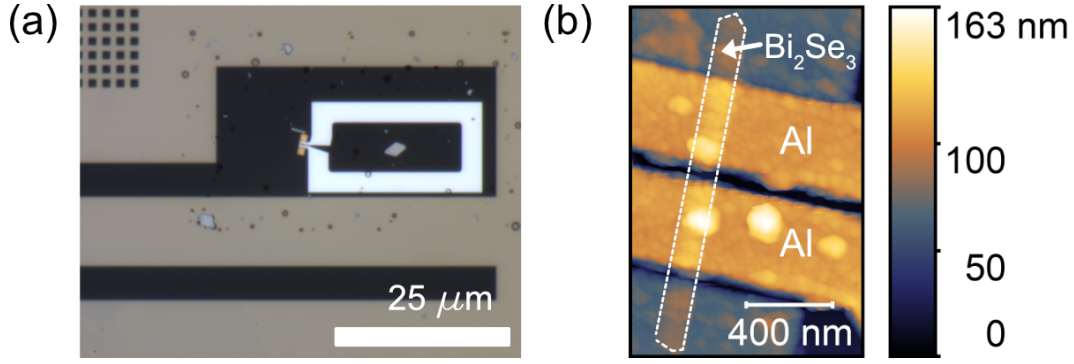

Figure 6.3: (a) Optical image of the shorted end of the NbN $\lambda/4$ resonator (dark grey) on a sapphire substrate (black). The Al rf-SQUID loop is seen in light grey. (b) Atomic force microscopy image (topography) of the Al-Bi_2Se_3-Al junction embedded in the Al rf-SQUID loop shown in panel (a). The white dashed line indicates the outline of the TI nanoribbon.

Most of the design parameters of our resonators are described in Chapter 3 section 3.2.2. In this chapter, we will discuss measurements based on resonator RL and the RF-SQUID attached to it. To quickly, the resonator RL had a design frequency of 627 MHz. From the measured values of the higher harmonics of the resonator, we get the fundamental frequency of the resonator to be 628 MHz. Here, we used the fact that the frequencies of the higher modes of $\lambda/4$ resonator are given by $\omega_n = \omega_0(2n+1)$ with $n > 0$ a positive integer to get the fundamental frequency. In table 6.1, we summarize the measured mode frequencies of resonator RL together with the fitted internal and external quality factors (see Chapter 3 section 3.2.2 for details on the fitting procedure).

For the rf-SQUID loop inductance, we need to fulfil the condition $\chi L_{loop} < 1$ such that we can neglect screening effects and, therefore, obtain a linear change of phase across the junction with applied external magnetic flux (see Appendix A). For typical critical currents of our TI junctions $I_c \sim 1$ μA we get the condition $L_{loop} < I_c^{-1}\Phi_0/2\pi \simeq 300$ pH. For the Al SQUID loop shown in figure 6.3 (a) with length $l_{loop} = 25$ μm and width $w_{loop} = 13$ μm we calculated the self-inductance by solving the Maxwell London equations on the loop geometry [153], giving

Mode number	$\omega_n/2\pi$	Q_{int}	Q_{ext}
3	4.4 GHz	93000	160000
4	5.65 GHz	32000	88000
5	6.91 GHz	33000	78000
6	8.16 GHz	79000	70000

Table 6.1: Frequency, internal and external quality factor of resonator RL with fundamental mode frequency $\omega_0 \simeq 628$ MHz for mode numbers 3-6

$L_{loop} \simeq$ 27pH. For the mutual inductance between the loop and the resonator, we can obtain an upper bound got an upper bound of 16 pH (see chapter 3, section 3.1.4). However, the real value might be smaller by a factor of up to 4 due to return currents causing a reduction of the mutual inductance. As shown below, our measurements point towards a smaller value $M \simeq 3-7$ pH. In figure 6.3 (b), we show the AFM image of the Al-Bi_2Se_3-Al junction from the SQUID loop, and for this junction we get a width of 89 nm, length of 100 nm and thickness of $t = 13$ nm.

6.3 Experimental details

In this section, we will discuss some of the experimental observations, and data analysis is performed in a later section. The detailed experimental setup used for the measurements of our RF-SQUIDs coupled to CPW resonators is given in Chapter 3. Our measurements involve obtaining resonance characteristics of RF-SQUID devices using a VNA while changing the flux bias with the help of a superconducting coil.

From the circuit analysis presented in Appendix A, one can directly link the measured frequency shift $\delta\omega$ and the changes of the internal losses $\delta(1/Q_{int})$ as a function of phase bias to the real and imaginary part of the junction's magnetic susceptibility [171]:

$$\frac{\delta\omega}{\omega_0} = \frac{M^2}{2L_R}\chi' \tag{6.7}$$

$$\delta\left(\frac{1}{Q}\right) = \frac{M^2}{L_R}\chi'', \tag{6.8}$$

with M the mutual inductance and $L_R \simeq L_l l \simeq 23$ nH the effective inductance of the $\lambda/4$ resonator. Considering that the critical current of our junction lies in the range $100-500$ nA [28] for given nanoribbon dimensions, we obtain from our $\delta\omega/\omega$ data fits shown below a mutual inductance value in the range $M \simeq 3-7$ pH.

The microwave power at the output of the VNA was chosen such that we obtain maximum signal-to-noise while staying in the linear regime for the susceptibility

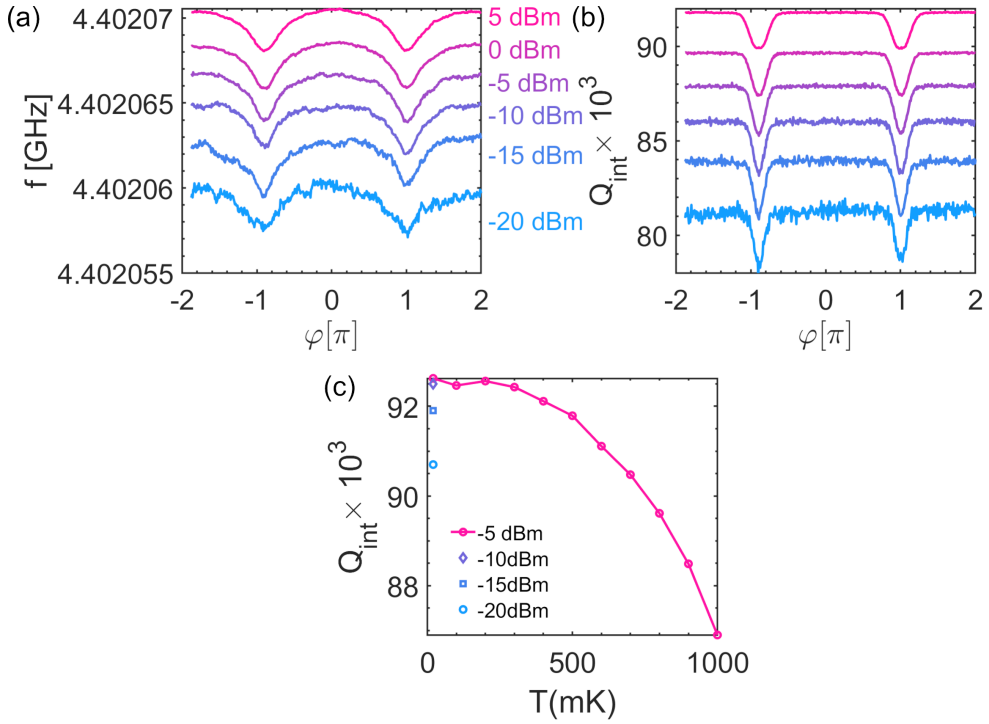

Figure 6.4: (a), (b) Measured phase dependence of the coupled system resonance and internal quality factor, respectively, for resonator mode $n = 3$ at various VNA output powers at $T = 20$ mK. (c) Internal quality factor at zero phase bias for various applied microwave powers together with the temperature dependence at $P = -5$ dBm as a function of temperature.

measurements, i.e. $\delta\Phi_{ac} \ll \Phi_0$. In figure 6.4 (a) and (b), we show the measured phase dependence of the resonance frequency and internal quality factor, respectively, of the coupled system for resonator mode $n = 3$ at various VNA output powers at $T = 20$ mK. For output power $P > -5$ dBm, we observe distortions (flattening out of dip features) of the signals around phase bias $\varphi = \pi$, whereas for lower powers we do not observe any significant change in the signal except for degradation of the signal-to-noise. Therefore, we used $P = -5$ dBm as the VNA output power throughout all the following measurements.

6.4 Temperature dependence of χ

In figure 6.5 (a) and (c) we show the measured resonance frequency and internal quality factor as a function of applied phase bias $\varphi = 2\pi\Phi_{ext}/\Phi_0$ at various temperatures for mode number 3 and 6, respectively. The corresponding quality factors are shown in panels (b) and (d), respectively. In panels (e) and (f) we show the resonance frequencies of the same two modes as a function of temperature for a fixed applied magnetic flux $\Phi_{ext} = 0$, respectively. At low temperatures, we see

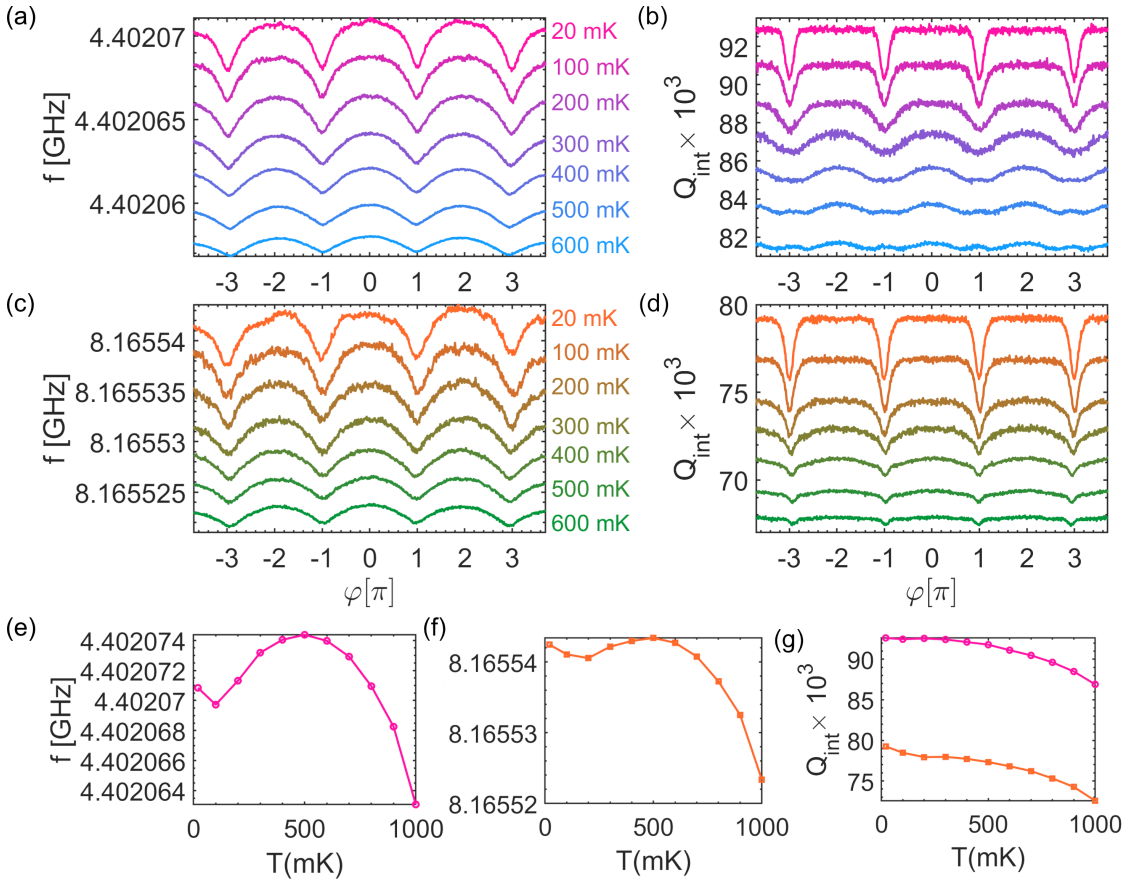

Figure 6.5: (a),(c) Phase bias response of the resonance frequency at various temperatures for modes number 3 and 6, respectively (curves are offset for clarity). (b), (d) Phase bias response of the internal quality factor at various temperatures for modes number 3 and 6, respectively (curves are offset for clarity). (e), (f) Resonance frequency as a function of temperature at zero phase bias for mode numbers 3 and 6, respectively. (g) Internal quality factor as a function of temperature at zero applied phase bias for mode number 3 (magenta symbols) and mode number 6 (orange) symbols.

the effect of two-level fluctuator noise on the resonator, which is characterized by the upturn of the resonance frequency below a temperature $T_n = \hbar\omega_n/2k_BT$ [175]. The effect of the noisy environment can also be directly seen in the rather noisy frequency data shown in 6.5 (c) for temperatures below 200 mK. For larger temperatures, TLFs at the resonator frequency 8.16 GHz become saturated (approaching equal thermal population), resulting in much smoother resonator frequency vs phase measurements. From the frequency data vs phase shown in 6.5 (a) and (c), we can extract the relative resonance shift $2\delta f/f_0$, which is shown in panel (a) of figure 6.6. Here, the data taken at 4.4 GHz are displayed as solid lines, and the data measured at 8.16 GHz as dashed lines. Similarly, from the Q_{int} data vs phase shown in figure 6.5 (b) and (d), we can extract the loss changes

$\delta(1/Q_{int})$ shown in panel (b) of figure 6.6.

First, we discuss the relative frequency shift data shown in figure 6.6 (a). No obvious difference (within the TLF noise-induced fluctuations) between the data measured at 4.4 GHz and 8.16 GHz can be observed at any temperature. From figure 6.2, we see that the real part of χ_D saturates for frequencies larger than Γ_{in}. Since χ'_D contributes to the relative frequency shift (see eq. 6.7) together with the observation that the $\delta f/f_0$ vs phase data are rather insensitive to the probing frequencies, 4.4 GHz and 8.16 GHz, points towards the fact that the inelastic scattering rate Γ_{in} is smaller than 4.4 GHz.

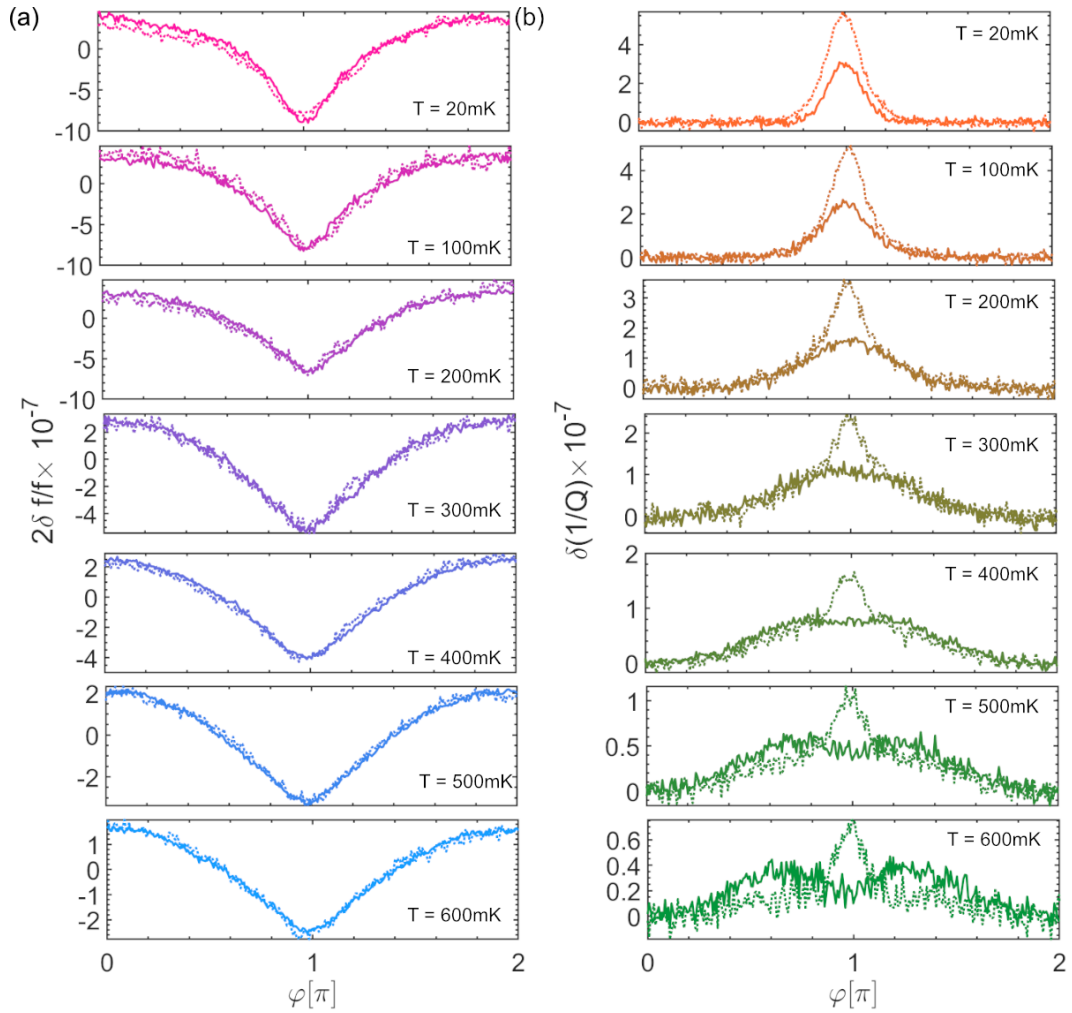

Figure 6.6: (a) Extracted frequency shift as a function of externally applied phase bias for various temperatures. The solid lines are the data probed at $\omega/2\pi = 4.4$ GHz. The dotted lines represent the measured data probed at $\omega/2\pi = 8.16$ GHz. (b) Extracted added losses as a function of externally applied phase bias for various temperatures. The solid lines are the data probed at $\omega/2\pi = 4.4$ GHz. The dotted lines represent the measured data probed at $\omega/2\pi = 8.16$ GHz.

Next, we discuss the added losses vs phase data shown in 6.6 (b). In contrast to the frequency shift vs phase data, the added losses vs phase data behave quite differently at the two frequencies. At low temperatures, we observe a dissipation peak centred at $\varphi = \pi$, which we can attribute to microwave-induced transitions when the Andreev transition energy is in resonance with the resonator mode frequency $\hbar\omega_n = 2E_n(\varphi)$. The dissipation peak is strongly suppressed for temperatures above 500 mK when probing at 4.4 GHz, whereas a clear dissipation peak is visible up to 600 mK for probing frequency 8.16 GHz. In fact, for temperatures $k_BT > \hbar\omega$ Andreev bound state pairs with separation $2E_n \simeq \hbar\omega$ around $\varphi = \pi$ approach equal population $f_n \simeq f_{-n}$ reducing the contribution of χ_{ND} to the magnetic susceptibility (see eq. 6.5).

6.5 Data Analysis

In this section, our goal is to determine the two relaxation rates, Γ_{in} and Γ_{mw}. To achieve this, we perform a concurrent fitting of the frequency shift $\delta f/f_0$ and the supplementary loss data $\delta(1/Q_{int})$ at various temperatures using equations 6.6, 6.7, and 6.8. To facilitate this procedure, we adopt the following assumptions:

1. We treat the bulk and surface states independently, and only microwave transitions between electron-hole symmetric bound states are considered.

2. The bulk has a lower induced superconducting gap and corresponding critical temperature as compared to the surface states. Indications of this phenomenology are given by the typical critical current vs temperature data we observe in our Bi_2Se_3 nanoribbon Josephson junctions [142]. For the surface state, we assume a gap of $\Delta_s = 0.75\Delta_{Al}$ with $T_c^s = 1.15K$ [22] and for the bulk states we assume a critical temperature $T_c^b = 0.7K$ [142] and induced gap of $\Delta_b = \Delta_s T_c^b/T_c^s \simeq 0.5\Delta_{Al}$.

3. For the topological surface states contributing to the Josephson transport we assume a Fermi wave vector $k_F = 5e8$ m^{-1}. From the AFM imaging, shown in figure 6.3(b), we infer a junction width of 89 nm, length of 100 nm and thickness of $t = 13$ nm. Moreover, for the TSS transport channels, we assume transmission coefficients τ_n typical for Dirac materials (see equation 2.31 in Chapter 2).

4. The bulk only contributes via diffusive channels to the Josephson transport. We, therefore, treat the bulk using the short diffusive junction model with the characteristic Dorokhov distribution of transmission coefficients [65, 142]. We adjust the parameters of the bulk (mainly normal conductance) such that the ratio between the Josephson current at zero temperature carried by

surface states and diffusive (bulk) states is $\sim 2:1$. This value is close to the one we obtained from CPR measurements in similar Josephson junctions using asymmetric dc SQUID measurements [142].

5. The relaxation times are phase-independent. Moreover, we do not discern between the relaxation times in the bulk and surface states.

6. The only fitting parameters are the effective temperature T_{eff}, and the relaxation rates Γ_{in} and Γ_{mw}.

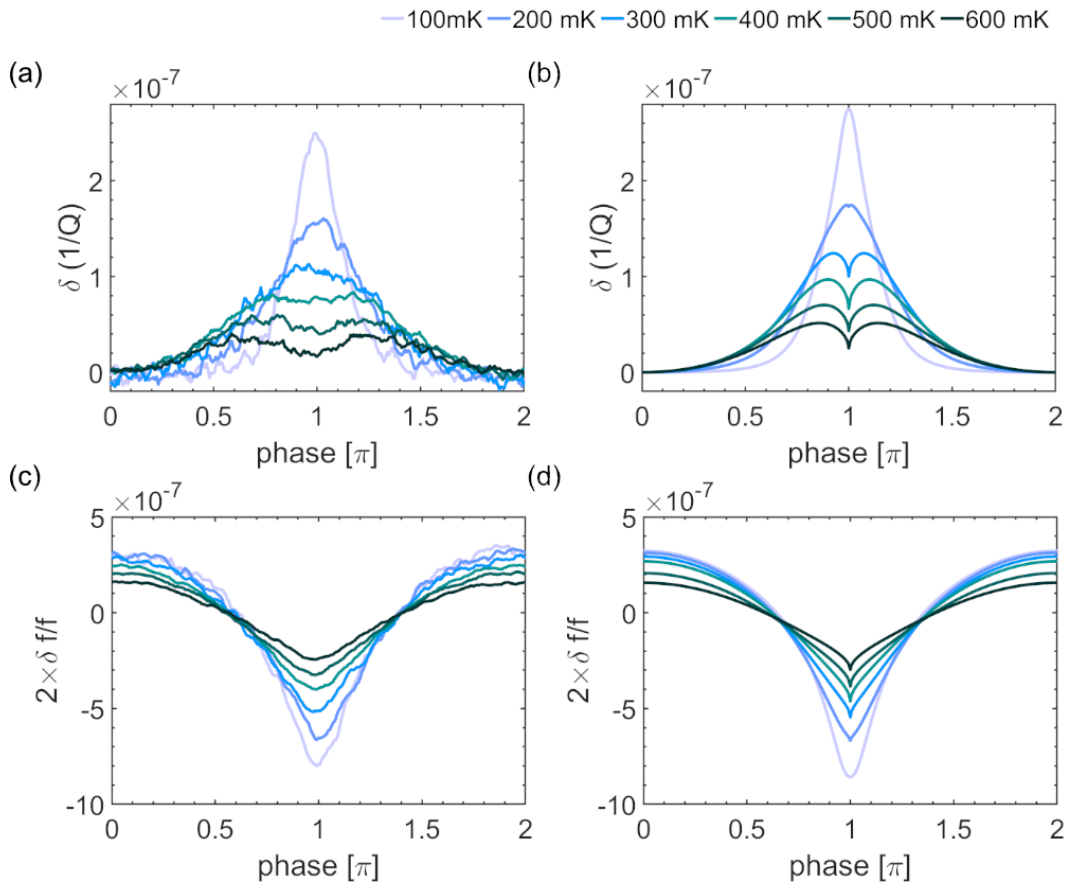

Figure 6.7: (a) Measured added losses as a function of phase at various temperatures probed at $\omega/2\pi = 4.4$ GHz. (b) Fitted added losses. The inset shows the fitted temperature T_{eff} (c) Measured frequency shift as a function of phase at various temperatures probed at $\omega/2\pi = 4.4$ GHz. (d) Fitted frequency shift.

In figure 6.7, we show in the left column the experimental data of the phase dependence of the added losses (panel (a)) and the relative frequency shift (panel (c)) at various temperatures probed at $\omega/2\pi = 4.4$ GHz. The right column (panels (b) and (d)) shows the corresponding fits. The fitted effective temperatures

are shown in the inset of panel (b). This offset at low temperatures could be attributed to the non-ideal microwave filtering of our measurement setup, which inevitably leads to an overheating of the electronic system at low temperatures in our junction above the bath temperature. The extracted relaxation rates as a function of the bath temperature are shown in figure 6.9 as blue open circles (Γ_{in}) and blue discs (Γ_{mw}).

Similar to the data shown in figure 6.7 in figure 6.8, we show in the left column the experimental data of the phase dependence of the added losses (panel (a)) and the relative frequency shift (panel (c)) at various temperatures probed at $\omega/2\pi = 8.16$ GHz. The right column shows the corresponding fits. Here, we used the same effective temperatures obtained in the fits of the 4.4 GHz data shown in figure 6.7. The extracted Γ_{in} and Γ_{mw} at various bath temperatures are shown in figure 6.9 as red open circles and red discs, respectively.

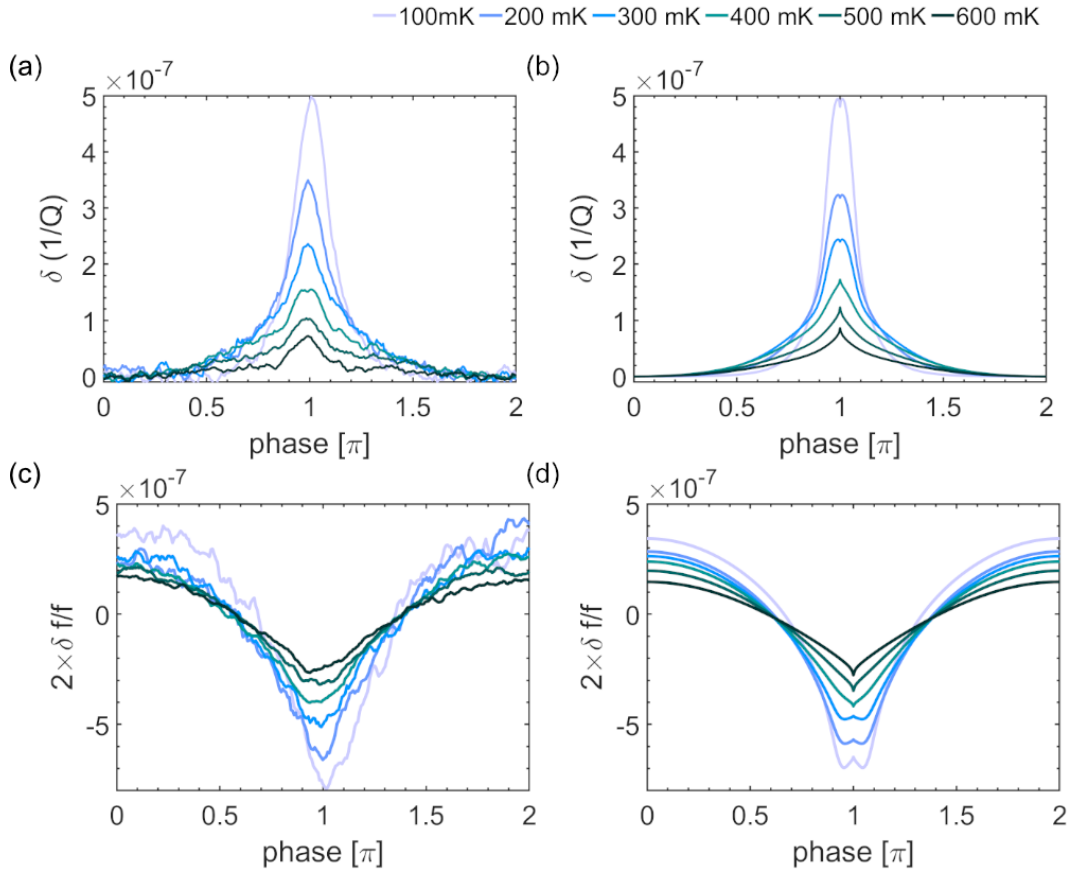

Figure 6.8: (a) Measured added losses as a function of phase at various temperatures probed at $\omega/2\pi = 8.16$ GHz. (b) Fitted added losses. (c) Measured frequency shift as a function of phase at various temperatures probed at $\omega/2\pi = 8.16$ GHz. (d) Fitted frequency shift.

6.5.1 Discussion

The inelastic relaxation rates Γ_{in} shown in figure 6.9 are rather constant at temperatures up to $T_{bath} = 400$ mK and then decrease by a factor ~ 1.5 at $T_{bath} = 600$ mK. This is in stark contrast to the temperature dependence observed in long diffusive SNS junctions [171], where the inelastic scattering rate follows a linear in T behavior reminiscent of a phase coherence time in diffusive metallic systems. From the typical phase coherence length in Bi_2Se_3 nanoribbons [86], $l_\phi \simeq 300$ nm, we obtained from weak anti-localization measurements at $T = 1$ K, we can calculate the dephasing rate $\Gamma_\phi = l_\phi^2/D$ with $D = E_F\mu_e/2e$ the diffusion constant. Here $E_F \simeq 180$ meV is the typical chemical potential and $\mu_e \simeq 3000$ cm^2/Vs the typical mobility in our TI nanoribbons. With these values, we obtain $\Gamma_\phi \simeq 300$ GHz. This value is much larger than the Γ_{in} values shown in figure 6.9 at $T = 600$ mK. A possible reason for this discrepancy could be that weak anti-localization corrections in the conductance are mainly determined by diffusive trajectories and, therefore, less sensitive to ballistic transport modes. Because the Josephson current primarily flows through quasi-ballistic modes, the relaxation rates of these modes may not be correlated with Γ_ϕ.

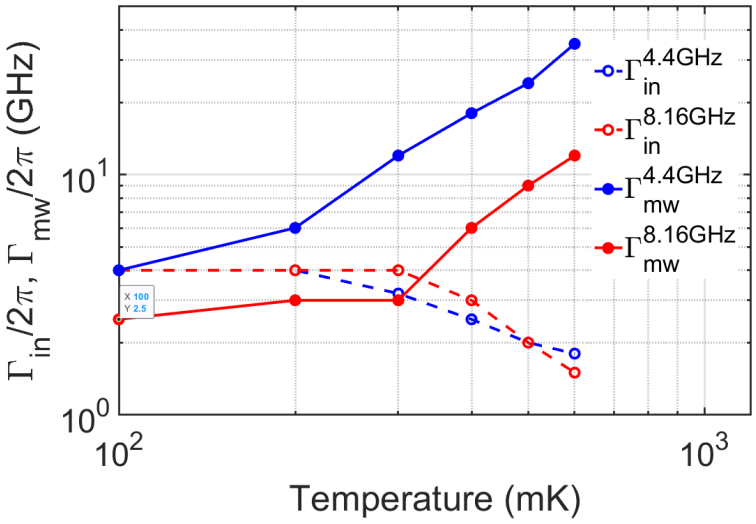

Figure 6.9: Relaxation rates Γ_{in} and Γ_{mw} at probing frequencies 4.4 GHz and 8.16 GHz.

However, the rather unconventional temperature dependence at higher temperatures (decrease of relaxation rate) of Γ_{in} is not clear yet. One possible explanation could be the simplified assumption in the data analysis of having the same relaxation rate in both the TSSs and bulk states (see item 5) in the previous section). Assuming a smaller relaxation rate in the TSS might explain the discrepancy at higher temperatures once the weight of the bulk states to χ_D starts to decrease due to the proximity of the bath temperature to the critical temperature of the

bulk-induced gap.

The relaxation rates Γ_{mw} at probing frequencies 4.4 GHz and 8.16 GHz increase with temperature, possibly indicating a power law dependence at higher temperatures, T^p, with $p \simeq 2-3$. At lower temperatures, the rates approach saturation values around $\Gamma_{mw}^{4.4GHz} \simeq 4$ GHz and $\Gamma_{mw}^{8.16GHz} \simeq 2.5$ GHz, respectively. The main relaxation mechanisms for Andreev bound state qubits are related to phonon or photon emission [61, 176]. For the phonon-mediated relaxation rate, one can estimate an upper bound given by the electron-phonon scattering rate [176] $\Gamma_{eph} \simeq \epsilon^3/(\hbar k_B^2 \Theta_D^2)$ with ϵ the energy spacing between a bound state pair or the temperature and $\Theta_D \simeq 180$ K the Debeye temperature of Bi_2Se_3. Considering the largest energy scale in our system $\sim 1K$ we obtain an upper bound for the relaxation rate $\Gamma_{eph} \simeq 4$ MHz which is more than 3 orders of magnitude smaller than the values of Γ_{mw} we observe. The maximum relaxation rate caused by photon emission (Purcell effect) is given by the coupling strength between the Andreev system and the resonator mode. For mutual inductance values in the range $3-10$ pH we obtain coupling values $g/2\pi < 6$ MHz (see Appendix A for details). Therefore, both the electron-phonon coupling and Purcell effect cannot explain the large relaxation rates, Γ_{mw}, we observe.

Another possibility to take into account is the interaction between the Andreev bound state system and a continuum of electronic states. This continuum may arise from the fact that the induced gap in the bulk (possibly also in the TSSs) is not a hard gap, but rather a soft gap with sub-gap states forming a continuum where Andreev bound states can dissipate their energy.

7 Towards reducing bulk contributions to transport in Bi_2Se_3 devices

A major problem that one faces in devices fabricated using 3D-topological insulators (TI) Bi_2Se_3 is the unavoidable presence of bulk conductivity. These bulk states often mask the effects of unconventional topological surface states (TSSs) or complicate the transport analysis on these devices. As seen in Chapters 5 and 6, our S-TI-S junctions have significant contributions to transport arising from conducting bulk states and in this chapter, we will discuss our attempts to tackle this problem. In the first section, we will briefly discuss our attempts to reduce bulk carriers with electrostatic gating and in the following section, we will discuss a gated device made using thin Bi_2Se_3 nanoribbon from a slightly different growth process than the nanoribbons discussed in most of this thesis. In the last section, we will discuss the possibility of reducing bulk contributions to supercurrent transport in S-TI-S junction by increasing the length of the junction.

7.1 Reducing bulk contributions to transport in Bi_2Se_3 nanoribbons: electrostatic gating

In this section, we will discuss two different approaches we took for reducing bulk contribution to transport in our Al-Bi_2Se_3-Al junctions. First, we will discuss suspended S-TI-S junction with local gate electrodes, and then we will discuss a device in which a Bi_2Se_3 nanoribbon is sandwiched in between a top and bottom layer of h-BN dielectric-based gates.

7.1.1 Transport of suspended Al-Bi_2Se_3-Al junctions

Typically, we are only able to change the chemical potential of our junction by roughly ≤ 10 meV (see Chapter 4), and this is not enough to bring up the chemical potential close to the Dirac point of the TINRs [85, 131]. Moreover, as seen in 2.6 of Chapter 2, we have a trivial 2DEG formed at the interface between our Bi_2Se_3 nanoribbon and the substrate due to band bending effects[84, 85]. By implementing a suspended junction, one hopes to avoid this unintentional 2DEG

by elevating the nanoribbon from the substrate and thereby not allowing the TI-weaklink part of our junction to touch the substrate. Now, with the use of a local gate (with a width of 50 nm) defined in between the Al electrodes (separation between the electrodes is between 100-120 nm), we expect to have better electrostatic control over the transport in our junction than what is typically achieved by a global back gate. The schematic of a suspended junction is shown in figure 7.1(a). This junction follows the same fabrication process as discussed in Chapter 3 section 3.1; the only difference is that when depositing the Al electrodes, we also deposit Al on top of the gate with a gap of roughly 100 nm from the TINR on both sides to form a split gate like structure on top of the local Au gate that sits under the TINR. They form a gate controlled by a single voltage source, and this is done to increase the effectiveness of the gating process by surrounding more of the TINR with the gate. The corresponding SEM images of the device SS1 discussed here are shown in figure 7.1(b).

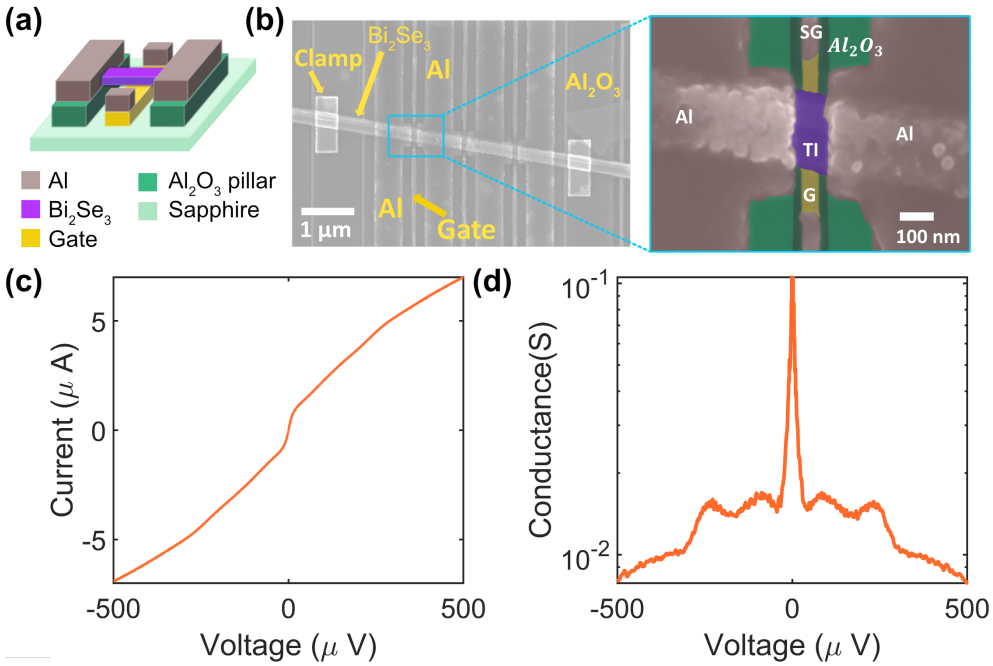

Figure 7.1: (a) Schematic of a suspended Al-Bi_2Se_3-Al junction with Al_2O_3 pillar and local back(Ti/Au/Pd) plus side(Pt/Al) gates. (b) SEM images of suspended nanowire junction with various parts labelled. On the right, we have given false zoomed-in SEM image showing device SS1. Here, SG corresponds to split/side gate. (c) and (d) Measured IVC and differential conductance of device SS1 at 300 mK, respectively.

We characterized the fabricated suspended junctions in our 300mK system. The IVC and differential conductance corresponding to device SS1 are plotted in figure 7.1(c) and (d), respectively. As seen here, the IVC of the junction is rather rounded and does not show any hysteresis behaviour like our typical

junctions. This is mainly due to the elevated base temperature and lack of high-frequency filtering in our 300 mK dipstick compared to our dilution fridge. For better characterization of such junctions, one needs to use a measurement setup where the DC lines are properly filtered for high-frequency noise. Now, in the conductance spectra, we observe some features arising from multiple Andreev reflections pointing towards the good quality of the junctions. Here, though we tried to gate the device, the gate leads started to leak at a gate voltage $V_g <$ -2V, and we could not observe any significant gating effects in these devices. Similar behaviour was observed in multiple suspended junctions fabricated in this manner. Sapphire is a high-insulating substrate; this level of leaking in our devices is unexpected. However, we suspected that the leakage might have resulted from the highly porous nature of the Al_2O_3 pillars that are deposited using e-beam evaporation. After a few failed attempts, we abandoned the idea. Later, we found out that the positive AR-P 6200 series (CSAR 62) e-beam resist we utilize for fabricating the junctions develops cracks under strain, which may result in the shorting of nearby structures. Since our suspended junctions are fabricated in a region with various high profiles, it resulted in straining the resist layer and, in turn, might have also contributed to the leaking gates in our suspended junctions.

7.1.2 Gated devices with h-BN dielectric

In the case of 2D materials, h-BN flake or film has been used for both material isolation as well as a gate dielectric [177]. A high-quality h-BN flake can withstand electric fields with a strength of 1V/nm, and this makes it an ideal choice for gate dielectric. By using h-BN-based gates on both the top and bottom of our devices, we wanted to see if we could gate Bi_2Se_3 nanoribbon devices through the Dirac point. In our experiments, we used h-BN flakes exfoliated from cosmetic-grade h-BN powder, which could withstand an electric field of $\simeq$ 0.7V/nm. Anyway, we fabricated some nanoribbon-based devices with normal contacts (Ti/Au) to check the feasibility of using such h-BN flakes for achieving electrostatic gating in our devices to get closer to the Dirac point. An optical image, along with a schematic showing the cross-section, of one of our fabricated dual-gated TINR devices (BSH1) is shown in figure 7.2(a). Detailed information on the fabrication of the device is given in section 3.1 of Chapter 3. The TINR ribbon used in this experiment had a width of $\simeq$ 480 nm and a thickness of $65 - 70$ nm (the nanoribbon came with a ridge parallel to the axis of the ribbon with a width of roughly 150 nm and 5nm raised compared to the rest of the nanoribbon). The TINR is measured in a four-probe configuration, where the voltage probes are separated by 3μm. The gates are controlled by individual voltage sources. Also, the top and bottom hBN flakes are roughly $\simeq$ 25-30 nm and $\simeq$ 15-20 nm thick, respectively. All the measurements shown here are performed in our 300 mK dipstick at base temperature.

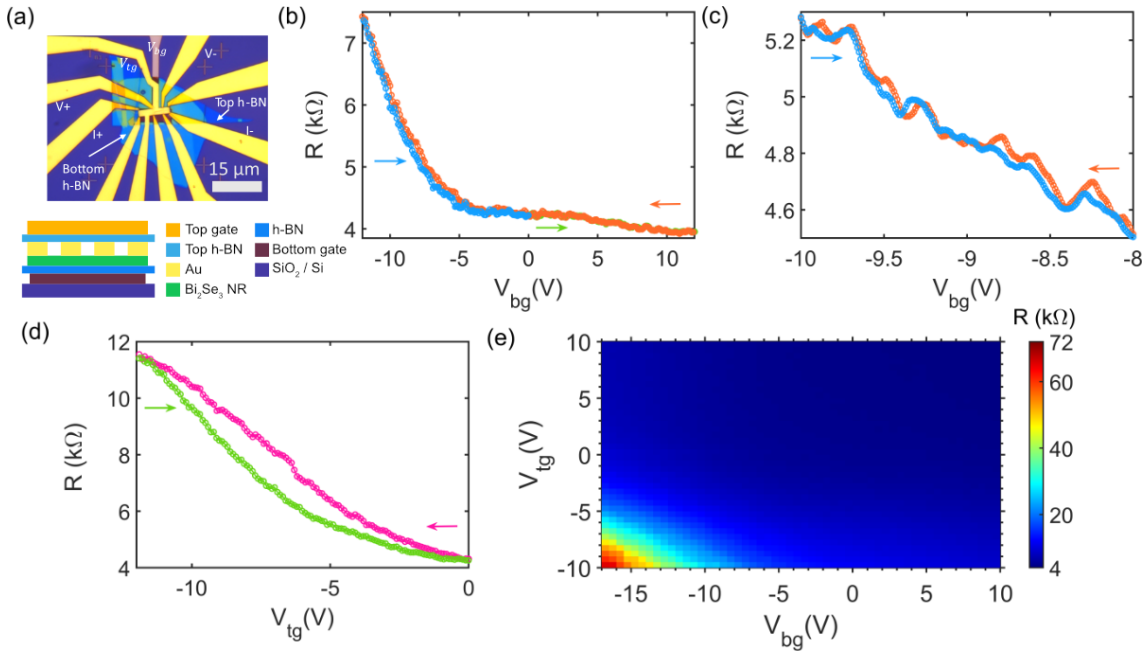

Figure 7.2: (a) Optical image of TINR device BSH1 with top and bottom gate electrode using h-BN flakes as gate dielectric. Here, top and bottom h-BN flakes are roughly 15-20 and 25-30 nm thick, respectively. The bottom section of the image shows a schematic cross-section of the device (b) Change in resistance of the device with respect to applied back gate voltage (V_{bg}) with zero top gate voltage (V_{tg}). Here, we sweep V_{bg} from 0V to 12V (green curve), 12V to -12V (orange curve) and -12V to 0V (blue curve), and the arrows indicate the direction of the sweep. With more negative gate voltages, the resistance of the devices starts to go up, and at V_{bg} =-12V, the resistance of the device gets almost doubled in value compared to the zero voltage case showing the n-type nature of our devices. (c) Resistance curves showing a finer gate sweep performed in the small V_{bg} range of -8V to -10V in both directions($V_{tg} = 0$). Here, we see some oscillation in the resistance of the device, which may originate from the transversal quantization effect. (d) Response of the device to applied top gate voltage V_{tg} with zero V_{bg}. Here, we see a hysteresis in the top gate response of the device, and this might be related to accumulated charges in hBN or the interface between the TINR and h-BN. (e) A resistance map of the device with both V_{bg} and V_{tg} applied, we managed to increase the resistance of the device up to $\simeq$ 72 kΩ, which is almost 15 the initial resistance of the device with zero gate voltage.

We first measured the IVC of the device at zero back gate (V_{bg})and top gate voltages (V_{tg}). From here, we get a device resistance of $\simeq$ 4.2 kΩ and a corresponding sheet resistance of $\simeq$ 0.67 kΩ/□. We measured the variation of resistance of the device with applied V_{bg} while keeping the top gate voltage $V_{tg} = 0V$. The resulting resistance curves are shown in figure 7.2(b), and here, different colours of the curves indicate the sweep direction. We see that the resistance of device BSH1 increases for negative gate voltages, which indicates the n-type nature of

our TINRs [85, 86]. At V_{bg} =-12V, the resistance of the device gets almost doubled in value compared to the zero voltage case. In figure 7.2(c), we plotted the resistance curve of the device for a small V_{bg} sweep range of -8V to -10V. Here, one can see some resistance oscillations, which are consistent in both forward and backward sweeps. This might be due to transversal quantization in the device seen in similar TI devices [131, 141]. The response of the device to V_{tg} with zero V_{bg} is shown in figure 7.2(d). Here, similar behaviour as in the case applied back gate alone. But since the top h-BN flake is thinner, with V_{tg} =-12V, the resistance of the device has gone up by a factor of roughly $\simeq$ 2.8. Also, we see that the sweep curve corresponding to the top gate shows some hysteresis. This might indicate shifts due to accumulated charges at the interfaces of the device.

In figure 7.2(e), we show the response in terms of the resistance map of device BSH1 in terms of V_{bg} and V_{tg}. As seen here, the resistance of the device increases sharply around high negative gate voltages and reaches a peak value of $\simeq$ 72 kΩ at V_{bg} = -17V and V_{tg} = -10V. This is approximately 15 times higher compared to the initial resistance of the device and corresponds to a sheet resistance of $\simeq$ 11.5 kΩ/□. We believe that, with such a sharp increase in the device resistance and high sheet resistance, we might be really close to the Dirac point of the device. Unfortunately, we could not apply even larger negative gate voltages to show a decrease of resistance after the Dirac point when the carrier types switch from electrons to holes. Nevertheless, a dual gate TINR device with h-BN dielectrics might be a way to study transport around the Dirac point in our devices.

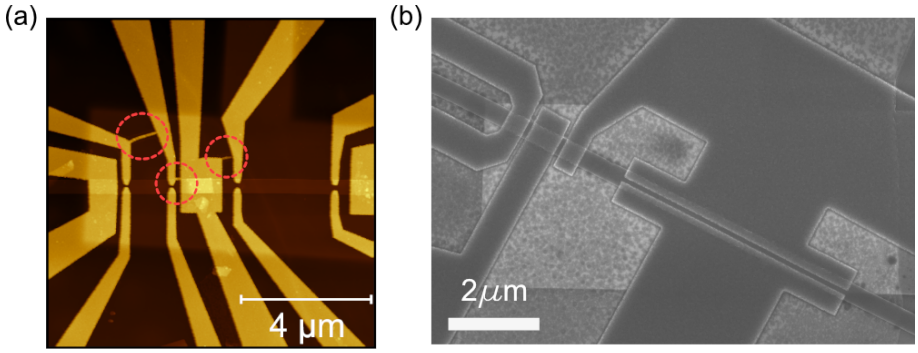

Figure 7.3: (a) AFM image of a TINR device fabricated on local gate/h-BN stack showing shorted electrode due to crack developed in the resist layer indicated with red circles. (b) SEM image of a test TINR device fabricated on local gate/h-BN stack with a modified recipe.

Although we tried to fabricate gate devices with h-BN dielectric for magneto-transport studies, due to the previously mentioned issue with AR-P e-beam resist due to strain, the electrodes often got shorted (see figure 7.3 (a)). With h-BN gated devices, the cracks in the resist become more prominent. This is because, during the baking process, the h-BN flake strains the resist layer due to the neg-

ative thermal expansion coefficient of h-BN [177], resulting in cracks in the resist layer. We later developed an improved e-beam lithography recipe that allows the fabrication of gated S-TI-S junctions using h-BN as dielectric. A test TINR device fabricated on an h-BN flake using this recipe is given in 7.3(b), not showing any evident cracks or short. Due to time constraints, we could not fabricate or measure any S-TI-S junction with h-BN as gate dielectric.

7.2 Reducing bulk contributions to transport in Bi_2Se_3 nanoribbons: use of ultra thin nanoribbons

In the previous section, we showed a large increase in sheet resistance of dual h-BN gated TINR device of thickness 65(70)nm, possibly approaching the Dirac point in the material. But in order to reduce carrier density in our nanoribbon and better tune them near the Dirac point, it is essential to use ultrathin TINRs (thickness below 15 nm). In fact, Kunakova et al. demonstrated ambipolar transport in a gated 9 nm thick Bi_2Se_3 nanoribbon device fabricated on STO substrate with high dielectric constant [86]. Ultrathin nanoribbons can be controlled easily with gate voltages compared to the thicker nanoribbons that we typically use in our devices. Our typical Bi_2S_3 growth process discussed in [84] has a lower yield for nanoribbons with thicknesses below 15 nm. So, our collaborators optimized the growth process to increase the yield of sub-15 nm TINRs, as discussed in [178].

Niherysh et al. carried out magnetotransport characterization of devices based on ultrathin Bi_2Se_3 nanoribbons grown using the modified growth process by Sondors et al. [178, 179]. The full description of this study is outside the scope of this thesis. From the observed SdH oscillations in these devices, we have an indication of TSSs being present in these devices, like our standard devices [85]. We looked at the gate dependence of the resistance of a device fabricated using TINRs from the new growth process. The device discussed here is referred to as Device 3 in [179], and the typical device layout used in the study is shown in figure 7.4(a). Device 3 is fabricated using an ultrathin Bi_2Se_3 nanoribbon with a width and thickness of 85 and 12 nm. The gate voltage is applied with Ti/Au contacts deposited on the backside of SiO_2(300nm)/Si substrates.

The resistance (R_{xx}) vs Gate voltage curve of Device 3 is given in figure 7.4(b). Like in the case of device BSH1 discussed above, we observe resistance oscillations with respect to gate voltage, which might originate from transversal momentum quantization in the TINR. Using a COMSOL simulation, the capacitance of the device was determined, and from this, one gets a change in carrier concentration of $\Delta n \simeq 1.5 \times 10^{12}$ cm^{-2}. This roughly corresponds to a change in the chemical potential of the bottom TSSs (interface with substrate) by $\Delta\mu \simeq 45$meV [179]. Now, in the case of transversal quantization in the device, the subband spacing is

given by $\Delta\mu^P = \hbar v_F/P$ where $P = 2(w+t)$ is the perimeter along the rectangular cross-section of the TINR (see Chapter 2 section 2.5.2 or Chapter 4 for more on transversal quantization). Assuming a typical $v_F = 5\times10^5$ ms^{-1}, one gets $\Delta\mu^P \simeq$ 9meV. So, in the applied gate voltage range, one expects roughly $\Delta\mu/\Delta\mu^P = 5$ peaks in the resistance oscillations. As seen in figure 7.4(b), there are roughly 5-6 resistance peaks in the measured data in both directions, which agrees with the expected periodicity of resistance oscillations due to transversal quantization.

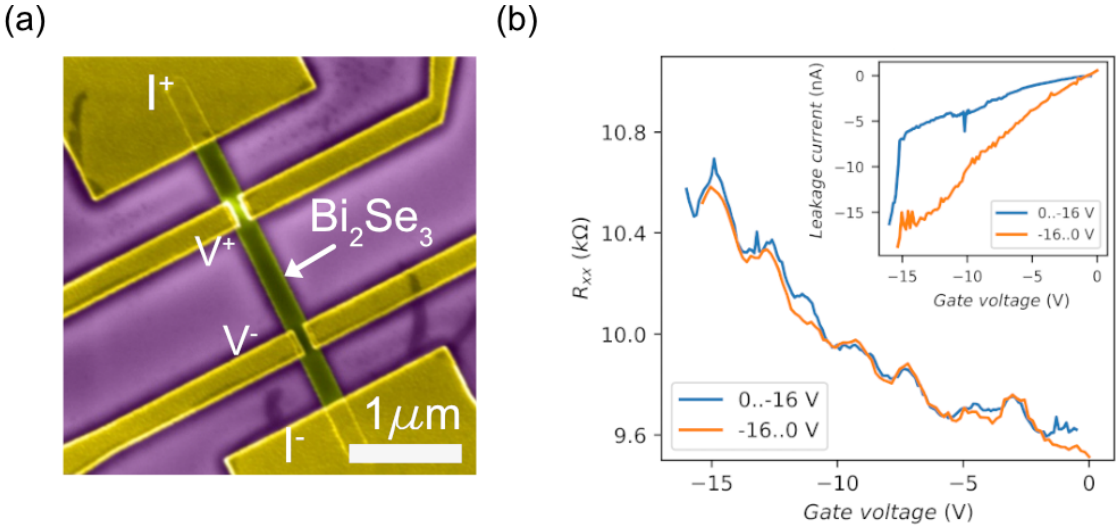

Figure 7.4: (a) SEM image showing typical device geometry used for magneto-transport measurements. The voltage and current probes used for the measurements discussed are indicated as V^+ (V^-) and I^+ (I^-), respectively (b) R_{xx} as a function of back-gate voltage for Device three from [179]. The blue and orange curves represent two different gate sweep directions. The inset shows the corresponding gate leakage current of the device (image adapted from [179]).

We have not fabricated any S-TI-S junction using these ultrathin Bi_2Se_3 nanoribbons from the new growth process. However, because of the thin nature of these nanoribbons, we expect to be able to tune the chemical potential close to the Dirac point with the help of top and bottom gates, and we might succeed in observing ambipolar transport in this case like Kunakova et al. [86].

7.3 Increased junction length for reducing diffusive contributions in Al-Bi_2Se_3-Al junctions

Most of the Al-Bi_2Se_3-Al junctions in this thesis had a length of less than 120nm. We used this design to ensure we are within the short junction limit to have a simpler description of Andreev bounds states in our junctions (see sections 2.3.3). Now, if we increase the length of the junctions further, then we should

see a reduction in the current contribution from the diffusive channel while the ballistic contributions remain the same. This is because for a diffusive junction, the critical current scales as roughly $1/l$ and $1/l^3$ in the short and long junction limits, respectively [180].

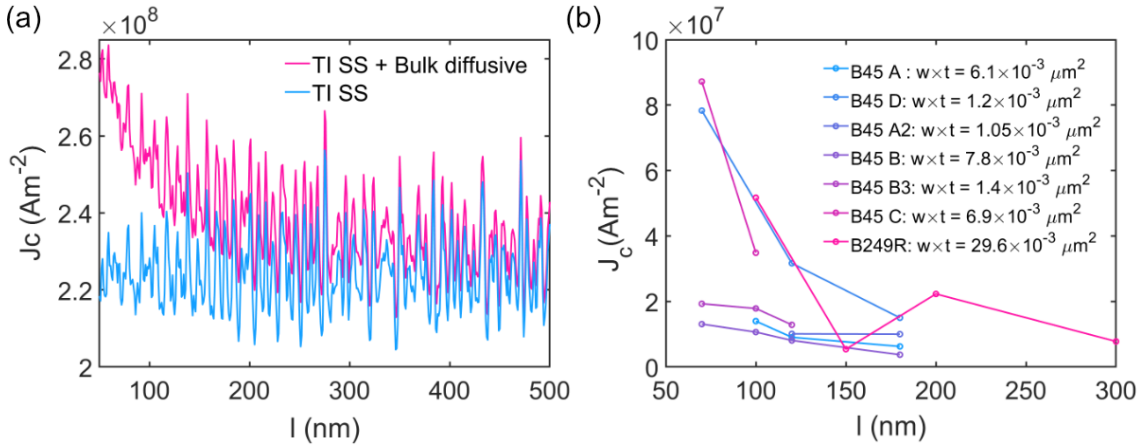

Figure 7.5: (a) Calculated J_c vs. l of a typical TI-junction of width 200 nm in the short junction limit. The blue line corresponds to the case in which surface states completely carry the supercurrent, and the magenta line corresponds to a case in which both ballistic TI-surface states and bulk diffusive states are involved in the transport. As seen here, for a junction with only TI-surface states, the J_c fluctuates around a constant value with increasing length. Whereas for a junction with both bulk and TI surface states contributing to transport, initially, the J_c drops with increasing length. This is because as L is increased, the resistance of the device increases, and the diffusive contribution to Jc decreases by approximately $1/l$. Above 200 nm, the current is carried mainly by surface states, and J_c fluctuates around the same value. (b) Measured J_c vs L curves for various TI-junctions. Each line corresponds to junctions fabricated on the same nanoribbon.

Using the same model for CPR in junction as described in Chapter 5, we calculated the critical current density J_c as a function of the junction length l for an S-TI-S junction of width 200 nm and typical junction parameters($k_F = 0.55$ nm$^{-}1$ and diffusive channel contributing 30% to the supercurrent) [142]. The calculated J_c of the device as a function of l is given in figure 7.5. As seen here, we see an initial drop in J_c as the length increases, and above 200 nm, the J_c saturates and starts to fluctuate around a constant value. This indicates that the current contribution, in this case, comes from the TSSs alone. From Chapter 4, we know that in our junction, we have Fabry-Pérot oscillations at a length scale over a micrometre. So, it might be possible to find a regime where the length of the device is such that the diffusive contribution to the current carried by the junction is minimal while the ballistic TSSs are still in the short junction regime. This could be explored more in the future. As a preliminary result, in Fig. **??**(b),

we have plotted the measured J_c vs. L curves for various devices we measured. Here, each line corresponds to the junctions fabricated on the same nanoribbon. As in the simple model described above, we see an initial drop in J_c followed by saturation of J_c above 150 nm. So, a junction with increased length (maybe even close to μm scale) is a potential way to reduce bulk contributions to transport, and this will be explored more in the future.

8 Summary and outlook

The growing interest in emulating Majorana fermions for topologically protected quantum computing architectures led us to study the properties of topological insulator-superconductor hybrid junctions.

In this thesis, we used Bi_2Se_3 in nanoribbon form to fabricate our junctions to have a higher surface-to-volume ratio, thereby reducing the unavoidable bulk contributions to transport. We explored in depth the size quantization effects and ballistic transport in Al-Bi_2Se_3-Al junctions by studying the width dependence of the critical current density and Fabry-Pérot resonances arising from ballistic topological surface states(TSSs). We observed a pronounced reduction of the Josephson critical current density J_c of our devices when the junction width is reduced. We showed that this phenomenology could be associated with the transport through the topological surface states. By geometric considerations, the Josephson current is mainly carried by modes propagating on the top surface. To provide further proof of transversal quantization effects in our devices, we looked at Fabry-Pérot(FP) resonance in our junction in both normal and superconducting states. We demonstrated FP resonances in Al-Bi_2Se_3-Al junctions with lateral dimensions up to 1.5 μm. Moreover, we observed FP oscillations in the Josephson current and excess current, which correlate with the normal state conductance oscillations as a function of applied gate voltage. These findings indicate quasi-ballistic transport of TSSs over micrometre length scales.

To study the DC transport properties of our junctions and provide indications of supercurrent being carried by TSSs we extract the current phase relation (CPR) of our Al-Bi_2Se_3-Al junctions using an asymmetric SQUID measurement technique. The CPRs are skewed, and the skewness values at very low temperatures were higher than the typical skewness expected from a short diffusive junction. This points towards the presence of high transmissive transport modes arising from TSSs in our device. However, by fitting the experimentally obtained CPR at 20 mK, we found that our junctions have both diffusive and ballistic transport modes contributing to Josephson transport. Yet, a major portion of the supercurrent is carried by ballistic TSSs. This was one of the crucial pieces of information we needed for analyzing our microwave measurements on Al-Bi_2Se_3-Al junctions.

We implemented Al-Bi_2Se_3-Al junctions in a circuit QED-inspired layout in the form of an RF-SQUID coupled to a CPW resonator to check the possibility of probing the Andreev bound states (ABSs) associated with these highly transmissive modes. Though we did not observe any avoided level crossing due to vacuum

Rabi-oscillations, we measured the ac susceptibility of our junctions. By scrutinizing the phase variation of the coupled system's resonance mode, we obtained critical insights into the dynamics of Andreev-bound states within the junction. Our measurements highlight the existence of bound states characterized by small energy gaps alongside relaxation rates surpassing 1 GHz. Through the examination of the temperature dependence of these rates, we attribute the microwave excitation/relaxation process to the interaction with an electronic continuum residing in the bulk (Possibly also TSSs) of the topological insulator. For future studies, it will be of paramount importance to reduce the bulk conductivity in order to probe bound states in the TSSs only.

The presence of both diffusive and ballistic transport modes in our junctions complicates the transport analysis in the junctions. Therefore, reducing transport modes, especially the diffusive contribution, is essential for experiments aimed at detecting MBSs using 3D-TI junctions. So, in the last section of the thesis, we discussed our attempts at reducing the bulk conductivity in our Bi_2Se_3 devices. Although we could not achieve any gating effects in the suspended junctions, we found that by using h-BN as dielectric and by gating the device from both the top and bottom side, we can increase the resistance of the device drastically, and we can get the chemical potential very close to the Dirac point. The effectiveness of this approach in controlling supercurrent transport in our Al-Bi_2Se_3-Al junction is yet to be tested. We also briefly discussed the possibility of using ultrathin nanoribbons for better gate control, thereby reducing bulk contributions to transport. We believe sub-15 nm devices might be better suited for transport studies close to the Dirac point. We also discussed the possibility of increasing the length of our S-TI-S junction to reduce bulk contributions to supercurrent in the junction.

Taking all the insight into account, for future studies, we are going to use ultra thin Bi_2Se_3 with gating capabilities to control the transport in the junctions and tune the Fermi level near the Dirac point to reduce bulk transport contributions. Also, the dependence on the critical current and the junction length must be studied to identify a regime where the diffusive channel contributes less to transport while the states from TSSs are still in short junction limit. Also, in situ deposited epitaxial superconductors might be essential to realize "hard" induced gaps in TIs. It might be good to study the nature of the induced superconducting gap in our junction to check for the presence of subgap states. Indeed, we have indications of a soft-induced gap causing excessive relaxation rates in the ABS dynamics. Due to the presence of transversal quantization in our devices, it is essential to apply a flux of 0.5 Φ_0^N (h/e) along the axis of the TINR in future experiments for observing MBSs in these junctions.

Finally, the whole field of condensed matter and the detection of Majorana fermions depends heavily on the quality of materials. For unambiguous detection of this elusive particle, it is essential to identify and develop better materials.

This is a major challenge that the community is presently facing and will require innovative solutions to improve the quality of the materials.

Appendices

Appendix A

Microwave measurements: various formulas

A.1 Resonator model

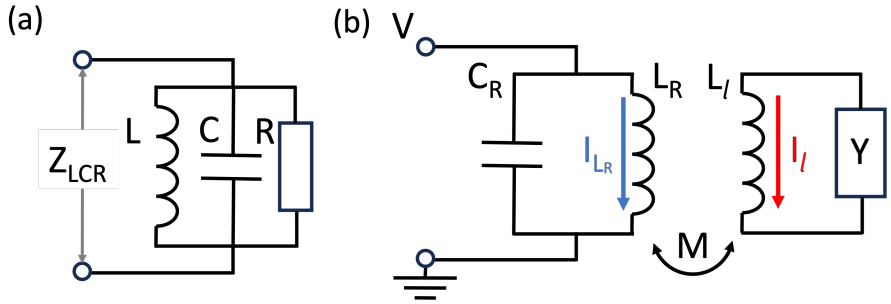

Figure A.1: (a) Parallel LCR circuit. (b) rf-SQUID coupled to an LC resonator through mutual inductance M.

A.1.1 Parallel LCR resonator impedance close to resonance frequency

The impedance of a parallel RLC resonator shown in Fig. A.1 (a) is given by:

$$Z_{LCR} = \left(\frac{1}{R} + \frac{1}{i\omega L} + i\omega C\right)^{-1}. \tag{A.1}$$

Expressing the impedance close to the resonance frequency using $\omega = \omega_0 + \delta\omega$ with $\omega_0 = 1/\sqrt{LC}$ and neglecting $\delta\omega^2/\omega_0^2$ terms we get:

$$\begin{aligned} Z_{LCR} &\simeq \left(\frac{1}{R} + \frac{i2\omega_0\delta\omega LC}{(\omega_0+\delta\omega)L}\right)^{-1}, \\ &\simeq \left(\frac{1}{R} + i2\delta\omega C\right)^{-1} \\ &= \left(\frac{1}{R} + i2\frac{\delta\omega}{\omega_0}\frac{1}{Z_0}\right)^{-1}, \end{aligned} \tag{A.2}$$

with $Z_0 = \sqrt{L/C}$ the characteristic impedance of the LC circuit.

A.1.2 RF-SQUID coupled to a lumped element LC circuit

In the following we consider an admittance, Y, shorted by a superconducting loop with inductance L_l, which is coupled via a mutual inductance, M, to the inductance of a parallel LC circuit (see Fig. A.1 (b)). For a fixed ac-voltage drive,V, we obtain the following two equations

$$\begin{aligned} V &= i\omega L_R I_{L_R} + i\omega M I_l, \\ 0 &= i\omega L_l I_l + \frac{I_l}{Y} + i\omega M I_{L_R}, \end{aligned} \tag{A.3}$$

with L_R the resonator inductance, I_{L_R} the ac current flowing through the resonator inductance, and I_l the ac current flowing through the loop inductance L_l. From the second equation in A.3, we obtain the expression for the loop current

$$I_l = -M\left(L_l + \frac{1}{i\omega Y}\right)^{-1} I_{L_R}. \tag{A.4}$$

We can therefore rewrite:

$$V = i\omega I_{L_R}\left[L_R - M^2\left(L_l + \frac{1}{i\omega Y}\right)^{-1}\right]. \tag{A.5}$$

Here we can define the load impedance Z_L in series with the resonator inductor as:

$$\begin{aligned} Z_L &= -i\omega M^2\left(L_l + \frac{1}{i\omega Y}\right)^{-1} \\ &= \frac{\omega^2 M^2}{i\omega L_l + 1/Y}. \end{aligned} \tag{A.6}$$

Using the expression of the Josephson admittance $Y = \chi/i\omega$ we obtain the load impedance

$$Z_L = -i\omega M^2 \frac{\chi}{1 + L_l \chi}. \tag{A.7}$$

For a small screening parameter, i.e. $\chi L_l \ll 1$ we get

$$Z_L = -i\omega M^2 \chi \tag{A.8}$$

In the following, we will discuss the effect of the load impedance on both the resonance frequency and quality factor of the coupled system. For this, we first consider the loaded impedance of the LC circuit (neglecting any intrinsic losses, i.e. the parallel resistor is set to infinity), which becomes:

$$\tilde{Z}_{LC} = \left(\frac{1}{i\omega L_R + Z_L} + i\omega C_R \right)^{-1}. \tag{A.9}$$

Rewriting this expression at frequencies close to the resonance frequency $\omega = \omega_0 + \delta\omega$, with $\omega_0 = 1/\sqrt{L_R C_R}$, and neglecting $\delta\omega^2/\omega_0^2$ terms we get:

$$\begin{aligned} \tilde{Z}_{LC} &\simeq \frac{i(1 + \frac{\delta\omega}{\omega_0})\omega_0 L_R + Z_L}{-2\frac{\delta\omega}{\omega_0} + i\frac{Z_L}{Z_0}\left(1 + \frac{\delta\omega}{\omega_0}\right)}, \\ &\simeq \frac{iZ_0 + Z_L}{-2\frac{\delta\omega}{\omega_0} + i\frac{Z_L}{Z_0}}. \end{aligned} \tag{A.10}$$

In the limit $Z_L \ll Z_0 = \sqrt{L_R/C_R}$ we get

$$\tilde{Z}_{LC} \simeq \frac{1}{\frac{Z_L}{Z_0^2} + 2i\frac{\delta\omega}{\omega_0}\frac{1}{Z_0}}. \tag{A.11}$$

Using the real and imaginary component of the load impedance $Z_L = \mathrm{Re}(Z_L) + \mathrm{Im}(Z_L)$ we arrive at the final expression

$$\tilde{Z}_{LC} \simeq \frac{1}{\frac{\mathrm{Re}(Z_L)}{Z_0^2} + \frac{i}{Z_0}\left(\frac{2\delta\omega}{\omega_0} + \frac{\mathrm{Im}(Z_L)}{Z_0}\right)}. \tag{A.12}$$

From this expression, we can derive the relative resonance frequency shift, $\delta\omega/\omega_0$, and the added losses, $\delta(1/Q)$ caused by the load impedance. The resonance condition is fulfilled for $\mathrm{Im}(1/\tilde{Z}_{LC}) = 0$, giving us the relative frequency change due to the load impedance

$$\frac{\delta\omega}{\omega_0} = -\frac{\mathrm{Im}(Z_L)}{2Z_0}. \tag{A.13}$$

Comparing expression A.12 with equation A.2 we can identify $Z_0^2/\operatorname{Re}(Z_L)$ as an effective resistor, R_{eff}, in parallel with the LC circuit (see Fig. A.1 (a)). Using the expression for the quality factor of a parallel LCR circuit we obtain for the losses added to the LC circuit:

$$\begin{aligned}\delta\left(\frac{1}{Q}\right) &\simeq (\omega_0 R_{eff} C)^{-1} \\ &= \frac{\operatorname{Re}(Z_L)}{Z_0}.\end{aligned} \tag{A.14}$$

Plugging the expression of the load impedance for small screening parameter, eq. A.8, into eqs. A.13 and A.14 we get:

$$\frac{\delta\omega}{\omega_0} = \frac{M^2}{2L_R}\chi' \tag{A.15}$$

$$\delta\left(\frac{1}{Q}\right) = \frac{M^2}{L_R}\chi'' \tag{A.16}$$

The above two equations are also valid in the case of a distributed element resonator such as a $\lambda/4$ resonator, with L_R replaced by $L_l l$ [156]. Here L_l and l are the inductance per unit length and the length of the $\lambda/4$ resonator, respectively.

In the limit where the screening parameter does not fulfill the condition $\chi L_l \ll 1$ we have to replace χ' with $\operatorname{Re}\left(\frac{\chi}{1+\chi L_l}\right)$ and χ'' with $\operatorname{Im}\left(\frac{\chi}{1+\chi L_l}\right)$ in eqs. A.15 and A.16, respectively.

A.2 Matrix elements of the Andreev current operator

The current operator of an Andreev system of a single mode with transmission coefficient τ_n written in the Andreev states basis is given by [61, 176, 181]:

$$\hat{I}_n = I_n(\varphi, \tau_n)\left(\sigma_z + \sqrt{1-\tau_n}\tan(\varphi/2)\sigma_x\right), \tag{A.17}$$

where the current $I_n(\varphi, \tau_n)$ is given by

$$I_n(\varphi, \tau_n) = \frac{2e}{\hbar}\frac{\partial E_n^+}{\partial\varphi} = \frac{e\Delta'}{2\hbar}\frac{\tau_n \sin(\varphi)}{\sqrt{1-\tau_n \sin^2(\varphi/2)}}, \tag{A.18}$$

with e the elementary charge, and $\hbar = h/2\pi$ the reduced Planck constant. σ_z and σ_x are the z- and x-Pauli matrices, respectively.

A.3 Estimation of resonator Andreev bound state coupling

The coupling Hamiltonian between the Andreev system and the resonator mediated by the mutual inductance M between the rf-SQUID and the resonator is given by [61]:

$$H_g = M\hat{I}_R\hat{I}_n, \tag{A.19}$$

with $\hat{I}_R$ the current operator of the resonator given by [61, 182]:

$$\hat{I}_R = \sqrt{\frac{\hbar\omega_n}{2L_l l}}(a^\dagger + a). \tag{A.20}$$

Here a and $a^\dagger$ are the annihilation and creation operators of the harmonic oscillator mode ω_n, respectively.

Combining eqs. A.17 and A.20 into eq. A.19 one obtains [61]:

$$H_g = g(a^\dagger + a)\left(\frac{1}{\sqrt{1-\tau}\tan(\varphi/2)}\sigma_z + \sigma_x\right) \tag{A.21}$$

The maximum coupling strength g at phase $\varphi = \pi$ between the LC resonator mode and the Andreev bound state pair mediated by the mutual inductance M can be approximated as [61]:

$$\hbar g \simeq M\sqrt{\frac{\hbar\omega_n}{2L_l l}}\frac{e\Delta'}{\hbar}. \tag{A.22}$$

For a mutual inductance of $3 - 10$ pH we should obtain $g/2\pi$ values between 1.3 MHz and 4.5 MHz for the 4.4 GHz resonator mode and 1.8 MHz and 6.1 MHz for the 8.16 GHz mode.

Appendix B

Fabrication recipes

Substrate cleaning

- Hot acetone (50°C) bath for 10 mins.
- If required, do an ultrasonic bath for 10 mins in acetone.
- IPA and blow dry with nitrogen gun.
- Check and repeat if necessary. If there are more residues or particles on the surface, consider using oxygen plasma and then doing the cleaning process from the beginning.
- For sapphire substrates, first using use a cotton swab to clean the surface while keeping it in an acetone bath.

Chip marks

- Clean the substrate or wafer.
- Spin MMA EL6 at 6000 rpm, bake at 130°C for 3 mins.
- Spin ARP 1:2 at 6000 rpm, bake at 130°C for 3 mins.
- If the substrate is sapphire, evaporate 20 nm Cr using Leasker Nano Cr.
- EBL with base dose 220 $\mu C/cm^2$.
- Development: 75 sec in Hexyl acetate and 75 sec in MIBK:IPA 1:3. After each step stop the development in IPA and blow dry before proceeding.
- Soft plasma at 25W for 10 sec.
- Evaporate Ti (10 nm) / Au (70 nm) / Pd (10 nm) in Lesker 1.
- Liftoff in hot acetone with gentle pipetting. IPA dip and then blow dry.

Al electrode for TI-junction or Au electrode other devices

- Spin MMA EL6 at 3000 rpm, bake at 130°C for 2 mins.
- Spin ARP 2:1 at 6000 rpm, bake at 130°C for 2 mins.
- If the substrate is sapphire, evaporate 20 nm Cr with Leasker Nano Cr.
- EBL with base dose 212 $\mu C/cm^2$ for low current and 300 $\mu C/cm^2$ for high current exposure.
- Development: 75 sec in Hexyl acetate and 75 sec in MIBK:IPA 1:3.After each step stop the development in IPA and blow dry before proceeding.
- Soft plasma at 25W for 10 sec.
- IBE etch for 35 sec, current 5mA, voltage 300 V, flow 4 sccm.
- Evaporate Pt (3 nm) / A1 (100 nm) in Lesker 1 (use recipes R1 Pt and R2 Al to keep the deposition rate 0.1 nm/s) for junction or desired metal for other devices. In case Au contact choose the desired deposition recipe.
- Liftoff in hot acetone with gentle pipetting. IPA dip and then blow dry.

Gate electrodes for suspended devices

Do not deposit any metal more than 40 nm to be safe. The resist layer is very thin.

- Spin MMA EL4 at 8000 rpm, bake at 170°C for 3 mins.
- Spin PMMA A2 at 5000 rpm, bake at 170°C for 3 mins.
- If the substrate is sapphire, evaporate 20 nm Cr with Leasker Nano Cr.
- EBL with base dose 1080 $\mu C/cm^2$.
- Development for 90 sec in MIBK:IPA 1:3 and stop the development in IPA and blow dry.
- Soft plasma at 25W for 5 sec.
- IBE etch for 35 sec, current 5mA, voltage 300 V, flow 4 sccm.
- Evaporate Ti (5 nm) / Au (25 nm) / Pd (5 nm) in Lesker 1.
- Liftoff in hot acetone with gentle pipetting. IPA dip and then blow dry.

Al_2O_3 pillars for suspended devices

- Spin MMA EL6 at 6000 rpm, bake at 170°C for 3 mins.
- Spin ARP 1:2 at 6000 rpm, bake at 170°C for 3 mins.
- If the substrate is sapphire, evaporate 20 nm Cr with Leasker Nano Cr.
- EBL with base dose 205 $\mu C/cm^2$.
- Development: 75 sec in n-amyl acetate and 75 sec in MIBK:IPA 1:3. After each step stop the development in IPA and blow dry before proceeding.
- Soft plasma at 25W for 10 sec.
- Evaporate Al2O3 (50 nm) in Lesker 2.
- Liftoff in hot acetone with gentle pipetting. IPA dip and then blow dry.

Trilayer recipe for devices on h-BN

Used for avoiding cracking problems associated with ARP and still do closely spaced patterns for junctions down to 50 nm.

- Spin MMA EL6 at 3000 rpm, acc 1000 for 60s, and bake at 130°C for 2 mins
- Spin ARP 1:2 at 6000 rpm, acc 1000 for 60s and bake at 130°C for 2 mins
- Spin PMMA A3 at 6000 rpm, acc 1000 for 60s and bake at 130°C for 2 mins
- Spin Espacer at 2800 rpm, acc 1000 for 60s and blow dry or ambient dry if needed.
- EBL with base dose 240 $\mu C/cm^2$ for low current patterns and 350 $\mu C/cm^2$ for high current patterns.
- Remove the top Espacer layer by dipping in H_2O for 30 sec and blow dry.
- Develop for 60 sec in H_2O:IPA 7:93 (premixed-bottle, shake the bottle to mix before using). Stop development using IPA for 5 sec and blow dry.
- Develop for 60 sec in n-amylacetate for 60 sec. Stop development using IPA for 5 sec and blow dry.
- Develop for 60 sec in MIBK:IPA 1:3 (premixed-bottle) for 60 sec. Stop development using IPA for 5 sec and blow dry.
- Soft plasma at 25W for a maximum of 15 sec using batch top.

- IBE etch for 35 sec, current 5mA, voltage 300 V, flow 4 sccm.
- Evaporate metal of choice
- Heat up acetone at 500°C and lift off for 10 mins with gentle pipetting. Dip in IPA for 30sec and blow dry.

NbN resonator

PMMA gets easily etched with Ar-Cl ecthing and one has to play close attention during etching process.

- Deposit 100nm NbN film using DCA in a 2-inch substrate.
- Dice into required chip sizes.
- Clean the chips gently after dicing to remove any residues.
- Spin PMMA A6 at 4000 rpm, acc 1000 for 60s, and bake at 170°C for 3 mins.
- EBL with base dose 700 $\mu C/cm^2$.
- Develop for 90 sec in H_2O:IPA7:93 (premixed-bottle, shake the bottle to mix before using). Stop development using IPA for 5 sec and blow dry.
- Soft plasma at 25W for a maximum of 15 sec using batch top.
- RIE Ar 50 sccm Cl 4 sccm for around 20 seconds. You use the laser for end detection.
- Rinse in H_2O and examine the chips to check for quality.

References

[1] P. A. M. Dirac, "The Quantum Theory of Electron", Proc. R. Soc. Lond. A **117**, 610–624 (1928).

[2] C. D. Anderson, "The Positive Electron", Phys. Rev. **43**, 491–494 (1933).

[3] E. Majorana, "A symmetric theory of electrons and positrons", Scientific Papers of Ettore Majorana: A New Expanded Edition, 113–128 (2020).

[4] F. Wilczek, "Majorana returns", Nature Physics **5**, 614–618 (2009).

[5] A.Yu. Kitaev, "Fault-tolerant quantum computation by anyons", Ann. Phys. (N. Y). **303**, 2–30 (2002).

[6] C. Nayak, S. H. Simon, A. Stern, M. Freedman, and S. Das Sarma, "Non-Abelian anyons and topological quantum computation", Rev. Mod. Phys. **80**, 1083–1159 (2008).

[7] S. D. Sarma, M. Freedman, and C. Nayak, "Majorana zero modes and topological quantum computation", npj Quantum Inf. **1** (2015).

[8] M. Z. Hasan and C. L. Kane, "Colloquium: Topological insulators", Rev. Mod. Phys. **82**, 3045–3067 (2010).

[9] L. Fu and C. L. Kane, "Josephson current and noise at a superconductor/quantum-spin-Hall- insulator/superconductor junction", Phys. Rev. B - Condens. Matter Mater. Phys. **79**, 1–4 (2009).

[10] G. Tkachov, "Chiral current-phase relation of topological Josephson junctions: A signature of the 4π -periodic Josephson effect", Phys. Rev. B **100**, 1–8 (2019).

[11] J. Alicea, "New directions in the pursuit of Majorana fermions in solid state systems", Reports on progress in physics **75**, 1–36 (2012).

[12] R. M. Lutchyn, J. D. Sau, and S. Das Sarma, "Majorana fermions and a topological phase transition in semiconductor-superconductor heterostructures", Phys. Rev. Lett. **105**, 1–4 (2010).

[13] V. Mourik, K. Zuo, S. M. Frolov, S. R. Plissard, E. P. Bakkers, and L. P. Kouwenhoven, "Signatures of majorana fermions in hybrid superconductor-semiconductor nanowire devices", Science (80-.). **336**, 1003–1007 (2012).

[14] J. R. Williams, A. J. Bestwick, P. Gallagher, S. S. Hong, Y. Cui, A. S. Bleich, J. G. Analytis, I. R. Fisher, and D. Goldhaber-Gordon, "Unconventional Josephson effect in hybrid superconductor-topological insulator devices", Phys. Rev. Lett. **109**, 1–5 (2012).

[15] S. Cho, B. Dellabetta, A. Yang, J. Schneeloch, Z. Xu, T. Valla, G. Gu, M. J. Gilbert, and N. Mason, "Symmetry protected Josephson supercurrents in three-dimensional topological insulators", Nat. Commun. **4**, 1–6 (2013).

[16] L. Galletti, S. Charpentier, M. Iavarone, P. Lucignano, D. Massarotti, R. Arpaia, Y. Suzuki, K. Kadowaki, T. Bauch, A. Tagliacozzo, F. Tafuri, and F. Lombardi, "Influence of topological edge states on the properties of Al/Bi_2Se_3/Al hybrid Josephson devices", Phys. Rev. B - Condens. Matter Mater. Phys. **89**, 1–9 (2014).

[17] C. Kurter, A. D. Finck, Y. S. Hor, and D. J. Van Harlingen, "Evidence for an anomalous current-phase relation in topological insulator Josephson junctions", Nat. Commun. **6**, 2–7 (2015).

[18] I. Sochnikov, L. Maier, C. A. Watson, J. R. Kirtley, C. Gould, G. Tkachov, E. M. Hankiewicz, C. Brüne, H. Buhmann, L. W. Molenkamp, and K. A. Moler, "Nonsinusoidal current-phase relationship in josephson junctions from the 3D topological insulator HgTe", Phys. Rev. Lett. **114**, 1–6 (2015).

[19] J. Wiedenmann, E. Bocquillon, R. S. Deacon, S. Hartinger, O. Herrmann, T. M. Klapwijk, L. Maier, C. Ames, C. Brüne, C. Gould, A. Oiwa, K. Ishibashi, S. Tarucha, H. Buhmann, and L. W. Molenkamp, "4π-periodic Josephson supercurrent in HgTe-based topological Josephson junctions", Nat. Commun. **7**, 1–7 (2016).

[20] E. Bocquillon, R. S. Deacon, J. Wiedenmann, P. Leubner, T. M. Klapwijk, C. Brüne, K. Ishibashi, H. Buhmann, and L. W. Molenkamp, "Gapless Andreev bound states in the quantum spin Hall insulator HgTe", Nat. Nanotechnol. **12**, 137–143 (2017).

[21] C. Li, J. C. de Boer, B. de Ronde, S. V. Ramankutty, E. van Heumen, Y. Huang, A. de Visser, A. A. Golubov, M. S. Golden, and A. Brinkman, "4π-periodic Andreev bound states in a Dirac semimetal", Nat. Mater. **17**, 875–880 (2018).

[22] G. Kunakova, T. Bauch, E. Trabaldo, J. Andzane, D. Erts, and F. Lombardi, "High transparency Bi_2Se_3 topological insulator nanoribbon Josephson junctions with low resistive noise properties", Appl. Phys. Lett. **115** (2019).

[23] K. Le Calvez, L. Veyrat, F. Gay, P. Plaindoux, C. B. Winkelmann, H. Courtois, and B. Sacépé, "Joule overheating poisons the fractional ac Josephson effect in topological Josephson junctions", Communications Physics **2**, 1–9 (2019).

[24] H. Ren, F. Pientka, S. Hart, A. T. Pierce, M. Kosowsky, L. Lunczer, R. Schlereth, B. Scharf, E. M. Hankiewicz, L. W. Molenkamp, B. I. Halperin, and A. Yacoby, "Topological superconductivity in a phase-controlled Josephson junction", Nature **569**, 93–98 (2019).

[25] P. Schüffelgen et al., "Selective area growth and stencil lithography for in situ fabricated quantum devices", Nat. Nanotechnol. **14**, 825–831 (2019).

[26] M. Kayyalha, M. Kargarian, A. Kazakov, I. Miotkowski, V. M. Galitski, V. M. Yakovenko, L. P. Rokhinson, and Y. P. Chen, "Anomalous Low-Temperature Enhancement of Supercurrent in Topological-Insulator Nanoribbon Josephson Junctions: Evidence for Low-Energy Andreev Bound States", Phys. Rev. Lett. **122**, 47003 (2019).

[27] M. Kayyalha, A. Kazakov, I. Miotkowski, S. Khlebnikov, L. P. Rokhinson, and Y. P. Chen, "Highly skewed current-phase relation in superconductor-topological insulator-superconductor Josephson junctions", npj Quantum Materials **5**, 1–7 (2020).

[28] G. Kunakova, **A. P. Surendran**, D. Montemurro, M. Salvato, D. Golubev, J. Andzane, D. Erts, T. Bauch, and F. Lombardi, "Topological insulator nanoribbon Josephson junctions: Evidence for size effects in transport properties", Journal of Applied Physics **128**, 194304 (2020).

[29] B. De Ronde, C. Li, Y. Huang, and A. Brinkman, "Induced topological superconductivity in a $BiSbTeSe_2$-based Josephson junction", Nanomaterials **10**, 1–9 (2020).

[30] V. S. Stolyarov, D. S. Yakovlev, S. N. Kozlov, O. V. Skryabina, D. S. Lvov, A. I. Gumarov, O. V. Emelyanova, P. S. Dzhumaev, I. V. Shchetinin, R. A. Hovhannisyan, S. V. Egorov, A. M. Kokotin, W. V. Pogosov, V. V. Ryazanov, M. Y. Kupriyanov, A. A. Golubov, and D. Roditchev, "Josephson current mediated by ballistic topological states in $Bi_2Te_2.3Se_0.7$ single nanocrystals", Commun. Mater. **1**, 1–11 (2020).

[31] N. H. Kim, H. S. Kim, Y. Hou, D. Yu, and Y. J. Doh, "Superconducting quantum interference devices made of Sb-doped Bi_2Se_3 topological insulator nanoribbons", Curr. Appl. Phys. **20**, 680–685 (2020).

[32] D. Rosenbach, T. W. Schmitt, P. Schüffelgen, M. P. Stehno, C. Li, M. Schleenvoigt, A. R. Jalil, G. Mussler, E. Neumann, S. Trellenkamp, A. A. Golubov, A. Brinkman, D. Grützmacher, and T. Schäpers, "Reappearance of first Shapiro step in narrow topological Josephson junctions", Sci. Adv. **7** (2021).

[33] M. Bai, X. K. Wei, J. Feng, M. Luysberg, A. Bliesener, G. Lippertz, A. Uday, A. A. Taskin, J. Mayer, and Y. Ando, "Proximity-induced superconductivity in (Bi1-xSbx)2Te3 topological-insulator nanowires", Commun. Mater. **3**, 1–7 (2022).

[34] T. W. Schmitt, M. R. Connolly, M. Schleenvoigt, C. Liu, O. Kennedy, J. M. Chávez-Garcia, A. R. Jalil, B. Bennemann, S. Trellenkamp, F. Lentz, E. Neumann, T. Lindström, S. E. De Graaf, E. Berenschot, N. Tas, G. Mussler, K. D. Petersson, D. Grützmacher, and P. Schüffelgen, "Integration of Topological Insulator Josephson Junctions in Superconducting Qubit Circuits", Nano Lett. **22**, 2595–2602 (2022).

[35] R. Fischer, J. Picó-Cortés, W. Himmler, G. Platero, M. Grifoni, D. A. Kozlov, N. N. Mikhailov, S. A. Dvoretsky, C. Strunk, and D. Weiss, "4P -Periodic Supercurrent Tuned By an Axial Magnetic Flux in Topological Insulator Nanowires", Phys. Rev. Res. **4**, 1–9 (2022).

[36] D. Kong, J. J. Cha, K. Lai, H. Peng, J. G. Analytis, S. Meister, Y. Chen, H. J. Zhang, I. R. Fisher, Z. X. Shen, and Y. Cui, "Rapid surface oxidation as a source of surface degradation factor for Bi_2Se_3", ACS Nano **5**, 4698–4703 (2011).

[37] H. K. Onnes, Leiden Communication **120b** (1911).

[38] D. van Delft and P. Kes, "The discovery of superconductivity", Physics Today **63**, 38–43 (2010).

[39] R. de Bruyn Ouboter, "Heike Kamerlingh Onnes's Discovery of Superconductivity", Scientific American **276**, 98–103 (1997).

[40] W. Meissner and R. Ochsenfeld, Naturwissenschaften **21**, 787–788 (1933).

[41] A. M. Forrest, "Meissner and Ochsenfeld revisited", European Journal of Physics **4**, 117 (1983).

[42] M. Tinkham, *Introduction to Superconductivity*, 2nd ed. (Dover Publications, 2004).

[43] J. Bardeen, L. N. Cooper, and J. R. Schrieffer, "Theory of Superconductivity", Phys. Rev. **108**, 1175–1204 (1957).

[44] I. Giaever, "Electron Tunneling Between Two Superconductors", Phys. Rev. Lett. **5**, 464–466 (1960).

[45] P. H. Smith, S. Shapiro, J. L. Miles, and J. Nicol, "Superconducting Characteristics of Superimposed Metal Films", Phys. Rev. Lett. **6**, 686–688 (1961).

[46] B. D. Josephson, "Possible new effects in superconductive tunnelling", Physics Letters **1**, 251–253 (1962).

[47] B. D. Josephson, "Coupled Superconductors", Rev. Mod. Phys. **36**, 216–220 (1964).

[48] P. W. Anderson and J. M. Rowell, "Probable Observation of the Josephson Superconducting Tunneling Effect", Phys. Rev. Lett. **10**, 230–232 (1963).

[49] T. Van Duzer and C. Turner, *Principles of Superconductive Devices and Circuits*, Bibliyografya Ve Indeks (Prentice Hall, 1999).

[50] S. Shapiro, "Josephson Currents in Superconducting Tunneling: The Effect of Microwaves and Other Observations", Phys. Rev. Lett. **11**, 80–82 (1963).

[51] P. A. Rosenthal, M. R. Beasley, K. Char, M. S. Colclough, and G. Zaharchuk, "Flux focusing effects in planar thin-film grain-boundary Josephson junctions", Applied Physics Letters **59**, 3482–3484 (1991).

[52] J. Clarke and A. Braginski, *The SQUID Handbook: Fundamentals and Technology of SQUIDs and SQUID Systems* (Wiley, 2006).

[53] W. Tsang and T. Van Duzer, "Dc analysis of parallel arrays of two and three Josephson junctions", Journal of Applied Physics **46**, 4573–4580 (2008).

[54] A. Andreev, "Thermal Conductivity of the Intermediate State of Superconductors", JETP Letters **46**, 1823–1828 (1964).

[55] G. E. Blonder, M. Tinkham, and T. M. Klapwijk, "Transition from metallic to tunneling regimes in superconducting microconstrictions: Excess current, charge imbalance, and supercurrent conversion", Phys. Rev. B **25**, 4515–4532 (1982).

[56] T. Klapwijk, G. Blonder, and M. Tinkham, "Explanation of subharmonic energy gap structure in superconducting contacts", Physica B+C **109-110**, 16th International Conference on Low Temperature Physics, Part 3, 1657–1664 (1982).

[57] M. Octavio, M. Tinkham, G. E. Blonder, and T. M. Klapwijk, "Subharmonic energy-gap structure in superconducting constrictions", Phys. Rev. B **27**, 6739–6746 (1983).

[58] M. Kjaergaard, H. J. Suominen, M. P. Nowak, A. R. Akhmerov, J. Shabani, C. J. Palmstrøm, F. Nichele, and C. M. Marcus, "Transparent Semiconductor-Superconductor Interface and Induced Gap in an Epitaxial Heterostructure Josephson Junction", Phys. Rev. Appl. **7**, 034029 (2017).

[59] C. W. J. Beenakker, "Universal Limit of Critical-Current Fluctuations in Mesoscopic Josephson Junctions", Phys. Rev. Lett. **67**, 3836–3839 (1991).

[60] P. F. Bagwell, "Suppression of the Josephson current through a narrow, mesoscopic, semiconductor channel by a single impurity", Phys. Rev. B **46**, 12573–12586 (1992).

[61] C. Janvier and L. Tosi and L. Bretheau and C. O. Girit and M. Stern and P. Bertet and P. Joyez and D. Vion and D. Esteve and M. F. Goffman and H. Pothier and C. Urbina, "Coherent manipulation of Andreev states in superconducting atomic contacts", Science **349**, 1199–1202 (2015).

[62] R. Haller, "Probing the microwave response of novel Josephson elements", PhD thesis (University of Basel, 2021).

[63] M. C. Janvier, "Coherent manipulation of Andreev bound states in a superconducting atomic contact", PhD thesis (Universite Paris-Saclay, 2016).

[64] V. Ambegaokar and A. Baratoff, "Tunneling Between Superconductors", Phys. Rev. Lett. **10**, 486–489 (1963).

[65] F. Kos, S. E. Nigg, and L. I. Glazman, "Frequency-dependent admittance of a short superconducting weak link", Phys. Rev. B - Condens. Matter Mater. Phys. **87**, 1–10 (2013), eprint: 1303.2918.

[66] C. Kane, "Chapter 1 - Topological Band Theory and the Z2 Invariant", in *Topological Insulators*, Vol. 6, edited by M. Franz and L. Molenkamp, Contemporary Concepts of Condensed Matter Science (Elsevier, 2013), pp. 3–34.

[67] M. Nakahara, *Geometry, topology and physics* (CRC press, 2018).

[68] M. V. Berry, "Quantal phase factors accompanying adiabatic changes", Proceedings of the Royal Society of London. A. Mathematical and Physical Sciences **392**, 45–57 (1984).

[69] D. Xiao, M.-C. Chang, and Q. Niu, "Berry phase effects on electronic properties", Rev. Mod. Phys. **82**, 1959–2007 (2010).

[70] K. v. Klitzing, G. Dorda, and M. Pepper, "New Method for High-Accuracy Determination of the Fine-Structure Constant Based on Quantized Hall Resistance", Phys. Rev. Lett. **45**, 494–497 (1980).

[71] D. Tong, "Lectures on the quantum Hall effect", arXiv preprint arXiv:1606.06687 (2016).

[72] K. von Klitzing, T. Chakraborty, P. Kim, V. Madhavan, X. Dai, J. McIver, Y. Tokura, L. Savary, D. Smirnova, A. M. Rey, et al., "40 years of the quantum Hall effect", Nature Reviews Physics **2**, 397–401 (2020).

[73] D. J. Thouless, M. Kohmoto, M. P. Nightingale, and M. den Nijs, "Quantized Hall Conductance in a Two-Dimensional Periodic Potential", Phys. Rev. Lett. **49**, 405–408 (1982).

[74] L. Fu and C. L. Kane, "Topological insulators with inversion symmetry", Phys. Rev. B **76**, 045302 (2007).

[75] A. Bansil, H. Lin, and T. Das, "Colloquium: Topological band theory", Rev. Mod. Phys. **88**, 021004 (2016).

[76] J. E. Moore and L. Balents, "Topological invariants of time-reversal-invariant band structures", Phys. Rev. B **75**, 121306 (2007).

[77] C. L. Kane and E. J. Mele, "Z_2 Topological Order and the Quantum Spin Hall Effect", Phys. Rev. Lett. **95**, 146802 (2005).

[78] Markus König and Steffen Wiedmann and Christoph Brüne and Andreas Roth and Hartmut Buhmann and Laurens W. Molenkamp and Xiao-Liang Qi and Shou-Cheng Zhang, "Quantum Spin Hall Insulator State in HgTe Quantum Wells", Science **318**, 766–770 (2007).

[79] B. A. Bernevig, T. L. Hughes, and S.-C. Zhang, "Quantum spin Hall effect and topological phase transition in HgTe quantum wells", science **314**, 1757–1761 (2006).

[80] Y. L. Chen, J.-H. Chu, J. G. Analytis, Z. K. Liu, K. Igarashi, H.-H. Kuo, X. L. Qi, S. K. Mo, R. G. Moore, D. H. Lu, M. Hashimoto, T. Sasagawa, S. C. Zhang, I. R. Fisher, Z. Hussain, and Z. X. Shen, "Massive Dirac Fermion on the Surface of a Magnetically Doped Topological Insulator", Science **329**, 659–662 (2010).

[81] L. Fu, C. L. Kane, and E. J. Mele, "Topological Insulators in Three Dimensions", Phys. Rev. Lett. **98**, 106803 (2007).

[82] H. Zhang, C.-X. Liu, X.-L. Qi, X. Dai, Z. Fang, and S.-C. Zhang, "Topological insulators in Bi_2Se_3, Bi_2Te_3 and Sb_2Te_3 with a single Dirac cone on the surface", Nature physics **5**, 438–442 (2009).

[83] S.-Q. Shen, "Three-Dimensional Topological Insulators", in *Topological Insulators: Dirac Equation in Condensed Matter* (Springer Singapore, Singapore, 2017), pp. 125–152.

[84] J. Andzane, G. Kunakova, S. Charpentier, V. Hrkac, L. Kienle, M. Baitimirova, T. Bauch, F. Lombardi, and D. Erts, "Catalyst-free vapour-solid technique for deposition of Bi_2Te_3 and Bi_2Se_3 nanowires/nanobelts with topological insulator properties", Nanoscale **7**, 15935–15944 (2015).

[85] G. Kunakova, L. Galletti, S. Charpentier, J. Andzane, D. Erts, F. Léonard, C. D. Spataru, T. Bauch, and F. Lombardi, "Bulk-free topological insulator Bi_2Se_3 nanoribbons with magnetotransport signatures of Dirac surface states", Nanoscale **10**, 19595–19602 (2018).

[86] G. Kunakova, T. Bauch, X. Palermo, M. Salvato, J. Andzane, D. Erts, and F. Lombardi, "High-Mobility Ambipolar Magnetotransport in Topological Insulator Bi2Se3 Nanoribbons", Physical Review Applied **16**, 1 (2021).

[87] L. Fu and C. L. Kane, "Superconducting Proximity Effect and Majorana Fermions at the Surface of a Topological Insulator", Phys. Rev. Lett. **100**, 096407 (2008).

[88] M. Leijnse and K. Flensberg, "Introduction to topological superconductivity and Majorana fermions", Semiconductor Science and Technology **27**, 124003 (2012).

[89] X.-L. Qi and S.-C. Zhang, "Topological insulators and superconductors", Rev. Mod. Phys. **83**, 1057–1110 (2011).

[90] S. Das Sarma, C. Nayak, and S. Tewari, "Proposal to stabilize and detect half-quantum vortices in strontium ruthenate thin films: Non-Abelian braiding statistics of vortices in a $p_x + ip_y$ superconductor", Phys. Rev. B **73**, 220502 (2006).

[91] A. M. Cook, M. M. Vazifeh, and M. Franz, "Stability of Majorana fermions in proximity-coupled topological insulator nanowires", Phys. Rev. B **86**, 155431 (2012).

[92] M. Snelder, M. Veldhorst, A. A. Golubov, and A. Brinkman, "Andreev bound states and current-phase relations in three-dimensional topological insulators", Phys. Rev. B - Condens. Matter Mater. Phys. **87**, 1–7 (2013).

[93] D. M. Badiane, L. I. Glazman, M. Houzet, and J. S. Meyer, "Ac Josephson effect in topological Josephson junctions", Comptes Rendus Physique **14**, Topological insulators / Isolants topologiques, 840–856 (2013).

[94] D. M. Badiane, M. Houzet, and J. S. Meyer, "Nonequilibrium Josephson effect through helical edge states", Phys. Rev. Lett. **107**, 1–5 (2011).

[95] W. Liang, M. Bockrath, D. Bozovic, and J. H. Hafner, "Fabry-Perot interference in a nanotube electron waveguide", Nature **411**, 665–669 (2001).

[96] "Phase-Coherent Transport in Graphene Quantum Billiards", Science **317**, 1530–1533 (2007).

[97] A. V. Kretinin, R. Popovitz-Biro, D. Mahalu, and H. Shtrikman, "Multimode Fabry-Pérot conductance oscillations in suspended stacking-faults-free InAs nanowires", Nano Letters **10**, 3439–3445 (2010).

[98] A. F. Young and P. Kim, "Quantum interference and Klein tunnelling in graphene heterojunctions", Nature Physics **5**, 222–226 (2009).

[99] A. L. Grushina, D. K. Ki, and A. F. Morpurgo, Applied Physics Letters **102**, 223102 (2013).

[100] P. Rickhaus, R. Maurand, M. H. Liu, M. Weiss, K. Richter, and C. Schönenberger, "Ballistic interferences in suspended graphene", Nature Communications **4**, 1–6 (2013).

[101] A. Varlet, M.-H. Liu, V. Krueckl, D. Bischoff, P. Simonet, K. Watanabe, T. Taniguchi, K. Richter, K. Ensslin, and T. Ihn, "Fabry-Pérot Interference in Gapped Bilayer Graphene with Broken Anti-Klein Tunneling", Phys. Rev. Lett. **113**, 116601 (2014).

[102] P. Rickhaus, P. Makk, M. H. Liu, E. Tóvári, M. Weiss, R. Maurand, K. Richter, and C. Schönenberger, "Snake trajectories in ultraclean graphene p-n junctions", Nature Communications **6**, 1–6 (2015).

[103] P. Pandey, R. Kraft, R. Krupke, D. Beckmann, and R. Danneau, "Andreev reflection in ballistic normal metal/graphene/superconductor junctions", Physical Review B **100**, 165416 (2019).

[104] M. I. Katsnelson, K. S. Novoselov, and A. K. Geim, "Chiral tunnelling and the Klein paradox in graphene", Nature Physics **2**, 620–625 (2006).

[105] M. Titov and C. W. Beenakker, "Josephson effect in ballistic graphene", Phys. Rev. B - Condens. Matter Mater. Phys. **74**, 1–4 (2006).

[106] D. Golubev, T. Bauch, and F. Lombardi, "Josephson Effect in Graphene and 3D Topological Insulators", in *Fundamentals and Frontiers of the Josephson Effect*, edited by F. Tafuri (Springer International Publishing, Cham, 2019), pp. 529–553.

[107] J. H. Bardarson, P. W. Brouwer, and J. E. Moore, "Aharonov-Bohm Oscillations in Disordered Topological Insulator Nanowires", Phys. Rev. Lett. **105**, 156803 (2010).

[108] L. A. Jauregui, M. T. Pettes, L. P. Rokhinson, L. Shi, and Y. P. Chen, "Magnetic field-induced helical mode and topological transitions in a topological insulator nanoribbon", Nature nanotechnology **11**, 345–351 (2016).

[109] A. Murani, A. Kasumov, S. Sengupta, Y. A. Kasumov, V. T. Volkov, I. I. Khodos, F. Brisset, R. Delagrange, A. Chepelianskii, R. Deblock, H. Bouchiat, and S. Guéron, "Ballistic edge states in Bismuth nanowires revealed by SQUID interferometry", Nat. Commun. **8**, 1–7 (2017).

[110] A. Assouline, C. Feuillet-Palma, N. Bergeal, T. Zhang, A. Mottaghizadeh, A. Zimmers, E. Lhuillier, M. Eddrie, P. Atkinson, M. Aprili, and H. Aubin, "Spin-Orbit induced phase-shift in Bi 2 Se 3 Josephson junctions", Nat. Commun. **10** (2019).

[111] F. Domínguez, O. Kashuba, E. Bocquillon, J. Wiedenmann, R. S. Deacon, T. M. Klapwijk, G. Platero, L. W. Molenkamp, B. Trauzettel, and E. M. Hankiewicz, "Josephson junction dynamics in the presence of 2π - And 4π -periodic supercurrents", Phys. Rev. B **95**, 1–9 (2017).

[112] S. Ghatak, O. Breunig, F. Yang, Z. Wang, A. A. Taskin, and Y. Ando, "Anomalous Fraunhofer Patterns in Gated Josephson Junctions Based on the Bulk-Insulating Topological Insulator $BiSbTeSe_2$", Nano Lett. **18**, 5124–5131 (2018).

[113] A. Q. Chen, M. J. Park, S. T. Gill, Y. Xiao, D. Reig-i Plessis, G. J. MacDougall, M. J. Gilbert, and N. Mason, "Finite momentum Cooper pairing in three-dimensional topological insulator Josephson junctions", Nat. Commun. **9**, 1–9 (2018).

[114] A. Kononov, G. Abulizi, K. Qu, J. Yan, J. Yan, D. Mandrus, D. Mandrus, K. Watanabe, T. Taniguchi, C. Schönenberger, and C. Schönenberger, "One-Dimensional Edge Transport in Few-Layer WTe_2", Nano Lett. **20**, 4228–4233 (2020).

[115] A. Murani, B. Dassonneville, A. Kasumov, J. Basset, M. Ferrier, R. Deblock, S. Guéron, and H. Bouchiat, "Microwave Signature of Topological Andreev level Crossings in a Bismuth-based Josephson Junction", Phys. Rev. Lett. **122**, 1–6 (2019).

[116] R. S. Deacon, J. Wiedenmann, E. Bocquillon, F. Domínguez, T. M. Klapwijk, P. Leubner, C. Brüne, E. M. Hankiewicz, S. Tarucha, K. Ishibashi, H. Buhmann, and L. W. Molenkamp, "Josephson Radiation from Gapless Andreev Bound States in HgTe-Based Topological Junctions", Phys. Rev. X **7**, 021011 (2017).

[117] H. J. Kwon, K. Sengupta, and V. M. Yakovenko, "Fractional ac Josephson effect in p- and d-wave superconductors", Eur. Phys. J. B **37**, 349–361 (2004).

[118] J. Park, Y.-B. Choi, G.-H. Lee, and H.-J. Lee, "Characterization of Shapiro steps in the presence of a 4π-periodic Josephson current", Phys. Rev. B **103**, 1–9 (2021).

[119] L. Galletti, S. Charpentier, P. Lucignano, D. Massarotti, R. Arpaia, F. Tafuri, T. Bauch, Y. Suzuki, A. Tagliacozzo, K. Kadowaki, and F. Lombardi, "Josephson effect in Al/Bi_2Se_3/Al coplanar hybrid devices", Phys. C Supercond. its Appl. **503**, 162–165 (2014).

[120] L. Galletti, S. Charpentier, Y. Song, D. Golubev, S. M. Wang, T. Bauch, F. Lombardi, A. We, A. Bi, and T. Al, "High-Transparency Al/Bi_2Te_3 Double-Barrier Heterostructures", **27**, 10–13 (2017).

[121] S. Charpentier, L. Galletti, G. Kunakova, R. Arpaia, Y. Song, R. Baghdadi, S. M. Wang, A. Kalaboukhov, E. Olsson, F. Tafuri, D. Golubev, J. Linder, T. Bauch, and F. Lombardi, "Induced unconventional superconductivity on the surface states of Bi_2Te_3 topological insulator", Nat. Commun. **8**, 6–13 (2017).

[122] B. A. Aminov, A. A. Golubov, and M. Y. Kupriyanov, "Quasiparticle current in ballistic constrictions with finite transparencies of interfaces", Phys. Rev. B **53**, 365–373 (1996).

[123] A. Chrestin, T. Matsuyama, and U. Merkt, "Evidence for a proximity-induced energy gap in Nb/InAs/Nb junctions", Phys. Rev. B **55**, 8457–8465 (1997).

[124] A. J. Watson, W. Lu, M. H. Guimarães, and M. Stöhr, "Transfer of large-scale two-dimensional semiconductors: challenges and developments", 2D Materials **8**, 032001 (2021).

[125] C. Wen, "Coplanar Waveguide: A Surface Strip Transmission Line Suitable for Nonreciprocal Gyromagnetic Device Applications", IEEE Transactions on Microwave Theory and Techniques **17**, 1087–1090 (1969).

[126] K. Watanabe, K. Yoshida, and T. A. Kohjiro, "Kinetic Inductance of Superconducting Coplanar Waveguides", Japanese Journal of Applied Physics **33**, 5708 (1994).

[127] J. Gao, "The physics of superconducting microwave resonators", PhD thesis (California Institute of Technology, 2008).

[128] M. S. Khalil, M. Stoutimore, F. Wellstood, and K. Osborn, "An analysis method for asymmetric resonator transmission applied to superconducting devices", Journal of Applied Physics **111** (2012).

[129] S. Probst, F. B. Song, P. A. Bushev, A. V. Ustinov, and M. Weides, "Efficient and robust analysis of complex scattering data under noise in microwave resonators", Review of Scientific Instruments **86**, 024706 (2015).

[130] M. Göppl, A Fragner, M Baur, R Bianchetti, S. Filipp, J. M. Fink, P. J. Leek, G Puebla, L Steffen, and A. Wallraff, "Coplanar waveguide resonators for circuit quantum electrodynamics", Journal of Applied Physics **104** (2008).

[131] **A. P. Surendran**, G. Kunakova, X. Palermo, K. Niherysh, D. Montemurro, J. Andzane, D. Erts, D. S. Golubev, S. Lara-Avila, F. Lombardi, and T. Bauch, "Ballistic transport on micrometer scale revealed by Fabry-Pérot-like resonances in Bi_2Se_3 nanoribbon devices", Submitted to Phys. Rev. Applied (2023).

[132] A. D. K. Finck, C. Kurter, Y. S. Hor, and D. J. Van Harlingen, "Phase Coherence and Andreev Reflection in Topological Insulator Devices", Phys. Rev. X **4**, 041022 (2014).

[133] A. D. Finck, C. Kurter, E. D. Huemiller, Y. S. Hor, and D. J. Van Harlingen, "Robust Fabry-Perot interference in dual-gated Bi_2Se_3 devices", Applied Physics Letters **108**, 203101 (2016).

[134] Karalic, Matija and Štrkalj, Antonio and Masseroni, Michele and Chen, Wei and Mittag, Christopher and Tschirky, Thomas and Wegscheider, Werner and Ihn, Thomas and Ensslin, Klaus and Zilberberg, Oded, "Electron-Hole Interference in an Inverted-Band Semiconductor Bilayer", Phys. Rev. X **10**, 031007 (2020).

[135] C. W. J. Beenakker, "Colloquium: Andreev reflection and Klein tunneling in graphene", Reviews of Modern Physics **80**, 1337–1354 (2008).

[136] A. V. Shytov, M. S. Rudner, and L. S. Levitov, "Klein Backscattering and Fabry-Pérot Interference in Graphene Heterojunctions", Phys. Rev. Lett. **101**, 156804 (2008).

[137] Markus Müller and Matthias Bräuninger and Björn Trauzettel, "Temperature dependence of the conductivity of ballistic graphene", Physical Review Letters **103**, 2–5 (2009).

[138] D. Gunlycke and C. T. White, Applied Physics Letters **93**, 122106 (2008).

[139] M. Oksanen, A. Uppstu, A. Laitinen, D. J. Cox, M. F. Craciun, S. Russo, A. Harju, and P. Hakonen, "Single-mode and multimode Fabry-Pérot interference in suspended graphene", Phys. Rev. B **89**, 121414 (2014).

[140] S. Cho, B. Dellabetta, R. Zhong, J. Schneeloch, T. Liu, G. Gu, M. J. Gilbert, and N. Mason, "Aharonov-Bohm oscillations in a quasi-ballistic three-dimensional topological insulator nanowire", Nature Communications **6**, 6–10 (2015).

[141] F. Münning, O. Breunig, H. F. Legg, S. Roitsch, D. Fan, M. Rößler, A. Rosch, and Y. Ando, "Quantum confinement of the Dirac surface states in topological-insulator nanowires", Nature Communications **12** (2021).

[142] **A. P. Surendran**, D. Montemurro, G. Kunakova, X. Palermo, K. Niherysh, E. Trabaldo, D. S. Golubev, J. Andzane, D. Erts, F. Lombardi, and T. Bauch, "Current-phase relation of a short multi-mode Bi_2Se_3 topological insulator nanoribbon Josephson junction with ballistic transport modes", Superconductor Science and Technology **36**, 064003 (2023).

[143] A. A. Golubov, M. Y. Kupriyanov, and E. Il'ichev, "The current-phase relation in Josephson junctions", Rev. Mod. Phys. **76**, 411–469 (2004).

[144] M. L. Della Rocca, M. Chauvin, B. Huard, H. Pothier, D. Esteve, and C. Urbina, "Measurement of the current-phase relation of superconducting atomic contacts", Phys. Rev. Lett. **99**, 1–4 (2007).

[145] G. Nanda, J. L. Aguilera-Servin, P. Rakyta, A. Kormányos, R. Kleiner, D. Koelle, K. Watanabe, T. Taniguchi, L. M. Vandersypen, and S. Goswami, "Current-Phase Relation of Ballistic Graphene Josephson Junctions", Nano Lett. **17**, 3396–3401 (2017).

[146] M. D. Thompson, M. Ben Shalom, A. K. Geim, A. J. Matthews, J. White, Z. Melhem, Y. A. Pashkin, R. P. Haley, and J. R. Prance, "Graphene-based tunable SQUIDs", Appl. Phys. Lett. **110** (2017).

[147] F. Nichele, E. Portolés, A. Fornieri, A. M. Whiticar, A. C. Drachmann, S. Gronin, T. Wang, G. C. Gardner, C. Thomas, A. T. Hatke, M. J. Manfra, and C. M. Marcus, "Relating Andreev Bound States and Supercurrents in Hybrid Josephson Junctions", Phys. Rev. Lett. **124**, 1–6 (2020).

[148] C. Li, B. de Ronde, J. de Boer, J. Ridderbos, F. Zwanenburg, Y. Huang, A. Golubov, and A. Brinkman, "Zeeman-Effect-Induced $0-\pi$ Transitions in Ballistic Dirac Semimetal Josephson Junctions", Phys. Rev. Lett. **123**, 026802 (2019).

[149] I. Babich, A. Kudriashov, D. Baranov, and V. S. Stolyarov, "Limitations of the Current-Phase Relation Measurements by an Asymmetric dc-SQUID", Nano Letters **23**, 6713–6719 (2023).

[150] K. K. Likharev, "Superconducting weak links", Rev. Mod. Phys. **51**, 101–159 (1979).

[151] A. Murphy and A. Bezryadin, "Asymmetric nanowire SQUID: Linear current-phase relation, stochastic switching, and symmetries", Phys. Rev. B **96**, 094507 (2017).

[152] W. Mayer, M. C. Dartiailh, J. Yuan, K. S. Wickramasinghe, E. Rossi, and J. Shabani, "Gate controlled anomalous phase shift in Al/InAs Josephson junctions", Nat. Commun. **11** (2020).

[153] J. Johansson, K. Cedergren, T. Bauch, and F. Lombardi, "Properties of inductance and magnetic penetration depth in (103)-oriented $YBa_2Cu_3O_7$-δ thin films", Phys. Rev. B - Condens. Matter Mater. Phys. **79**, 1–6 (2009).

[154] J. Romijn, T. M. Klapwijk, and J. E. Mooij, "Critical pair-breaking current in superconductors far below Tc", Phys. B+C **108**, 981–982 (1981).

[155] H. Courtois, M. Meschke, J. T. Peltonen, and J. P. Pekola, "Origin of hysteresis in a proximity josephson junction", Physical Review Letters **101**, 1–4 (2008), eprint: 0805.4524.

[156] R. Haller, G. Fülöp, D. Indolese, J. Ridderbos, R. Kraft, L. Y. Cheung, J. H. Ungerer, K. Watanabe, T. Taniguchi, D. Beckmann, R. Danneau, P. Virtanen, and C. Schönenberger, "Phase-dependent microwave response of a graphene Josephson junction", Phys. Rev. Res. **4**, 10.1103/PhysRevResearch.4.013198 (2022).

[157] T. Akazaki, H. Nakano, J. Nitta, and H. Takayanagi, "Observation of enhanced thermal noise due to multiple Andreev reflection in ballistic InGaAs-based superconducting weak links", Applied Physics Letters **86**, 1–3 (2005).

[158] R. Wakatsuki, Y. Saito, S. Hoshino, Y. M. Itahashi, T. Ideue, M. Ezawa, Y. Iwasa, and N. Nagaosa, "Nonreciprocal charge transport in noncentrosymmetric superconductors", Science Advances **3**, e1602390 (2017).

[159] R. S. Souto, M. Leijnse, and C. Schrade, "Josephson Diode Effect in Supercurrent Interferometers", Phys. Rev. Lett. **129**, 267702 (2022).

[160] F. Ando, Y. Miyasaka, T. Li, J. Ishizuka, T. Arakawa, Y. Shiota, T. Moriyama, Y. Yanase, and T. Ono, "Observation of superconducting diode effect", Nature **584**, 373–376 (2020).

[161] B. Turini, S. Salimian, M. Carrega, A. Iorio, E. Strambini, F. Giazotto, V. Zannier, L. Sorba, and S. Heun, "Josephson Diode Effect in High-Mobility InSb Nanoflags", Nano Letters **22**, 8502–8508 (2022).

[162] B. Pal, A. Chakraborty, P. K. Sivakumar, M. Davydova, A. K. Gopi, A. K. Pandeya, J. A. Krieger, Y. Zhang, M. Date, S. Ju, et al., "Josephson diode effect from Cooper pair momentum in a topological semimetal", Nature physics **18**, 1228–1233 (2022).

[163] C. Baumgartner, L. Fuchs, A. Costa, S. Reinhardt, S. Gronin, G. C. Gardner, T. Lindemann, M. J. Manfra, P. E. Faria Junior, D. Kochan, et al., "Supercurrent rectification and magnetochiral effects in symmetric Josephson junctions", Nature nanotechnology **17**, 39–44 (2022).

[164] H. Narita, J. Ishizuka, R. Kawarazaki, D. Kan, Y. Shiota, T. Moriyama, Y. Shimakawa, A. V. Ognev, A. S. Samardak, Y. Yanase, et al., "Field-free superconducting diode effect in noncentrosymmetric superconductor/ferromagnet multilayers", Nature Nanotechnology **17**, 823–828 (2022).

[165] H. Wu, Y. Wang, Y. Xu, P. K. Sivakumar, C. Pasco, U. Filippozzi, S. S. Parkin, Y.-J. Zeng, T. McQueen, and M. N. Ali, "The field-free Josephson diode in a van der Waals heterostructure", Nature **604**, 653–656 (2022).

[166] J.-X. Lin, P. Siriviboon, H. D. Scammell, S. Liu, D. Rhodes, K Watanabe, T Taniguchi, J. Hone, M. S. Scheurer, and J. Li, "Zero-field superconducting diode effect in small-twist-angle trilayer graphene", Nature Physics **18**, 1221–1227 (2022).

[167] Y. V. Fominov and D. S. Mikhailov, "Asymmetric higher-harmonic SQUID as a Josephson diode", Phys. Rev. B **106**, 134514 (2022).

[168] A. Greco, Q. Pichard, and F. Giazotto, "Josephson diode effect in monolithic dc-SQUIDs based on 3D Dayem nanobridges", Applied Physics Letters **123**, 092601 (2023).

[169] C. Ciaccia, R. Haller, A. C. C. Drachmann, T. Lindemann, M. J. Manfra, C. Schrade, and C. Schönenberger, "Gate-tunable Josephson diode in proximitized InAs supercurrent interferometers", Phys. Rev. Res. **5**, 033131 (2023).

[170] M. Trahms, L. Melischek, J. F. Steiner, B. Mahendru, I. Tamir, N. Bogdanoff, O. Peters, G. Reecht, C. B. Winkelmann, F. von Oppen, et al., "Diode effect in Josephson junctions with a single magnetic atom", Nature **615**, 628–633 (2023).

[171] B. Dassonneville, A. Murani, M. Ferrier, S. Guéron, and H. Bouchiat, "Coherence-enhanced phase-dependent dissipation in long SNS Josephson junctions: Revealing Andreev bound state dynamics", Physical Review B **97**, 184505 (2018).

[172] B. Dassonneville, M. Ferrier, S. Guéron, and H. Bouchiat, "Dissipation and supercurrent fluctuations in a diffusive normal-metal–superconductor ring", Physical Review Letters **110**, 217001 (2013).

[173] M. Ferrier, B. Dassonneville, S. Guéron, and H. Bouchiat, "Phase-dependent Andreev spectrum in a diffusive SNS junction: Static and dynamic current response", Physical Review B **88**, 174505 (2013).

[174] V. Chidambaram, A. Kringhøj, L. Casparis, F. Kuemmeth, T. Wang, C. Thomas, S. Gronin, G. C. Gardner, Z. Cui, C. Liu, et al., "Microwave sensing of Andreev bound states in a gate-defined superconducting quantum point contact", Physical Review Research **4**, 023170 (2022).

[175] M. Arzeo, F. Lombardi, and T. Bauch, "Microwave losses in MgO, $LaAlO_3$, and $(La_{0.3}Sr_{0.7})(Al_{0.65}Ta_{0.35})$ O_3 dielectrics at low power and in the millikelvin temperature range", Applied Physics Letters **104** (2014).

[176] A Zazunov, V. Shumeiko, G Wendin, and E. Bratus, "Dynamics and phonon-induced decoherence of Andreev level qubit", Physical Review B **71**, 214505 (2005).

[177] M. J. Molaei, M. Younas, and M. Rezakazemi, "A Comprehensive Review on Recent Advances in Two-Dimensional (2D) Hexagonal Boron Nitride", ACS Applied Electronic Materials **3**, 5165–5187 (2021).

[178] R. Sondors, K. Niherysh, J. Andzane, X. Palermo, T. Bauch, F. Lombardi, and D. Erts, "Low-Vacuum Catalyst-Free Physical Vapor Deposition and Magnetotransport Properties of Ultrathin Bi_2Se_3 Nanoribbons", Nanomaterials **13** (2023).

[179] K. Niherysh, X. Palermo, **A. P. Surendran**, A. Kalaboukhkov, R. Sondors, J. Andzane, D. Erts, T. Bauch, and F. Lombardi, "Quantum Confinement and Coherent Transport in Ultrathin Bi_2Se_3 nanoribbons", Submitted to Phys. Rev. Applied (2023).

[180] A. Murani, S. Sengupta, A. Kasumov, R. Deblock, C. Celle, J.-P. Simonato, H. Bouchiat, and S. Guéron, "Long- to short-junction crossover and field-reentrant critical current in Al/Ag-nanowires/Al Josephson junctions", Phys. Rev. B **102**, 214506 (2020).

[181] A Zazunov, V. Shumeiko, E. Bratus, J Lantz, and G Wendin, "Andreev level qubit", Physical review letters **90**, 087003 (2003).

[182] A. Omelyanchouk, S. Shevchenko, Y. S. Greenberg, O Astafiev, and E Ilâ€™ichev, "Quantum behavior of a flux qubit coupled to a resonator", Low Temperature Physics **36**, 893–901 (2010).